

Hydrogen Storage by Physisorption on Porous Materials

Von der Fakultät Chemie der Universität Stuttgart zur
Erlangung der Würde eines Doktors der Naturwissenschaften
(Dr. rer. nat.) genehmigte Abhandlung

vorgelegt von
Barbara Panella
aus Rom, Italien

Hauptbericht: Prof. Dr. E. Roduner

Mitbericht: Prof. Dr. G. Schütz

Tag der mündlichen Prüfung: 13.09.2006

Max-Planck-Institut für Metallforschung,

Stuttgart

2006

Dedicato al mio adorato Papà

INDEX	1
1 INTRODUCTION AND MOTIVATION	3
2 FUNDAMENTALS	5
2.1 Physisorption	5
2.1.1 Principles of physisorption and adsorption isotherms	5
2.1.2 Hydrogen storage capacity	10
2.1.3 Theoretical approaches	13
2.1.4 Principles of Raman spectroscopy	13
2.2 Microporous materials / High SSA materials	18
2.2.1 Carbon materials	18
2.2.2 Metal-organic frameworks	21
2.2.3 Zeolites	24
3 EXPERIMENTAL TECHNIQUES	26
3.1 Sieverts' apparatus	26
3.2 Thermal desorption spectroscopy (TDS)	31
3.3 Raman spectroscopy	36
4 CARBON MATERIALS	38
4.1 Sample preparation and characterisation	38
4.2 Volumetric measurements	40
4.2.1 Results	40
4.2.2 Discussion	43
4.3 Thermal desorption spectroscopy	48
4.3.1 Results	48
4.3.2 Discussion	50
4.4 Raman spectroscopy	54

4.4.1 Results	54
4.4.2 Discussion	61
4.5 Summary	69
5 METAL-ORGANIC-FRAMEWORKS	71
5.1 Sample preparation and characterisation	71
5.2 Volumetric measurements	79
5.2.1 Results	79
5.2.2 Discussion	82
5.3 Thermal desorption spectroscopy	87
5.3.1 Results	87
5.3.2 Discussion	89
5.4 Raman spectroscopy	
5.4.1 Results	96
5.4.2 Discussion	99
5.5 Summary	101
6 COMPARISON BETWEEN NANOSTRUCTURED MATERIALS WITH HIGH SSA	103
7 CONCLUSIONS	109
8 ZUSAMMENFASSUNG	113
Appendix A	123
Appendix B	127
References	132
Acknowledgments	140
Curriculum Vitae	142

1 Introduction and motivation

Hydrogen gas is the ideal energy carrier, due to its pollutant-free combustion, which produces exclusively energy and water. The reaction of hydrogen with oxygen can be exploited for vehicle propulsion either in direct combustion engines or using fuel cells, which convert the chemical energy into electrical energy. A great challenge for commercializing hydrogen powered vehicles is on-board hydrogen storage using light weight, cheap and secure systems. Two different storage technologies are conventionally used, i.e. hydrogen gas in high pressure tanks made of steel or composite material, and liquid hydrogen in cryogenic vessels.^[1] Both technologies possess severe disadvantages for mobile applications. Indeed, hydrogen gas occupies large volumes at room temperature, and high pressures of several hundred bar are necessary to reach high storage capacities. Liquid hydrogen is successfully used for space shuttles propulsion, however the low condensation temperature of about 20 K, the related hydrogen boil-off and the sophisticated isolation technique, which is necessary at these temperatures, are big disadvantages for vehicles. In addition the energy required for liquefaction corresponds to more than 30% of the energy content of hydrogen.^[2]

An alternative solution is therefore hydrogen storage in solid materials. Here three principle storage mechanisms can be distinguished: i) chemisorption and absorption of hydrogen atoms in metals ii) formation of compounds with ionic character, like complex hydrides and iii) physisorption (or physical adsorption) of hydrogen molecules on porous materials.

Physical adsorption exhibits several advantages over chemical hydrogen storage as for example the complete reversibility and the fast kinetics. In addition a very small amount of energy ($< 10 \text{ kJ mol}^{-1}$) is involved both in the adsorption and in the release of H_2 . In contrast to hydrogen stored in metal hydrides and complex hydrides, no extra heat management systems are therefore required for on-board applications. Owing to the weak interaction forces, typically temperatures of about 80 K are necessary to reach high storage capacities in physisorption. Even though room temperature hydrogen storage technologies are more desirable in vehicles, cryogenic

tanks working at 80 K are far easier to manage than vessels with liquid hydrogen at 20 K. The investigation of hydrogen adsorption on porous materials for mobile application has become a big challenge, due to these interesting properties.

The texture and the structure of porous adsorbents may play a crucial role for the physisorption phenomenon of H₂ molecules. Thus the present work is focused on the systematic investigation of the hydrogen adsorption mechanism in different classes of porous materials, mainly carbon-based materials and metal-organic frameworks. In particular, the main goal of this thesis is to gain understanding on the physics of the adsorption and to correlate the hydrogen-adsorption properties, i.e. storage capacity and interaction strength, to the structure and texture of the adsorbent. This understanding could provide the way to further optimize porous materials for hydrogen adsorption.

Different experimental techniques extended to previously unexplored pressure and temperature ranges have been developed and employed in the present work. Adsorption isotherms have been measured volumetrically up to high pressures and at different temperatures, Raman spectroscopy has been used on different porous materials, and a setup for thermal desorption spectroscopy has been especially designed to work at temperatures down to 20 K. The techniques used have been especially adapted and the experimental setups modified to investigate physisorption of hydrogen, which requires special care owing to the low temperatures at which the process takes place.

The results obtained using these different experimental approaches on metal-organic frameworks and carbon materials will contribute to the investigation of a completely novel field. Indeed, when this thesis work was started, metal-organic frameworks were almost completely unexplored from the point of view of their hydrogen storage potential^[3,4] and no comparison with other porous materials existed.

Finally, similarities and differences between porous materials possessing different structures and composition, including literature data are discussed.

2 Fundamentals

2.1 Physisorption

2.1.1 Principles of physisorption and adsorption isotherms

Physical adsorption of a gas on a solid can be described as an enrichment of molecules at the interface between the solid surface and the gas phase. Responsible for this phenomenon is a combination of attractive dispersive (or van der Waals) interactions and short range repulsive interactions between the adsorbent and the adsorbate molecule. This results in a minimum in the potential energy curve of the gas at approximately one molecular radius from the solid surface. The attractive interaction originates from long-range forces produced by fluctuations in the charge distribution of the gas molecules and of the atoms on the surface, giving rise to attraction between temporary fluctuating and induced dipoles. However, at small distances the overlap between the electron cloud of the gas molecule and of the substrate is significant and the repulsion increases rapidly.

The potential curve for the gas molecule approaching the surface is well known under the name of Lennard-Jones potential.^[5] The order of magnitude of this type of interaction depends both on the nature of the gas molecule and of the adsorbing material, but typically the values for molecular hydrogen adsorption lie in the range between 1 and 10 kJ mol⁻¹, which is approximately ten times less than for chemisorption.^[2] Fig. 2.1 shows the potential energy curve for a hydrogen molecule as a function of the distance from the adsorbent, both for dissociative adsorption, i.e. chemisorption and for molecular adsorption, i.e. physisorption.

In physical adsorption there is no energy barrier to prevent the molecule approaching the surface from entering the physisorption well. Therefore, if no diffusional barriers are present, the process is non-activated and fast kinetics is characteristic for physical adsorption.

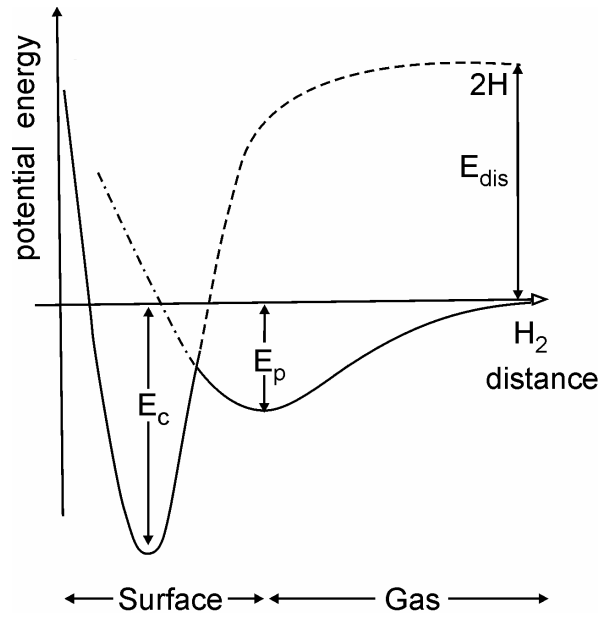


Fig. 2.1: Potential energy curve for chemisorbed and physisorbed hydrogen as a function of the distance from the adsorbent's surface. The minima of the two curves correspond to the equilibrium distance for physisorbed (E_p) and chemisorbed (E_c) hydrogen.

Six different classes of isotherms were determined for physical adsorption according to the IUPAC (International Union of Pure and Applied Chemistry) classification of 1985.^[6] These correlate the amount of gas adsorbed with the applied gas pressure. Microporous materials typically exhibit a type I adsorption isotherm. This type of isotherm shows an initial steep increase, corresponding to progressive filling of the micropores, then a plateau is reached at higher pressures, corresponding to monolayer coverage (fig. 2.2 left).

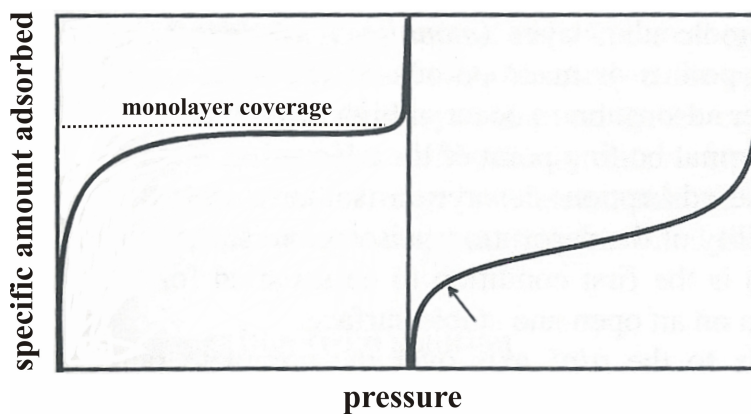


Fig. 2.2: Type I adsorption isotherm (left) and type II adsorption isotherm (right).

Indeed, for microporous materials the small pore dimensions of the adsorbent limit the adsorption only to one or a few molecular layers.^[7] The Langmuir model describes type I isotherms with a kinetic approach and assuming that the adsorption enthalpy is independent from the coverage.^[8]

This model yields the Langmuir equation, which relates the coverage, θ , with the applied gas pressure P :

$$\theta = \frac{a \cdot P / P^0}{1 + a \cdot P / P^0} \quad (2.1)$$

where, above the critical temperature of the adsorbate P^0 is the standard pressure. Below the critical temperature P^0 would be substituted with the saturation pressure in this equation. The coverage, θ , can be expressed as the ratio between the amount of gas adsorbed at the pressure P and the maximum amount corresponding to monolayer coverage. The adsorption coefficient, a , depends on the heat of adsorption, E_a , and on the temperature, T :

$$a = K \cdot \exp\left(\frac{E_a}{RT}\right) \quad (2.2)$$

The initial steep rise in the isotherm depends therefore on the heat of adsorption, i.e. the stronger the interaction between gas and adsorbent the sharper is the initial increase of the amount of gas adsorbed as a function of pressure. The plateau value of the hydrogen storage capacity is independent of the interaction energy and corresponds to the complete monolayer coverage of the adsorbent's surface. The fractional coverage in the Langmuir equation can also be expressed as a function of the chemical potential of the gas, μ , and of the adsorption potential, ε , in the form presented in eq. 2.3.^[9,10]

$$\theta = \frac{1}{1 + \exp\left(\frac{\varepsilon - \mu}{RT}\right)} \quad (2.3)$$

This equation is equivalent to equation (2.4):

$$\varepsilon = RT \ln\left(\frac{1}{\theta} - 1\right) + \mu \quad (2.4)$$

For an ideal gas the expression of the chemical potential depends on the standard chemical potential, μ^0 , at the measured temperature and on the pressure as shown in eq. (2.5)

$$\mu = \mu^0 + RT \ln(P/P^0) \quad (2.5)$$

P^0 corresponds here to the standard pressure. The validity of this equation, and of introducing the pressure instead of the fugacity in (2.5), can be determined by plotting the chemical potential as a function of $\ln(P/P^0)$. The chemical potential can be calculated from the tabulated values of the enthalpy and the entropy of the gas. Considering equation (2.1), (2.4) and (2.5) it is possible to obtain a new expression for the adsorption potential:

$$\varepsilon = \mu^0 - RT \ln a \quad (2.6)$$

This equation shows that applying the Langmuir model the resulting adsorption energy is independent of the coverage. Indeed, it is a characteristic of this model to assume that no lateral interaction between adsorbed molecules exists, and that the adsorption enthalpy is therefore independent of the number of molecules adsorbed on the surface.

For gas adsorption at low coverage the adsorbed molecules behave like a two dimensional ideal gas, which is well described by Henry's law:^[5]

$$\theta = k' \cdot (P/P^0) \quad (2.8)$$

where k' depends on the potential energy of adsorption ϕ according to equation (2.9)

$$k' = \frac{v_p}{RT} \cdot \left[\exp\left(-\frac{\phi}{kT}\right) - 1 \right] \quad (2.9)$$

v_p is the pore volume, T the temperature and k the Boltzmann constant.

Another common isotherm observed in physisorption is the type II isotherm, which typically indicates the formation of multimolecular layers at higher pressures. The type II isotherm is shown in figure 2 (right), where the inflection point signed by the arrow corresponds to completion of the first monolayer. The Brunauer- Emmett-Teller (BET) theory is an extension of the Langmuir model for multilayer adsorption which describes relatively well the type II isotherm.^[11] This theory is based on the assumption that the energy of adsorption in the second and in the higher layers is equal to the liquefaction energy of the adsorbent. The BET equation is often expressed in the linear form:

$$\frac{P}{n(P^0 - P)} = \frac{1}{n_m C} + \frac{C - 1}{n_m C} \cdot \frac{P}{P^0}, \quad (2.10)$$

where n is the number of adsorbed molecules, n_m the monolayer capacity, P^0 is the saturation pressure and the constant C depends on the difference between adsorption energy of the first layer and the liquefaction energy of the adsorbate. It is nowadays confirmed that the BET model is for several reasons unable to describe in a realistic way a physisorption system, even though it reproduces the shape of the isotherm.^[12] Nevertheless, the BET model is commonly applied to determine the apparent specific surface area (SSA) for porous materials from nitrogen adsorption isotherms at 77 K and can be applied to compare different porous materials. Moreover the value of the specific surface often depends on the probe molecule used for the adsorption and on its accessibility in the pores of the adsorbent. Typically, adsorption isotherms of N_2 , Ar and CO_2 are used to determine the specific surface area of porous materials.

2.1.2 Hydrogen storage capacity

The amount of gas adsorbed, n_{ads} , on a solid is defined as the gas quantity introduced in the sample cell, n_i , minus the moles of free molecules in the gas phase:

$$n_{\text{ads}} = n_i - V_g \rho_g \quad (2.11)$$

where V_g is the volume occupied by the gas, including the pore volume of the sample and ρ_g is its density. As the real volume occupied by the gas phase is not known, experimental adsorption isotherms typically report the excess uptake, n_{ex} , i.e (2.12):

$$n_{\text{ex}} = n_i - V_0 \rho_g \quad (2.12)$$

where V_0 is the void volume including the pore volume of the sample measured with He gas expansion.^[13]

The relation between excess uptake and absolute uptake is therefore expressed in equation (2.13):

$$n_{\text{ex}} = n_{\text{ads}} + \rho_g (V_g - V_0) \quad (2.13)$$

The difference $(V_g - V_0)$, corresponds to the volume occupied by the adsorbed phase, with density ρ_a , in the pores of the adsorbent. This leads to the following expression of the excess uptake:^[14]

$$n_{\text{ex}} = \left(1 - \frac{\rho_g}{\rho_a}\right) n_{\text{ads}} \quad (2.14)$$

The schematic representation in figure 2.3. shows the difference between the void volume determined by He gas expansion and the real void volume V_g , which is determined by the volume of the adsorbed gas.

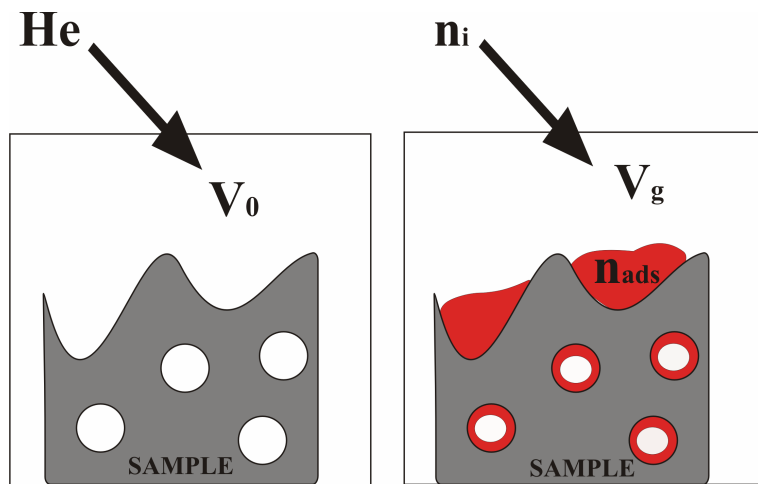


Fig. 2.3: Schematic diagram of the void volume V_0 in the sample cell, including the pore volume of the sample measured with He gas expansion (left) and of the real void volume of the sample cell and of the porous sample, V_i , considering the adsorbed phase (right).

While the absolute adsorption capacity, n_{ads} , for a type I isotherm reaches the saturation value at high pressures and then remains constant, the excess adsorption isotherm exhibits a maximum and then decreases at high gas densities, as shown in fig 2.4.

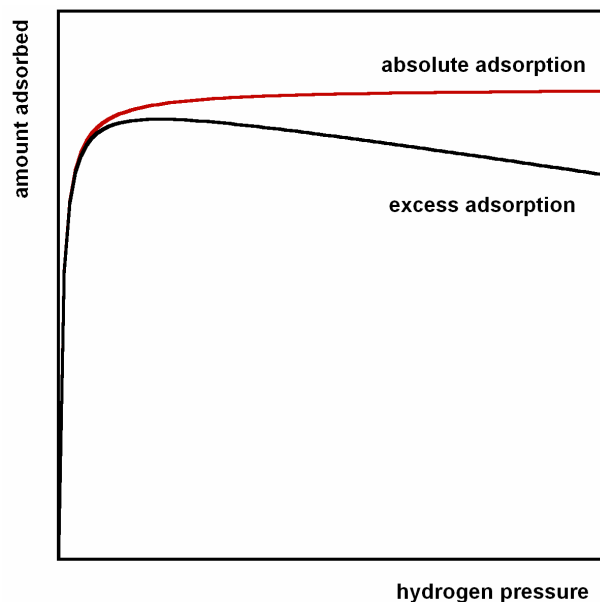


Fig. 2.4: Absolute adsorption isotherm (red), excess adsorption isotherm (black) for a microporous material.

The excess adsorption is zero when the gas density and the adsorbed density are equal. Typically at supercritical temperatures the inflection of the excess adsorption isotherm is observed only at very high pressures. Therefore, usually both the absolute adsorption isotherm and the excess adsorption isotherm of hydrogen in microporous materials are well described by the Langmuir model up to a certain pressure.

The amount of gas adsorbed on a solid can be expressed in several forms. The commonly applied definitions in hydrogen storage are the weight percent (*wt%*) storage capacity and the volumetric storage capacity (*vol*). The *wt%* storage capacity is defined as the mass of hydrogen adsorbed over the total mass, including adsorbent and adsorbate, i.e.:

$$wt\% = \frac{m_{H_2}}{m_{H_2} + m_s} * 100 , \quad (2.15)$$

where m_{H_2} is the mass of adsorbed hydrogen and m_s is the mass of the solid adsorbent. The volumetric uptake is defined as the amount of hydrogen adsorbed divided by the volume of the solid sample, i.e.

$$vol = \frac{m_{H_2}}{V_s} = \frac{m_{H_2}}{m_s} \cdot \rho_s \quad (2.16)$$

For mobile applications the packing density, ρ_s , of the material should be considered to calculate the volumetric uptake. The packing density is determined by the mass of the sample and the volume it occupies when it is subjected to mechanical compaction. However, often the bulk density of the material is considered, which can be determined more easily. This is typically measured by mercury pycnometry, i.e. displacement of a volume of mercury corresponding to the bulk volume of the sample. For crystalline materials the bulk density can also be theoretically calculated by X-Ray diffraction analysis and structure determination.

2.1.3 Theoretical approaches

Several theoretical models can be used to describe physical adsorption of a fluid on a porous material. These are mainly molecular simulation methods and density functional theory (DFT). The simulation methods, which are more commonly used, base on Grand Canonical Monte Carlo or Gibbs Ensemble Monte Carlo calculations. To take into account for quantum effects at low temperatures Monte Carlo simulations are integrated with the path integral formalism.^[15,16]

In Monte Carlo simulations a sequence of molecular configurations is generated in such a way that they occur with the corresponding equilibrium probability. This depends on the temperature and on the intermolecular energy of the system. Finally the thermodynamic quantities like adsorption energies and uptake values are estimated by averaging their values over the sequence. Typically for the pair-wise interaction between adsorbate and adsorbent the Lennard-Jones 12-6 potential is used.

Density functional theory is usually applied to simple systems composed of porous materials with well defined pore shapes, like slit pores, spheres or cylinders and simple gases.^[5] In this case DFT is less time consuming than simulations, but becomes unreliable for more complex systems. In DFT the energy of this system is expressed as a function of the density profile. Through variational methods the energy is minimized and the density profile is determined. This procedure requires an initial approximate form of the energy before proceeding with the subsequent minimization.

2.1.4 Principles of Raman spectroscopy

Rotational and roto-vibrational transitions of homonuclear diatomic molecules like H₂, which do not possess a permanent dipole moment, can be investigated by inelastic light scattering. A monochromatic laser radiation is focused on the sample and the scattered light is measured. The greatest part of this light has the same frequency as the incident radiation, due to elastic or Rayleigh scattering. A small part of the scattered light possesses a lower or higher frequency than the incident one. The

phenomenon of inelastic light scattering is called Raman effect and was discovered in 1928.^[17] This effect arises from the interaction of an electromagnetic radiation with the electron cloud of the molecule. Owing to this interaction an induced dipole moment develops in the molecule, which is in each direction of space proportional to the polarizability of the molecule and to the electric field of the radiation. The oscillation of the polarizability of the molecule due to vibration and rotation is responsible for the inelastic scattering of light.

For a quantum approach of the Raman effect the introduction of virtual energy levels is necessary. The molecule is lifted, due to the interaction with the radiation possessing energy $h\nu_0$, to a virtual state of higher energy and then decays into a different rotational or vibrational state compared to the initial one. In this process the scattered radiation can be up- or down shifted in frequency compared to the incident radiation according to equation (2.17), while for elastic scattering the incident and the scattered radiation possess the same frequency.

$$h\nu_0 = h\nu_{\text{scatt}} + \Delta E_{\text{mol}} \quad (2.17),$$

h is the Planck constant, ν_0 is the frequency of the incident radiation, ν_{scatt} is the frequency of the scattered radiation and ΔE_{mol} is the change in energy of the molecule due to rotational or vibrational transitions. In particular for $\nu_{\text{scatt}} < \nu_0$ the so called Stokes' lines and for $\nu_{\text{scatt}} > \nu_0$ the anti-Stokes' lines are observed. For frequencies and energies measured in wave number units, the Raman shifts give directly the energy differences of the system in cm^{-1} .^[18] Figure 2.5 shows a quantum mechanical representation of the Raman effect and of elastic scattering of light.

For simple rotational transitions the interaction with the laser radiation can induce a change of the rotational energy of the molecule. The expression of the energy of rotational levels for linear molecules, which are free to rotate in the three dimensions of space, in the approximation of the rigid rotor is given by equation (2.18)

$$E_J = BJ(J+1), \quad (2.18)$$

Here J is the rotational quantum number and B the rotational constant, which is inversely proportional to the square of the internuclear distance of the molecule.

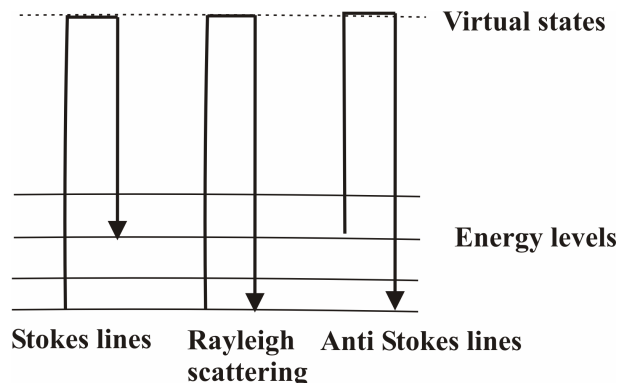


Fig. 2.5: Quantum mechanical representation of the Raman effect.

For pure rotational transitions of linear molecules the selection rules are $\Delta J = 0, \pm 2$, where $\Delta J = 0$ corresponds to pure elastic (Rayleigh) scattering.

Considering the transition from a level J to a level $J' = J \pm 2$, the frequency of the Stokes' lines and anti-Stokes' lines is given by eq. (2.19) and (2.20), respectively:

$$\nu_{\text{Stokes}} = \nu_0 - 2B(2J + 3) \quad (2.19)$$

for $\Delta J = 2$

$$\nu_{\text{anti-Stokes}} = \nu_0 + 2B(2J - 1) \quad (2.20)$$

for $\Delta J = -2$

Both branches, composed by the Stokes' lines and by the anti-Stokes' lines, respectively, are called S-branch in the pure rotational spectrum. Here the single lines will be named as $S_{\Delta\nu}(J)$, with $\Delta\nu$ corresponding to the change in the vibrational quantum number, ν , and J indicating the initial rotational state. For example the line corresponding to the transition with $\Delta\nu = 0$ and from the rotational state with $J = 0$ to $J = 2$ will be labelled with the symbol $S_0(0)$.

For vibrational transitions the selection rules are: $\Delta v = \pm 1$. Adding the rotational selection rules three branches are obtained: O-branch with $\Delta J = -2$, Q-branch with $\Delta J = 0$, and S-branch with $\Delta J = 2$. The positions of the of the O, Q and S branches for $\Delta v = +1$ are approximately given by the following expressions:

$$\nu_O = \nu_0 - \Delta E_{0-1} + 2B(2J - 1) \quad (2.21)$$

$$\nu_Q = \nu_0 - \Delta E_{0-1} \quad (2.22)$$

$$\nu_S = \nu_0 - \Delta E_{0-1} - 2B(2J + 3) \quad (2.23)$$

where ΔE_{0-1} indicates the change of energy of the molecule due to the vibrational transition with $\Delta v = +1$. According to equation (2.22) the Q-branch should be a single line. In reality, due to different values of the rotational constant B for different vibrational levels, the Q-branch can be a rather broad band. If the resolution of the spectrometer is high compared to the separation of the single Q-(J) lines, this band can be resolved in the single components. These correspond to different initial rotational states described by the quantum number $J = 0, 1, 2, 3 \dots$. Figure 2.6 shows the Raman spectrum of a diatomic molecule with the Stokes' and anti-Stokes' lines for pure rotational transitions and with the O-, Q- and S-band for vibration and rotation. Usually Raman spectra are expressed in terms of Raman wavenumber shifts, i.e the wavenumber of the exciting line minus the wavenumber of the scattered radiation ($\Delta v = \nu_0 - \nu_{\text{scatt}}$). Therefore Δv is always positive for Stokes' lines and negative for anti-Stokes' lines.

The intensity of the lines is influenced by nuclear spin population. In particular for hydrogen molecules the intensity of the lines will be influenced by the relative concentration of the two species of hydrogen, i.e para hydrogen (total nuclear spin quantum number $S = 0$) and ortho hydrogen (total nuclear spin quantum number $S = 1$). Indeed, for para-hydrogen only the states with even J quantum numbers will be populated, whereas for ortho-hydrogen only the states with odd J are permitted.^[19]

At low temperatures and under equilibrium conditions all hydrogen molecules populate the lowest rotational level, with $J = 0$. However, at higher temperatures

nuclear spin statistics prevails and the level with $J = 0$ and $J = 1$ possess a statistical weight of 1 and 3, respectively. The equilibrium concentration of para-hydrogen versus temperature is shown in fig. 2.7. As a result of the different ortho and para concentration the Raman spectrum of hydrogen exhibits an alternation in the intensities of the rotational lines. The ortho-para conversion is theoretically forbidden by nuclear spin selection rules. In practice the conversion takes place, but very slowly. This conversion can be accelerated by the presence of a paramagnetic catalyst.

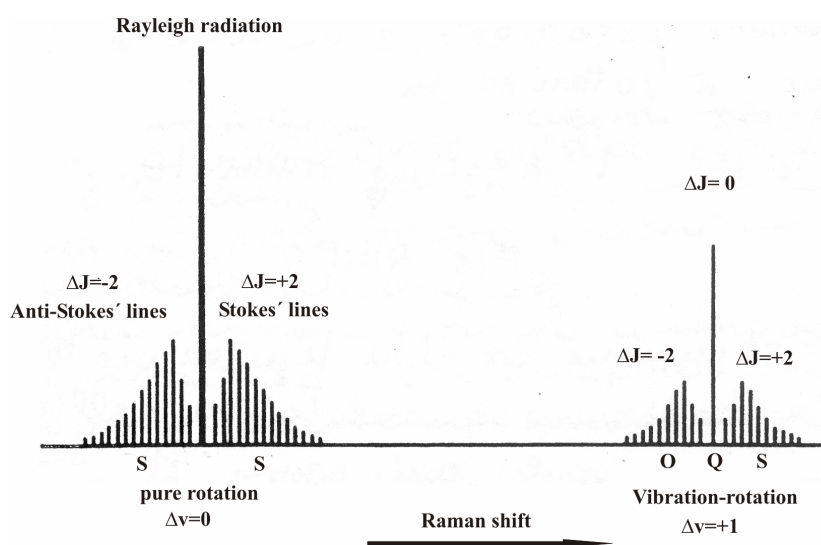


Fig. 2.6: Raman spectrum of a diatomic molecule.

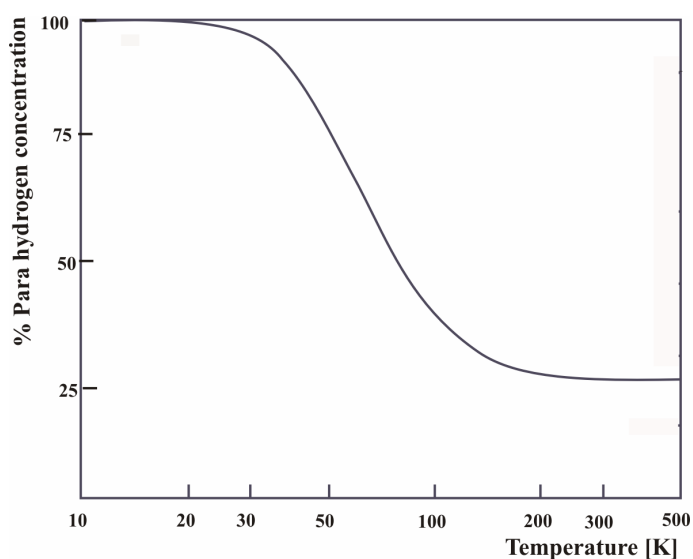


Fig. 2.7: Equilibrium concentration of para-hydrogen versus temperature. Curve reproduced from reference ^[19].

2.2 Microporous Materials/ High SSA materials

The surface texture and the structure of the adsorbent play a crucial role in the physisorption of gases, and an optimization of these properties can lead to an enhancement of their adsorption potential. The best candidates for storing hydrogen in the molecular form are highly porous nanostructured materials. Among these it is possible to distinguish three main classes: carbon materials, metal-organic frameworks (MOFs), and zeolites.

2.2.1 Carbon materials

A great variety of carbon nanostructures are known in literature as, for example, activated carbon, carbon nanofibres, multi-walled and single-walled nanotubes, carbon nanohorns, etc. Although they all consist of benzene-like carbon hexagons with sp^2 -hybridized carbon atoms, they mainly differ from each other in the way these hexagons are arranged in the material. In principle these materials can be separated into two big groups: those which possess a long-range order of the carbon hexagons, like nanotubes or nanofibres and those which have irregular structures like activated carbon. The majority of carbon nanostructures are mixtures of well ordered material, often of short range, surrounded by disordered material. The proportions of the ordered and disordered regions contribute greatly to the properties of the material.^[20] For instance tubular shaped single-walled carbon nanotubes (SWCNTs) are the best example of a well ordered structure with defined curvature (fig. 2.8). They can be considered as rolled graphene sheets with an inner diameter ranging from less than one to several nanometers and a length of 10 to 100 μm . Usually nanotubes are closed at both ends with caps, which have a fullerene like structure. Depending on which direction the graphite sheet is rolled in respect to the lattice vectors, three types of SWCNT can exist: zig-zag, armchair and chiral, which can be metallic or semiconducting.

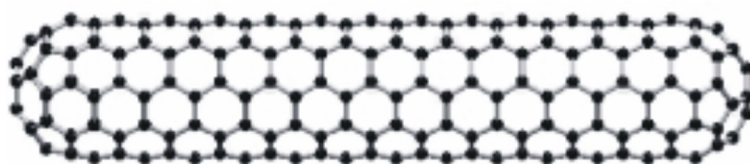


Fig. 2.8: Picture of a SWCNT closed with caps.

Owing to van der Waals forces these tubes tend to form bundles which possess a two-dimensional hexagonal closed packed ordered lattice (Fig. 2.9). Considering this type of lattice well defined positions where gas molecules could be adsorbed exist: the surface of the nanotubes, the grooves between two neighbouring tubes, the interstitial channels between three adjacent nanotubes and for open tubes also the positions inside, the pores, are accessible.^[21] Figure 2.9 shows the position of these adsorption sites in the cross section of the tubes' bundle.

Different main synthetic methods have been developed to produce SWCNTs. Single walled carbon nanotubes synthesized by electric arc discharge between graphite rods have usually a mean diameter of 1.4 nm and contain Fe, Co and Ni as metal catalyst particles. Similar characteristics are possessed by nanotubes produced by laser ablation of graphite. The highest production rate is offered by the HiPco (high pressure CO disproportion)^[22] method which yields by catalytic disproportion of carbon monoxide SWCNTs with a diameter of 1 nm.^[23] Also chemical vapour deposition is a cheap, high yielding synthetic method. Here a hydrocarbon is blown into a tube furnace and the nanotubes grow on a quartz or silicon substrate. The catalyst is either deposited on the substrate or injected in the furnace.^[24]

Depending on the treatment, carbon nanotubes can have very different texture. Non purified SWCNTs contain metal-catalyst particles, which decrease, due to their weight, the specific surface area. Purified SWCNTs possess typically surface areas of 300 - 1000 m² g⁻¹. The interval of SSAs which can be obtained for different samples of single-walled carbon nanotubes is very broad due to the fact that they often contain different forms of carbon, like soot or polyhedral particles.

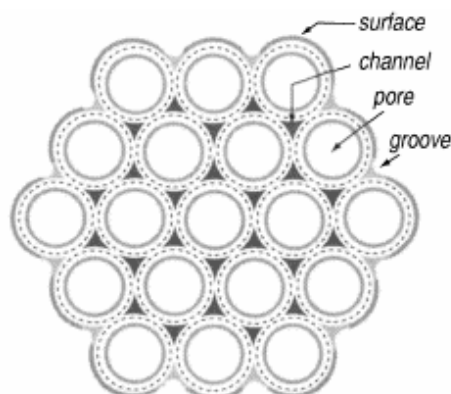


Fig. 2.9: Schematic representation of the cross section of a bundle of SWCNTs showing the sites accessible for gas adsorption. Reproduced from reference ^[21].

In contrast to SWCNTs, activated carbon possesses a highly disordered array of the graphitic platelets. In fact, an essential feature of all models describing activated carbon is a twisted network of carbon layer planes, cross-linked by an extended network of aliphatic carbon. This gives a continuum of interlayer spaces ranging from distances similar to the spacing in graphite up to sizes which can form micropores.^[24]

Carbonaceous structures have very different surface textures and porosities, which can be highly modulated through the synthetic procedure. Regular grade activated carbons have specific surface areas (SSA) of 700 - 1800 m² g⁻¹ but high porosity activated carbons like AX-21^[25] have SSA up to 3000 m² g⁻¹.^[25,26] The porosity in activated carbons is obtained by activation during or prior the carbonization of the organic precursor either through reaction with an oxidizing gas or with inorganic chemicals. “Super active carbons” like AX-21 are generally obtained by heat treatment of coke with an excess amount of potassium hydroxide.^[5] Recently a synthetic procedure has been developed to produce carbon with uniform pore size distribution. In this case an inorganic porous template, like a silica matrix is used to define the porosity of the carbon material.^[27,28,29] Hydrocarbons or an organic precursor is adsorbed on the porous silica and then subjected to pyrolysis. The template is then chemically removed, leaving well ordered pores of uniform size in the carbon material, which is chemically rather inert. The advantage of using materials with well defined texture and pore size distribution consists in the

possibility to relate the adsorption properties to the textural properties of the adsorbent.

Activated carbon and porous carbons find several applications in solvent and gasoline recovery from the gas phase: owing to its high specific surface area and microporosity activated carbon adsorbs easily organic vapours developed during different industrial production steps and gasoline vapours of automotive fuel systems.^[24] Other important applications are adsorption of inorganic and organic solutes from aqueous solution, removal of pollutants from water and catalysis.

2.2.2 Metal-organic frameworks (MOFs)

The concept of polymeric frameworks based on metal ions bridged other by organic ligands was well known since the late 1980s.^[30] However, the outstanding work performed by Yaghi on this class of crystalline materials, was responsible for the real breakthrough of metal-organic frameworks. He found that the use of carboxylate rigid organic ligands to aggregate metal-ions is ideal to form extended frameworks with structural stability and high porosity. Indeed, the strong metal-oxygen bond confers exceptional robustness to the framework which does not collapse even after removal of the solvent molecules incorporated during the synthesis.^[31] The result is a crystalline ordered framework possessing low density and high specific surface area. The key to design MOFs consists in the assembly of metal-carboxylate subunits as nodes of a framework and of organic linkers in the desired network topology. An example is given by the structure of MOF-5, which is the most studied of all metal-organic framework due to its high specific surface area and to the simple and cheap starting material to produce it.

In MOF-5, Zn^{2+} ions and 1,4-benzene-dicarboxylate form octahedral $Zn_4O(CO_2)_6$ clusters linked at the vertex of a cubic frameworks by benzene groups (fig 2.10).^[32]

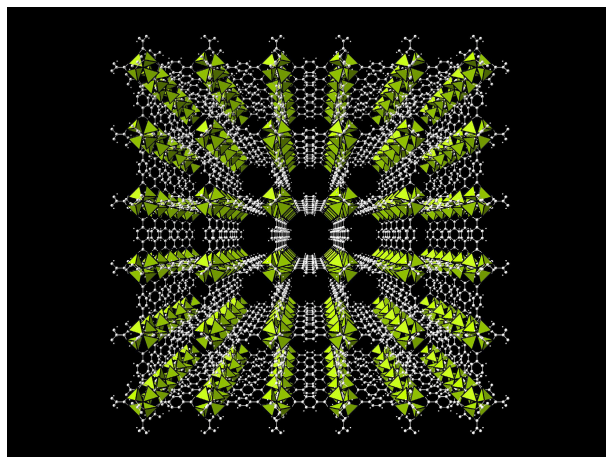


Fig. 2.10: Three-dimensional framework of MOF-5, with green polyhedra indicating the ZnO_4 tetrahedra, obtained from single crystal data in reference ^[32].

The great variety of organic ligands and metal-ions which can be used in the synthesis offers the opportunity to design different networks, with desired pore dimensions and metal centres. Nevertheless, the use of very long ligands often results in catenated networks, with smaller specific surface area and smaller pore dimensions than the corresponding non-catenated structure. Indeed if the pores of the network are large enough to accommodate the metal-carboxylate clusters a second network is built inside the first one. Two types of catenation can take place: interweaving and interpenetration. In the case of interpenetration (fig. 2.11 left) a maximal displacement between the two catenated networks is obtained, while interwoven frameworks (fig. 2.11 right) are minimally displaced and the inorganic subunits are very close to each other.^[33]

MOFs with paddle-wheel metal-carboxylate clusters, which have a square geometry, are especially interesting for catalysis and adsorption. In fact, in this type of clusters the axial coordination position of the metal ion can be occupied by a water ligand, which can be easily removed by heating. This leaves a so-called open metal site with coordinatively unsaturated metal ions which could act as strong polarizing centres for adsorbed molecules.

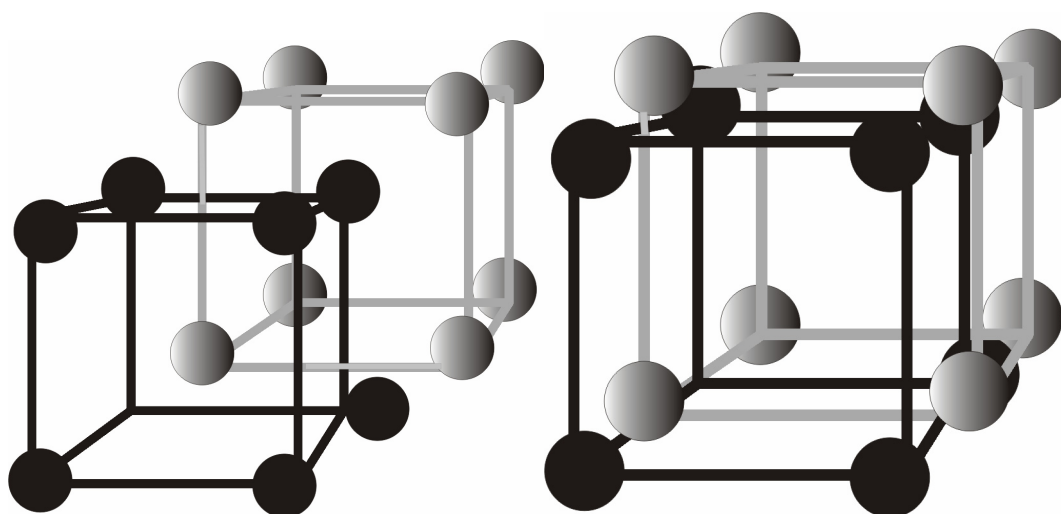


Fig. 2.11: Interpenetrated frameworks (left) and interwoven frameworks (right).

Today a great variety of different metal-organic frameworks have been synthesized and characterized, including some with SSAs up to $5000 \text{ m}^2 \text{ g}^{-1}$.^[34] In addition, MOFs can possess up to 90% of free volume and crystal densities ranging from 1 to 0.21 g cm^{-3} .^[35]

Owing to these exceptional properties they may find useful application in catalysis, gas storage and gas separation. In particular the development of new metal-organic frameworks has attracted a lot of interest for methane storage at room temperature.^[36] Some of the frameworks have possible application for sensing, due to changes in colour, in the magnetic and in the luminescence properties upon adsorption of gases, intercalation of molecules or reaction with solvents, respectively.^[37]

However, from an economic point of view, not all MOFs possessing high SSA come into question for a large scale industrial application. In fact the cost of production of the organic ligand limits the interest of industry to a reduced number of MOF structures. In the past, most metal-organic frameworks were synthesized under hydrothermal or solvothermal conditions and the synthesis was often slow and gave a very low yield. Recently, new synthetic procedures which yield MOFs on a large scale have been developed by BASF.^[38] This makes this class of porous materials much more attractive for industrial applications than carbon materials for which often only small sample masses are available. In addition, for the first time the

possibility to synthesize MOFs electrochemically in aqueous solution and under ambient conditions has been presented.^[39]

Another great advantage of crystalline metal-organic frameworks is the possibility to apply X-ray diffraction analysis to exactly determine the framework structure. The tailoring of these materials under diverse synthetic conditions is therefore supported by the possibility to know how the individual building blocks assemble and form the final structure.

2.2.3 Zeolites

Zeolites are three dimensional silicate structures built of TO_4 tetrahedrons sharing all four corners, where T typically indicates Si^{4+} and Al^{3+} ions. The general formula of zeolites is $M_{x/z}[(AlO_2)_x(SiO_2)_y] \cdot mH_2O$, where M is the non-framework exchangeable cation. The T-O-T bonds are very flexible, so that the tetrahedral units can be linked in a great number of different network topologies. Indeed, at least 28 different silica-based frameworks exist. In addition, due to this flexibility the geometry of the framework is able to adapt under diverse conditions of temperature, pressure and chemical surrounding.^[37] To maintain the electro neutrality of the structure, for every Si^{4+} substituted with an aluminium ion there is an additional extra-framework metal ion (M) adsorbed in the structure. The additional cations are usually alkali and earth alkali metal ions. The ion exchange capacity of these materials depends on both the size of the accommodating pores and on the charge of the cation. The presence of strong electrostatic forces inside the channels and pores can produce strong polarizing sites in the free volumes of the zeolite. The electrostatic field is produced by the extra-framework metal ions and it increases with increasing charge and decreasing size.

Some zeolites occur in nature, however most of them are produced synthetically usually by hydrothermal crystallization of aluminosilicate gels.

Zeolites can have a very open microporous structure with different framework types depending on the assembly of the tetrahedral building units. This assembly is determined by the Si to Al ratio. Fig. 2.12 shows two different zeolite, type A (left) and X and Y (right): In zeolite type A the sodalite cages, which are tertiary subunits

possessing the form of a truncated octahedron, are connected with each other through the square faces in a cubic framework, while in zeolite types X and Y the cages are connected through the hexagonal faces. The zeolites X and Y differ only in the Si/Al ratio but have identical frameworks. The anionic skeleton of zeolites is penetrated by channels giving a honeycomb-like structure with relatively high specific surface area up to $\sim 800 \text{ m}^2 \text{ g}^{-1}$. These channels are large enough to allow them to exchange certain ions or adsorb water and small molecules without breaking down the structure. Compared to MOFs, the framework of zeolites is thermally more stable and resistant under harsh chemical conditions.

Because of these attractive properties, zeolites have been intensively applied for technical purposes like gas adsorption, catalysis and ion exchange in aqueous solution. The largest amount of synthetic zeolites are added to detergents to remove Ca^{2+} and Mg^{2+} cations from cleaning water but they find also application in the removal of radioactive nuclei from nuclear waste.^[40] In catalysis zeolites are used in oil refining, catalytic cracking and selective oxidation.

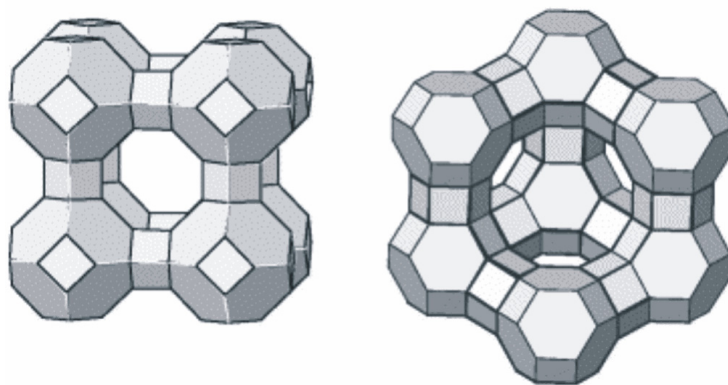


Fig. 2.12: Skeleton block of zeolite A (left), zeolite X and zeolite Y (right). Reproduced from reference ^[41]. The corners represent Al or Si atoms and in the middle of every line is one oxygen atom bridging two neighbouring Si or Al atoms.

3 Experimental Techniques

3.1 Sieverts' apparatus

Hydrogen adsorption isotherms were measured with a manually operated Sieverts' apparatus. Even though the idea behind a volumetric measurement of hydrogen sorption is very simple, many experimental errors can be introduced in this technique. According to Tibbetts et al. these errors are responsible for the exceptional results of hydrogen storage in carbon materials reported in the past.^[42] Therefore, in this section a very detailed description of the sorption measurements is reported.

The Sieverts' apparatus consists of two calibrated volumes, i.e., reservoir and sample cell, of 10.4 cm³ and 3.6 cm³, respectively, connected through a valve. All components of this set up possess VCR connections. Owing to the design with small volumes, the apparatus can be used to investigate even small quantities of material. A schematic diagram of the apparatus is shown in fig. 3.1. The pressure inside the reservoir is measured using a membrane pressure transducer with a sensitivity of 0.01 bar in the range of 1.3 bar to 100 bar. The system can be evacuated to a pressure of 1·10⁻⁶ mbar with a turbo molecular pump and the sample cell can be heated with an external heater up to a temperature of approximately 770 K.

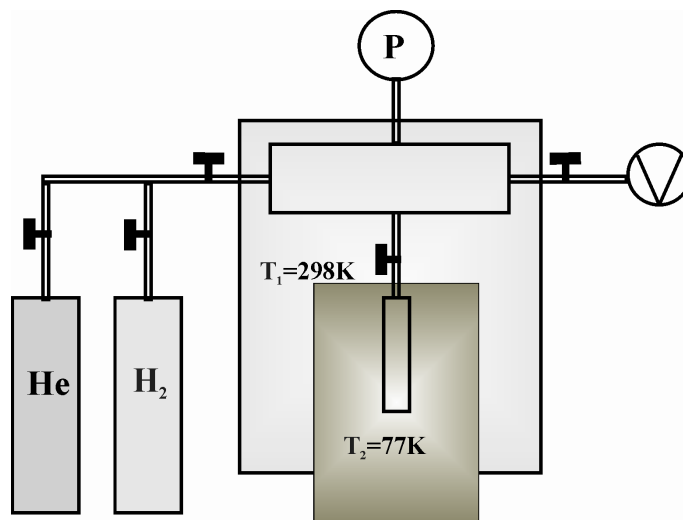


Fig. 3.1: Schematic diagram of the Sieverts' apparatus.

The apparatus was previously tested for leak absence and for accuracy through calibration with the empty sample cell and with well known metal hydrides. The storage capacity of a commercial AB₅ alloy of the type Mm(Ni,Al,Co,Mn,Fe)₅ was measured for calibration, where Mm stands for a mixture of La, Ce, Nd, Pr and small amounts of Ca. This alloy is normally used as the hydrogen containing electrode in Ni-MH rechargeable batteries. The composition of the alloy was analysed through energy dispersive X-Ray analysis (EDX), which yields an excess amount of Ni, Al, Co, Mn, Fe, compared to the AB₅ composition. This amount accounts to 14% of the total mass of the sample and does not contribute to the hydrogen storage capacity. The presence of systematic errors in the measuring technique or of a leak in the set up gives stronger deviations from the correct storage capacity in the case of smaller sample masses.^[42] Therefore, different quantities of AB₅ were used for the calibration. In the absence of systematic errors the storage capacity is independent of the quantity of sample used. For the calibration 3.2 g, 1.7 g and 0.142 g AB₅ powder were used. The smallest quantity is comparable to the sample mass typically used for the measurements on microporous samples (150 mg - 300 mg). The alloy powder was activated within the first hydrogen absorption step. Independently of the mass of AB₅ used for the measurement, a storage capacity of 1.3 ± 0.04 wt% at a hydrogen pressure of 20 bar was obtained. This result is in good agreement with literature data (~ 1.4 wt%)^[43], considering that 14 wt% of the sample does not contribute to the hydrogen storage.

The hydrogen adsorption measurements of porous materials were performed using ultra pure hydrogen gas (99.999%). In contrast to metal hydrides, which absorb selectively hydrogen, nanostructured materials with high specific surface area can adsorb all kind of gases. It is therefore essential for the measurements of hydrogen physisorption in porous materials to use very pure hydrogen gas. Prior to the measurement, the samples were heated for several hours at higher temperatures under vacuum to remove moisture and adsorbed gases from the surface of the sample.

In order to evaluate the excess hydrogen storage capacity (sect. 2.1.2), the volume of the sample has to be determined.^[44] The density of a porous sample is most appropriately measured using helium gas, whose adsorption can be neglected.^[45] Nevertheless for materials possessing low density and high porosity the absolute value of the sample's volume determined with a simple He gas expansion is usually affected by a high error. Therefore, an alternative method to measure the volume was developed. This procedure requires a non porous sample for calibration. We used sea sand whose density has been independently determined with an automatic gas sorption system using nitrogen gas. This method gives very good results for non-porous materials but cannot be used for porous samples which would adsorb nitrogen. At room temperature a calibration curve for the Sieverts' apparatus was measured using helium gas and different quantities of sea sand. An initial He pressure, P_a , of typically 50 bar was introduced in the reservoir. Then the valve to the sample cell containing a given mass of sea sand was opened and the pressure P_{ab} is recorded. The ratio P_a/P_{ab} versus the volume occupied by the sea sand sample gives a linear calibration curve shown in figure 3.2. The errors were calculated considering the sensitivity of the pressure transducer (i.e. 0.01 bar).

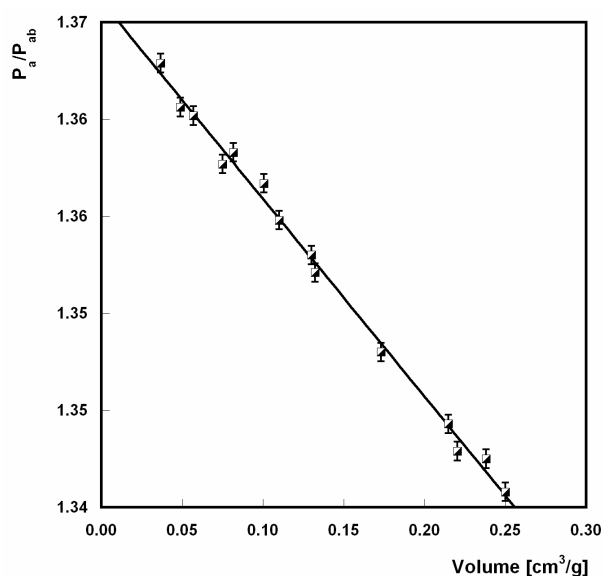


Fig. 3.2: Calibration curve of the ratio P_a/P_{ab} for helium gas versus the volume of different quantities of sea sand samples .

When the experiment was performed on the porous sample, the ratio P_a/P_{ab} was measured and using the calibration curve, the volume of the sample and the corresponding helium density was determined.

After the helium-volume of the sample was measured, the hydrogen storage capacity could be determined. The hydrogen uptake was measured at each temperature and pressure for the porous sample and subsequently for a sea sand sample, which occupied the same volume in the sample cell. Then the hydrogen pressure drop measured under the same experimental conditions for the sea sand sample and for the porous sample was compared. This comparison permits to eliminate small errors on the storage capacity due to temperature gradients between the reservoir and the sample cell, which arise especially at low temperature. The adsorption measurements can be performed at different pressures up to approximately 70 bar either at room temperature in a water bath, or at lower temperature by introducing only the sample cell in liquid gases or liquid mixtures. For low temperature measurements typically liquid nitrogen (77 K), liquid argon (87 K) or a mixture of ethanol and dry ice (200 K) were used. Each adsorption cycle of the isotherm was repeated for different hydrogen pressures and after each adsorption the sample was evacuated and degassed. This means that each storage value of an isotherm was obtained independently from the previous step. In addition, the final pressure of each adsorption step was measured after approximately 15-20 minutes, to ensure that thermal equilibrium was reached inside the small volume of the apparatus.

At high hydrogen pressures the strong deviation from the ideal gas behaviour has to be considered. For the calculation of the hydrogen storage capacity the corrected ideal gas equation (3.1) termed to the second order was therefore used^[46], where the compression factor Z for hydrogen is given in (3.2).

$$n = \frac{P}{Z} \cdot \frac{V}{R \cdot T} \quad (3.1)$$

$$Z = [1.000547 - (6.07 \cdot 10^{-7}) \cdot T] + [0.000912 - (1.0653 \cdot 10^{-6}) \cdot T] \cdot P + [(7.373407 - 0.0901 \cdot T) \cdot 10^{-7}] \cdot P^2 \quad (3.2)$$

P is the hydrogen pressure expressed in atmospheres and T the temperature, R is the ideal gas constant and V the volume.

For comparison figure 3.3 shows the hydrogen storage capacity which would be estimated using the ideal gas equation for a non adsorbing sample of 150 mg, which is comparable to the amount used in the present experiments. At 77 K and at a hydrogen pressure of 60 bar a storage capacity of approximately 8 wt% for a non-adsorbing material is calculated using the ideal gas equation. Even at room temperature an uptake of 1.5 wt% would apparently occur at 60 bar by only considering the ideal gas law.

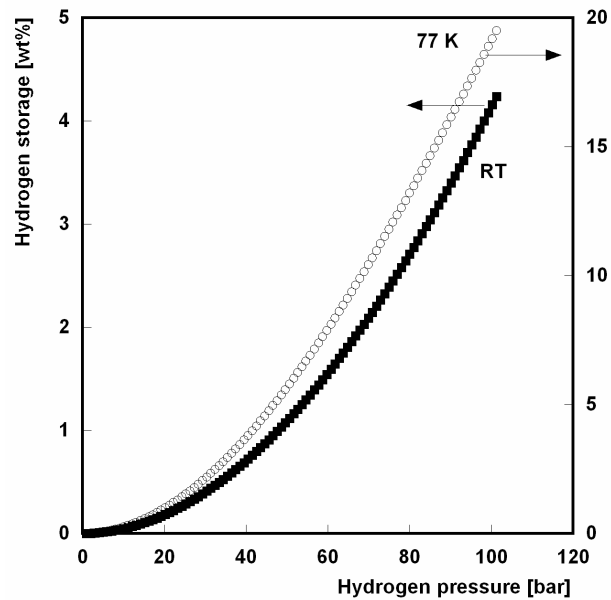


Fig. 3.3: Apparent hydrogen storage capacity of a non-adsorbing material of 150 mg versus pressure, evaluated using the ideal gas equation at RT (squares) and 77 K (circles).

3.2 Thermal desorption spectroscopy (TDS)

Thermal desorption spectroscopy is a technique to study selectively the desorption of gases from solids. For the desorption of hydrogen it is commonly applied to investigate metal hydrides and complex hydrides.^[47,48] In this case due to the high activation energies of desorption the experiment is usually performed at temperatures above room temperature. Less commonly TDS has been used to study hydrogen storage at low temperatures. The experimental difficulty in this case consists in performing the temperature programmed desorption at very low temperatures.

Fig. 3.4 shows the setup which was especially designed in our laboratory to measure desorption spectra of physisorbed hydrogen. The sample cell, (1), made of copper, and the thermocouple, (2), are introduced into a copper block, (3), in order to warrant a good thermal contact between sample and thermocouple. The copper block is surrounded by a resistive heater, (5), and can be connected to the cold finger of a flowing helium cryostat, (4), which allows to cool to 20 K. With a heat controller the temperature can be regulated with different heating rates. The desorbed gases are analysed by a quadrupole mass spectrometer, (7), which detects masses in the range from 1 to 100 amu and possesses a sensitivity of $2 \cdot 10^{-11}$ mbar.

Previous to the measurement the sample was heated in vacuum to remove moisture and adsorbed molecules. Then, at room temperature a hydrogen pressure of 25 mbar was introduced into the reactor and the sample is slowly cooled down to approximately 20 K. The temperature was held at 20 K for approximately 30 minutes, to assure that sample and copper block were at the same temperature. Subsequently the system was evacuated to remove the non-adsorbed hydrogen molecules. Owing to the low temperatures of the sample, adsorbed H₂ sticks to the surface of the adsorbent even under vacuum, while the free molecules can be easily pumped off. Then the temperature program was started with a constant heating rate of 0.03 K s⁻¹ or 0.1 K s⁻¹ and the signal of desorbed hydrogen was recorded with the mass spectrometer. In addition the masses 1 and 18 of atomic hydrogen and water, respectively, were measured.

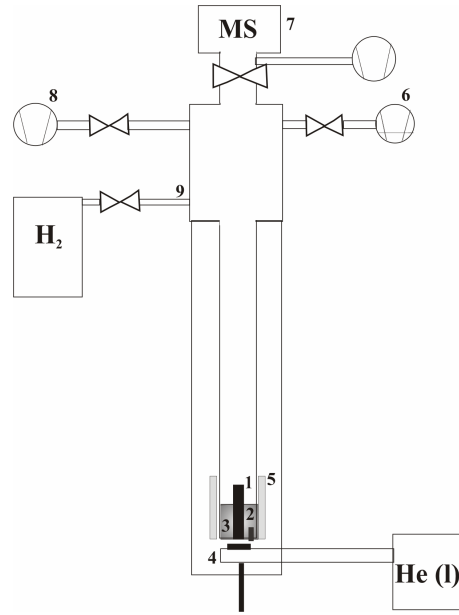


Fig. 3.4: Setup for thermal desorption spectroscopy. The indexed parts are: sample cell (1), thermocouple (2), copper block (3), He cryostat (4), heater (5), pressure gauge (6), mass spectrometer with turbo molecular pump (7), turbo molecular pump (8), hydrogen inlet (9).

Thermal desorption spectroscopy is a very selective and sensitive technique, and usually sample masses of less than 3 mg are enough to measure accurately a spectrum. In order to use TDS as a quantitative method a calibration is necessary.^[49] In the region of linear response of the mass spectrometer and using a constant pumping speed, the measured signal $I(t)$, which is an ionisation current, is proportional to the desorption rate as shown in eq. (3.3).

$$I(t) = \alpha \cdot \frac{dn(t)}{dt} \quad (3.3)$$

Here α is the proportionality constant and $n(t)$ the number of molecules desorbed at the time t .

Integrating (3.3) between the initial time t_l and the final time t_0 gives:

$$\int_{t_0}^{t_l} I(t) dt = \alpha \int_{t_0}^{t_l} \frac{dn(t)}{dt} dt \quad (3.4)$$

The integral on the left of equation (3.4) corresponds to the area, A , of the desorption curve, and the integral on the right is the total number N of desorbed hydrogen molecules. Equation (3.4) can be written in the form

$$A = \alpha \cdot N \quad (3.5)$$

It is possible to measure the proportionality constant α by calibrating the instrument with a well known standard. Pd powder has been used for the calibration. The Pd sample is loaded at room temperature with 0.7 bar of hydrogen. The corresponding amount of stored hydrogen can be calculated using equation (3.6) :^[50]

$$\ln p_{H_2} = -A(T) + B(T) \cdot x \quad (3.6)$$

x is the H/Pd atomic ratio, p_{H_2} is the hydrogen pressure and A and B are temperature dependent constants. Equation (3.6) yields at 0.7 bar a value $x = 0.7$, which corresponds to a storage capacity of 0.66 wt%.

After the absorption, the PdH_{0.7} sample was rapidly cooled to approximately 20 K in order to prevent hydrogen desorption during evacuation of the system, before starting the temperature program. Fig. 3.5 shows the hydrogen desorption spectrum of PdH_{0.7} recorded with a heating rate of 0.1 K s⁻¹. Here the hydrogen pressure in vacuum and the sample's temperature are measured as a function of time. Owing to the constant heating rate, the hydrogen pressure can as well be reported versus the applied temperature. The two distinct peaks measured at 272 K and 320 K are attributed to the β -region and to the $\alpha+\beta$ -region of the phase diagram of PdH_x.^[51]

The setup was also tested under the same experimental conditions, i.e. after introducing a hydrogen pressure of 25 mbar and cooling down to 20 K, with the empty sample cell and with sea sand. The amount of hydrogen which is simply adsorbed on the walls of the setup and on of the sample cell accounts for a storage capacity, which is less than 0.01 wt% on a sample of 3 mg and is therefore negligible.

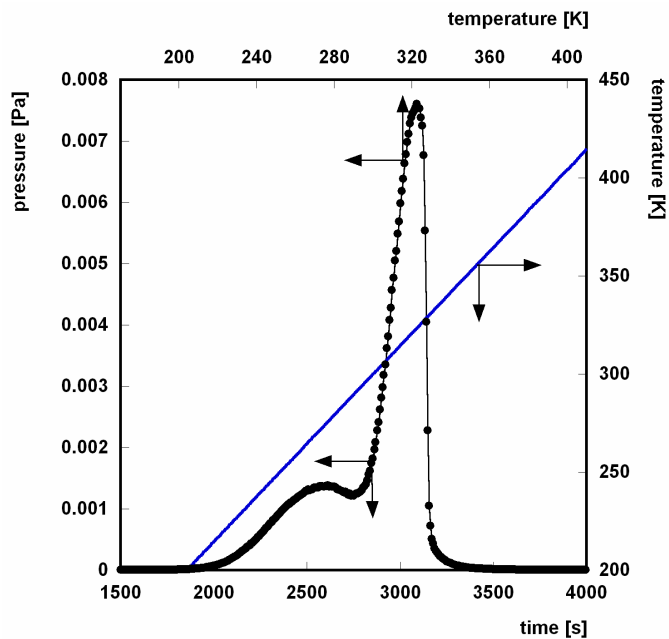


Fig. 3.5: Thermal desorption spectrum of hydrogen in Pd obtained with a heating rate of 0.1 K s^{-1} . The hydrogen pressure is reported versus time (black dots). The temperature is reported versus time (blue line).

Thermal desorption spectroscopy is not only a technique, to measure the amount of hydrogen adsorbed in a sample. More commonly it is applied to have information about the interaction of the adsorbed molecules with the adsorbent. Indeed, high desorption temperatures are characteristic of strong interactions between hydrogen molecules and adsorption sites, while weakly adsorbed H_2 molecules are desorbed at temperatures close to the critical temperature of hydrogen. A desorption spectrum possessing more desorption maxima at different temperatures indicates the presence of distinct adsorption sites possessing different potentials of adsorption.

TDS is often used to calculate the activation energy of desorption from the temperature of the desorption maximum. Here, two methods are proposed, which base on the measurement of the peak-maximum position: For coverage independent desorption parameters and first-order kinetics the activation energy for desorption correlates to the temperature of the peak maximum T_m and to the heating rate β , according to the Redhead's peak maximum method: ^[52]

$$E = RT_m \left[\ln \left(\frac{\nu T_m}{\beta} \right) - 3.64 \right] \quad (3.7)$$

Here ν is the pre-exponential factor for desorption, which describes the frequency of vibration of the hydrogen molecule in the adsorbed phase. This equation is usually applied to determine E from a single spectrum, however a value for ν has to be chosen. The usual choice is 10^{13} s^{-1} . The second method is based on the heating rate variation^[52]. The method requires a number of spectra corresponding to the same initial coverage, but measured with different heating rates.

$$\ln \frac{T_m^2}{\beta} = \frac{E}{RT_m} + \ln \frac{E}{\nu R} \quad (3.8)$$

Plotting $\ln(T_m^2/\beta)$ versus $1/T_m$ for different heating rates provides the activation energy of desorption, E , from the slope. This method requires at least a change of one order of magnitude in β to give accurate values of the activation energy of desorption.

In conclusion thermal desorption spectroscopy is a technique which after calibration offers the possibility to measure the amount of hydrogen desorbed from a sample and to determine the temperature of desorption. The desorption temperature is related to the activation energy of desorption and therefore to the affinity of the adsorbate with the adsorbent. The number of desorption peaks present in a desorption curve is correlated to the number of adsorption sites with different adsorption potential.

3.3 Raman spectroscopy

The experimental set up used to study the Raman effect in free and adsorbed hydrogen is shown in fig. 3.6. For these experiments a special Raman cell in stainless steel and with a suprasil window was built (fig. 3.7), suitable for measurements at low temperatures and both high pressures up to 30 bar and vacuum. Usually, only half of the cell was filled with the porous sample, so that in the lower part, mainly the signal of the adsorbed hydrogen was measured, while in the upper part of the cell it was possible to measure the free hydrogen gas, under the same conditions of temperature and pressure. The cell was introduced into a liquid helium flow cryostat and the temperature was measured directly at the cell with a thermocouple. The temperature of the Raman cell could be regulated with a heat controller and a resistive heater between 4 K and 300 K. The hydrogen pressure inside the cell was increased continuously between 0 and 22 bar. In addition, prior to the experiment the sample were degassed by connecting the Raman cell directly to a turbo molecular pump.

For excitation an Ar⁺ ion laser with emission line at 514 nm was used. The unwanted laser plasma lines were eliminated with a 30 cm prism monochromator. Then the laser beam was directed through the window of the cryostat and through the window of the Raman cell onto the sample (fig. 3.7 and 3.8) using a series of mirrors. The scattered radiation was collected by a lens, collimated and directed into the triple grating spectrometer of the type T 64000 equipped with a CCD camera. Depending on the desired resolution the grating could be configured to work in subtractive or in additive modus. In the additive configuration a best resolution of about 0.4 cm^{-1} was reached, but in this case the spectral window was reduced to an interval of only 16 cm^{-1} . In contrast, applying the subtractive modus the spectral window were increased to about 400 cm^{-1} , but as a consequence the resolution of 1.6 cm^{-1} was obtained. The spectra were calibrated with the lines of an Ar or of a Xe-lamp near to the transitions lines of hydrogen.

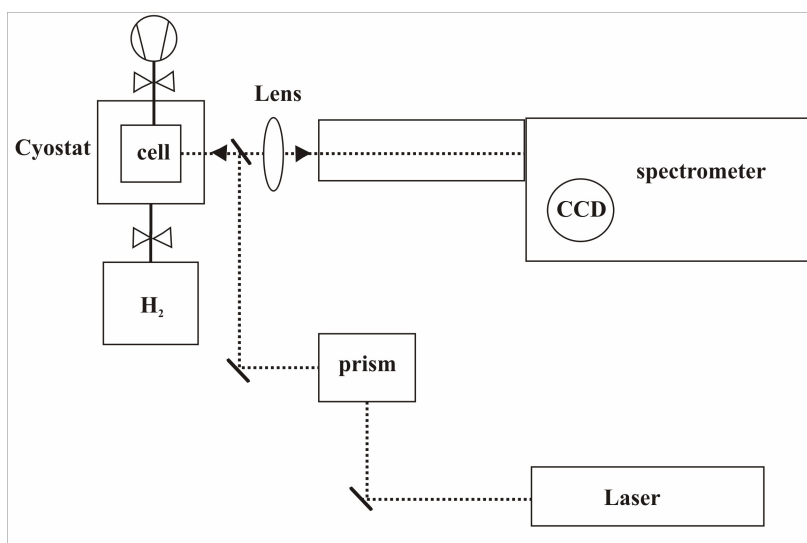


Fig. 3.6: Simplified diagram of the setup for Raman experiments.

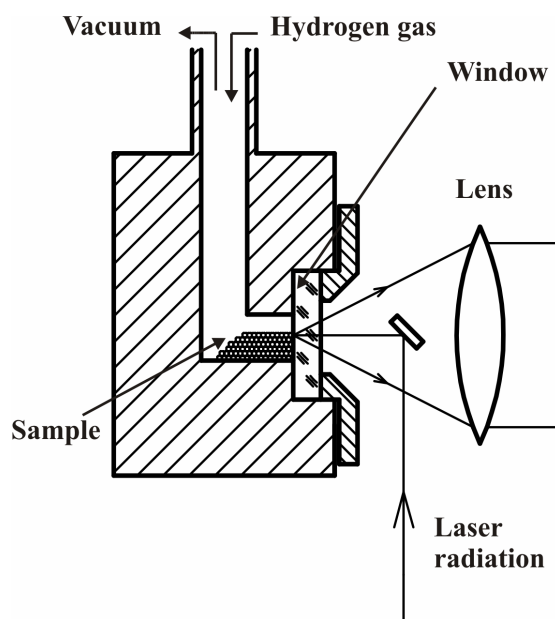


Fig. 3.7: Section of the Raman cell with the connection to the hydrogen supply or the vacuum pump. For simplicity the cryostat is omitted. The sample is positioned in front of the cell window. A mirror reflects the radiation onto the window and onto the sample and the backscattered radiation is collected by a lens.

4. Carbon materials

4.1 Sample preparation and characterization

Various carbon materials possessing different texture and structure were obtained from different suppliers worldwide for this study.

Firstly, different types of tubular carbon with specific structures were selected. Amorphous carbon nanotubes were produced by DC arc discharge in an atmosphere of hydrogen gas at temperatures above 300°C.^[53] These nanotubes are hollow pipes with a diameter ranging from 10 to 15 nm, and the walls show no long-range ordered structure. In fact, the temperature in the arc discharge chamber is lowered very fast due to the high thermal conductivity of hydrogen gas, used as a medium. This leads to the development of an amorphous structure instead of highly ordered bundles of nanotubes. Even without purification, these samples shows high levels of purity.

Single-walled carbon nanotubes (SWCNTs), produced with the HiPco^[22] (High pressure CO disproportion) method, were purchased from CNI. This synthesis produces a high yield of well ordered SWCNTs with a narrow diameter distribution around 1 nm, however, still containing metal catalyst particles. Owing to their high atomic mass these metal particles reduce the specific surface area of the nanotubes. Therefore, this material were purified by either selective oxidation and subsequent HCl treatment (sample I)^[54] or standard purification procedures giving 98 wt% of SWCNTs (sample II)¹.

Additionally, we received SWCNTs prepared by graphite arc discharge evaporation in helium atmosphere and collecting the soot from the cold walls of the reaction chamber^[55]. These samples contain typically a high fraction of amorphous carbon and catalyst particles, which reduces the specific surface area compared to purified SWCNTs.

Other samples were produced by cracking of liquid hydrocarbons in a low voltage arc discharge or by resistive heating. This method results in a mixture of MWCNTs, SWCNTs and polyhedral nanoparticles of different compositions and are called Ros 1 and Ros 3 by the producer.^[56]

¹J. Vajo. Personal communication

Secondly, disordered porous carbon samples from different suppliers were investigated. Activated carbon I is similar to AX-21^[25], which can be obtained from the reaction of coke with KOH, giving a product with cage-like type of porosity. Activated carbons of the type like AX-21 possess a doubled specific surface area compared to regular grade activated carbon. Porous carbon samples are carbon materials with ordered pores of uniform size which were prepared by the pyrolysis of sucrose (C₁₂H₂₂O₁₁) embedded in mesoporous silica of the type MCM-48.^[57] The silica is used as template with well-defined porosity and is subsequently removed by washing with HF. This synthesis yields spherical nanoporous carbon exhibiting periodic arrays of pores.

The specific surface area and the pore dimension of the samples were measured with an automatic gas sorption system using nitrogen gas at 77 K and applying the multipoint BET method for the specific surface area, and the MP-method which is an extension of the de Boer's t-method for the micropore volume.^[58] The different carbon nanostructures possess specific surface areas ranging from approximately 22 m² g⁻¹ to 2560 m² g⁻¹, and high pore densities. The highest surface area, which was measured for high grade activated carbon, is very close to the maximum theoretical surface of a graphene sheet of 2630 m² g⁻¹ if both sides are considered.^[60]

Table 4-1 shows the texture properties of the investigated carbon materials.

Table 4-1: Texture properties of carbon nanostructures.

Sample	BET SSA [m ² g ⁻¹]	Average pore diameter [Å]	Pore volume for pores with a radius < 6.5 Å [cm ³ g ⁻¹]
Activated carbon I	2564	11.8	0.75
Activated carbon II	1857	13.9	0.65
Porous carbon I	1646	11.1	0.46
Activated carbon III	1065	18.2	0.49
Purified SWCNT I	1024	15.4	0.39
Porous carbon II	946	10.6	0.25
Purified SWCNT II	854	17.1	0.36
Porous carbon III	1164	12.3	0.38
Porous carbon IV	1515	9.9	0.37
Amorphous CNT	369	14.5	0.13
SWCNTs	124	15.5	0.05
Mixture of nanoparticles I	34	11.5	0.01
Mixture of nanoparticles II	22	11.3	0.0065

4.2 Volumetric measurements

4.2.1 Results

Figure 4.1 and 4.2 show the hydrogen adsorption isotherms of activated carbon I and of purified SWCNTs II, respectively, at 77 K and at room temperature. Each point of the adsorption isotherm was obtained independently from the previous one after heating the sample at 473 K in vacuum. This explains why the uptake values can have some scatter at higher hydrogen pressures. The adsorption process was very fast and the equilibrium pressure was reached within a few seconds. During waiting for another 15 minutes no further pressure change was observed.

At 77 K all investigated carbon materials show a type I adsorption isotherm with an initial steep increase of the hydrogen uptake at low pressures and a horizontal plateau at higher pressures. This type of isotherms is characteristic for monolayer adsorption on microporous solids.^[7,60] The adsorption isotherms at 77 K were described with a Langmuir equation, which yields the saturation value, from the plateau of the fit (eq. 2.1). At room temperature the hydrogen adsorption isotherms of the carbon nanostructures show a linear Henry-type behaviour.

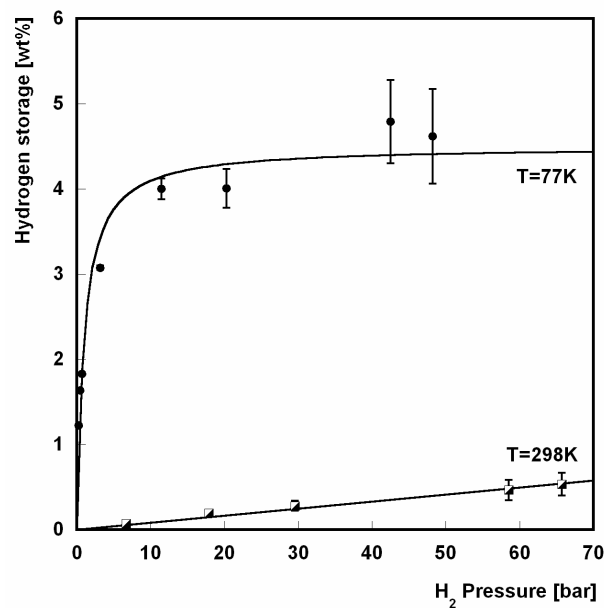


Fig. 4.1: Hydrogen adsorption isotherms of activated carbon at room temperature and at 77 K.

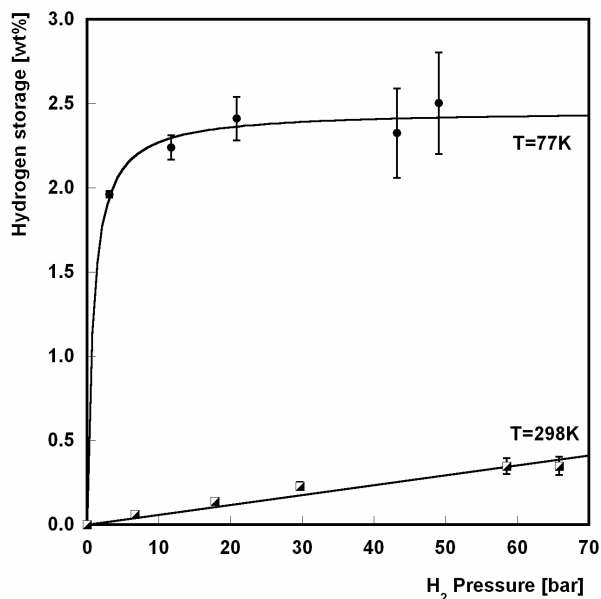


Fig. 4.2: Hydrogen adsorption isotherms of purified SWCNTs at room temperature and 77 K.

The hydrogen storage capacity and the shape of the isotherm are independent of the number of adsorption cycles which clearly indicates that hydrogen is stored reversibly in these carbon materials. Furthermore for activated carbon I the measurements at pressures less than 1 bar were performed using a microbalance. The good agreement of the uptake values measured volumetrically and gravimetrically is a further proof of the accuracy of the measurements.

At 298 K all materials show a hydrogen storage capacity which is less than 0.5 wt%, while a maximum uptake of 4.5 wt% is obtained at 77 K for high grade activated carbon, which is the best material analysed. For samples possessing a specific surface area less than $400 \text{ m}^2 \text{ g}^{-1}$ very low storage capacities are obtained, so that it was impossible to measure a whole adsorption isotherm. In fact, small uptakes at low pressures are affected by substantial errors. For these samples only the hydrogen storage capacity measured at the highest pressure is considered.

Table 4-2 shows the hydrogen adsorption properties of the investigated carbon materials at 77 K and room temperature. The maximum uptake corresponds to the

saturation value, which was obtained from the fit to the Langmuir equation. The error on the hydrogen uptake was estimated considering on each point of the isotherm the uncertainty deriving from the measurement of the sample's volume. In addition the larger the sample mass the smaller is the error calculated for the storage capacity.

The hydrogen uptake of the different carbon nanostructures is correlated to their BET specific surface area, (fig. 4.3). In this case the hydrogen storage values of each sample are the saturation values corresponding to the plateau of the isotherm at 77 K and the uptake measured at a pressure of 65 bar at RT. An almost linear relation between the storage capacity and the specific surface area is obtained both at room temperature and at low temperature. Furthermore the uptake per SSA is independent of the type of nanostructure investigated. The experimental curve has a slope of $(2.0 \pm 0.2) \cdot 10^{-3}$ wt% $m^{-2}g$ at 77 K and $(0.23 \pm 0.05) 10^{-3}$ wt% $m^{-2}g$ at RT.

In addition, a good correlation is found between the hydrogen storage capacity and the pore volume of the carbon samples considering small pores with a radius less than 0.65 nm. Fig. 4.4 shows this correlation both at 77 K and at room temperature, yielding a slope of (6.2 ± 0.6) wt% $cm^{-3}g$ and (0.7 ± 0.1) wt% $cm^{-3}g$, respectively.

Tabelle 4-2: Hydrogen adsorption properties of carbon materials.

Sample	Hydrogen storage at saturation and 77 K [wt%]	Hydrogen storage at 298 K and 65 bar [wt%]	Isotherm fig.
Activated carbon I	4.4 ± 0.4	0.5 ± 0.1	Fig. 4.1
Activated carbon II	3.8 ± 0.2	0.37 ± 0.06	Fig. A-2
Porous carbon I	2.7 ± 0.5	0.2 ± 0.1	Fig. A-3
Activated carbon III	2.7 ± 0.1	0.32 ± 0.05	Fig. A-1
Purified SWCNT I	2.1 ± 0.3	0.35 ± 0.06	Fig. A-5
Porous carbon II	2.2 ± 0.3	0.22 ± 0.06	Fig. A-4
Purified SWCNT II	2.4 ± 0.3	0.32 ± 0.06	Fig. 4.2
Porous carbon III	2.6 ± 0.3	0.30 ± 0.06	Fig. A-6
Porous carbon IV	3.3 ± 0.3	0.35 ± 0.06	Fig. A-7
Amorphous CNT	0.9 ± 0.5	0.1 ± 0.1	-
SWCNTs	0.5 ± 0.6	0.1 ± 0.1	-
Mixture of nanoparticles I	0.1 ± 0.1	0.0 ± 0.04	-
Mixture of nanoparticles II	0.1 ± 0.1	0.0 ± 0.04	-

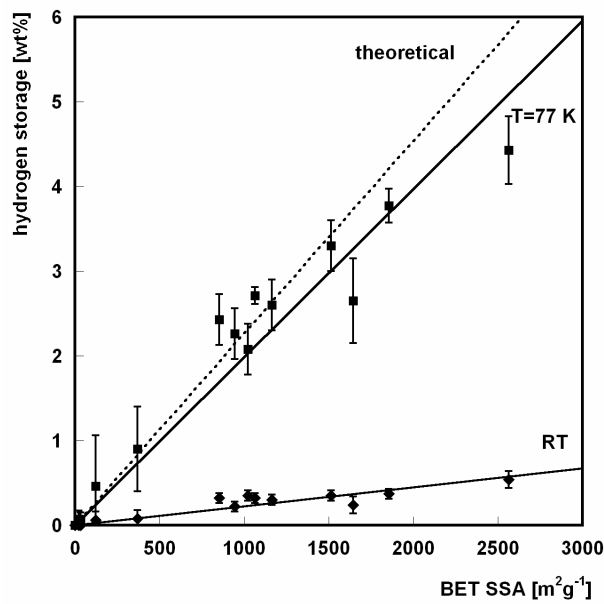


Fig. 4.3: Hydrogen storage capacity as a function of the BET SSA at 77 K and room temperature, compared with the theoretical model (dotted line) see 4.2.2.

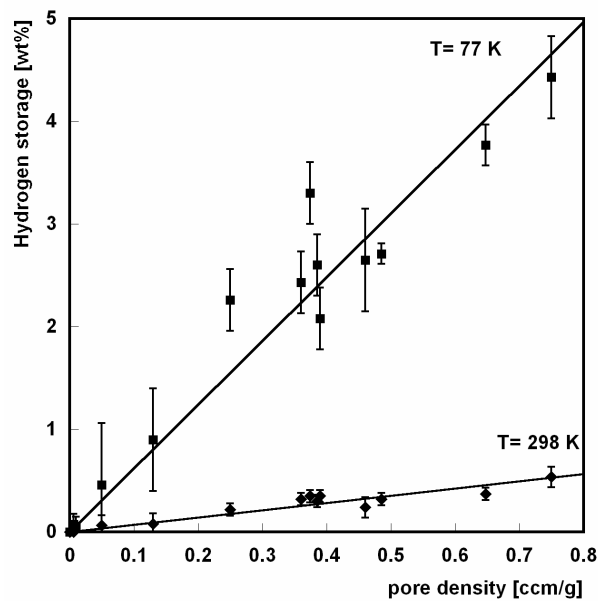


Fig. 4.4: Hydrogen storage capacity at 77 K and room temperature as a function of the pore volume of small pores with radius less than 6.5 Å.

4.2.2 Discussion

For all carbon nanostructures the adsorption isotherm at 77 K can be well described by a Langmuir type equation (e.g. fig. 4.1). The applicability of the Langmuir model together with the reversibility of the adsorption are strong indications that the

predominant mechanism for hydrogen storage in carbon materials is physical adsorption in the micropores and this is valid for all carbon nanostructures investigated. For activated carbon I, which at 77 K possesses the highest uptake, an adsorption potential of -5.3 kJ mol^{-1} was determined using equation (2.6) and the tabulated values of the entropy and the enthalpy of H_2 .^[61] This adsorption potential has to be considered as an approximate value since the dependence between the adsorption energy and coverage is neglected in the Langmuir model. Even this evaluation gives a rough estimation, the low value clearly indicates that hydrogen is physically adsorbed in this porous, carbonaceous material. Chemisorption of hydrogen would require a more than ten times higher energy of adsorption.^[62,63] This conclusion is also supported by the very fast kinetics of the adsorption process, which is typical for non-activated physisorption.

In contrast to low temperature measurements, at room temperature the adsorption isotherms are far from saturation and were described with a linear equation, according to the Henry-type behaviour. In fact, at these temperatures the thermal energy of the hydrogen gas corresponds to 6 kJ mol^{-1} , i.e. $5/2 RT$, which is high compared to the adsorption energy. Only fractional coverage takes place and the adsorbed molecules behave like a two-dimensional ideal gas.

The experimental results show that the hydrogen storage capacity depends linearly on the SSA of the carbon material both at room temperature and 77 K and is independent of type of nanostructure, curvature or array of the graphene sheets. This correlation indicates that for all carbon materials the hydrogen storage is based on simple surface adsorption. Similar results of a linear relation between hydrogen uptake and apparent specific surface area of carbon materials have been obtained by Nijkamp et al.^[26] with a slope of $1.5 \cdot 10^{-3} \text{ wt\% m}^{-2} \text{ g}$ at a pressure of 1 bar and 77 K and by Texier-Mandoki et al.^[64] with a slope of $1.7 \cdot 10^{-3} \text{ wt\% m}^{-2} \text{ g}$ at 10 bar and 77 K.

The value obtained in this work (fig. 4.3) is $2.0 \cdot 10^{-3} \text{ wt\% m}^{-2} \text{ g}$, which is slightly higher than the previously reported values, since the measurements were performed up to high pressures into the saturation regime. For the maximum hydrogen uptake on a single graphene sheet, Züttel proposed the following theoretical model:

considering that the specific surface area S_1 of a graphene sheet is $1315 \text{ m}^2 \text{ g}^{-1}$, the amount of hydrogen adsorbed can be calculated according eq. (4.9):^[65]

$$\frac{m_{\text{H}_2}}{m_{\text{C}}} = \frac{S_1 \cdot M_{\text{ad}}}{S_{\text{M}} \cdot N_{\text{A}}}, \quad (4.9)$$

where S_{M} is the surface area occupied by a single hydrogen molecule, N_{A} the Avogadro constant and M_{ad} the molecular mass of the adsorbate. S_{M} is obtained considering that the adsorbed monolayer has the density of liquid hydrogen and a close packing of the molecules in a two dimensional layer, according to eq. 4.10:

$$S_{\text{M}} = \frac{\sqrt{3}}{2} \cdot (d_{\text{M}})^2 = \frac{\sqrt{3}}{2} \cdot \left(\frac{\sqrt{2} M_{\text{ad}}}{\rho_{\text{ad}} \cdot N_{\text{A}}} \right)^{\frac{2}{3}} \quad (4.10)$$

Here, d_{M} is the diameter of the spherical molecule in the closed packed two-dimensional layer and ρ_{ad} is the density of the liquid adsorbate.

The theoretical model yields a maximum surface density of $2.28 \cdot 10^{-3} \text{ wt\% m}^{-2} \text{ g}$ (fig. 4.3). A comparison of the experimental value with this theoretical model shows that hydrogen adsorbed on carbon materials at 77 K has a density which is approximately 80% of the density of liquid hydrogen. In contrast, much lower densities are obtained at room temperature. Moreover, considering a close packed distribution of the hydrogen molecules on the carbon surface the value obtained at 77 K corresponds to a reticular distance of $\sim 4.5 \text{ \AA}$. This surface density is equivalent to six hydrogen molecules per 20 carbon hexagons. Theoretical calculations of hydrogen adsorbed on graphene layers and large polycyclic aromatic hydrocarbons to represent the graphitic surface, show that hydrogen is more strongly physisorbed above the hexagon centre.^[66,67] The regular arrangement of hydrogen molecules above the carbon hexagons which comes closest to the experimentally obtained value, corresponds to a H_2 to hexagon ratio of 1:3 as shown in fig. 4.6. Assuming this regular occupation the experimental value can be achieved by introducing approximately 10 % of vacancies in the two-dimensional H_2 -lattice.

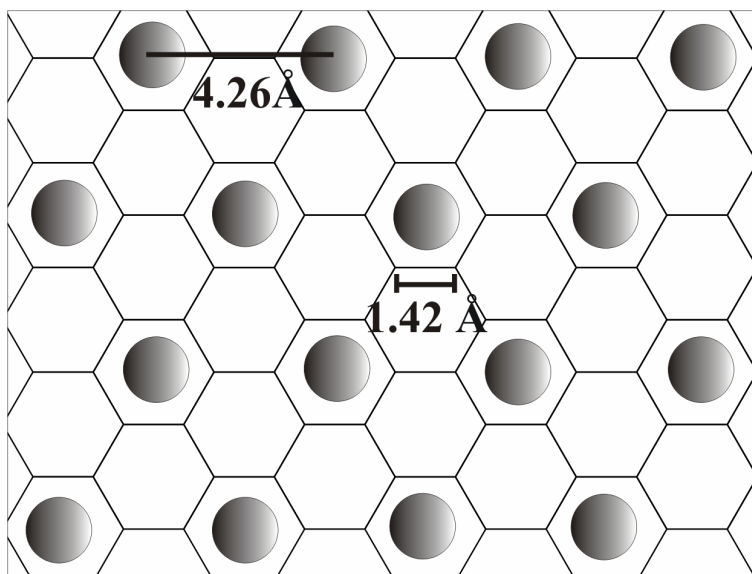


Fig. 4.6: Closed packed distribution of hydrogen molecules with a lattice parameter of 4.26 Å on a carbon surface.

In addition, several investigations indicate that the hydrogen storage capacity depends strongly on the micropore volume of the adsorbent material and not only on the SSA. De la Casa-Lillo et al.^[68] showed that at RT the hydrogen storage capacity of activated carbons and activated carbon fibres is linearly correlated with the micropore volume. These findings have been recently supported by studies on well-defined microporous carbons produced using porous silica templates with uniform pore size distribution^[69]. Also in these ordered textured carbons the hydrogen uptake at 77 K depends linearly on the micropore volume. Together these results give evidence that not only the high specific surface area but especially the presence of supermicropores, i.e. size smaller than 0.7 nm, is a crucial factor for hydrogen storage in carbons.^[64,68,69] Accordingly, the present results show that hydrogen storage is strongly correlated to the pore volume of the carbon samples especially for pores with small radius (< 0.65 nm) (fig. 4.4). Both correlations with the SSA and with the pore volume of small pores suggest that hydrogen adsorption in these carbon materials primarily takes place through micropore filling and that capillary condensation does not occur.

In conclusion, different carbon materials have been investigated with optimized texture for hydrogen adsorption. The complete reversibility, the fast kinetics and the low adsorption potential give evidence that hydrogen is adsorbed in molecular form on the surface of carbon nanostructures, i.e. pure physisorption. The amount of hydrogen physisorbed depends almost linearly on the specific surface area and the pore volume of small pores both at 77 K and at RT and is independent of the type of nanostructure. The experimental results are in good agreement with the theoretical model of hydrogen adsorbed on a single graphene layer.

4.3 Thermal desorption spectroscopy

4.3.1 Results

Figure 4.7 shows the spectrum of hydrogen adsorbed on activated carbon III obtained with a constant heating rate of 0.1 K s^{-1} . Prior to the measurements the sample was exposed to a hydrogen pressure of 25 mbar and subsequently cooled to approximately 20 K. The base pressure after evacuation was approximately 10^{-4} Pa . The pressure rise of hydrogen during desorption is three orders of magnitude above the empty sample cell. The mass 18 corresponding to water was recorded over the whole temperature range.

A small desorption peak of H_2O is observed at temperatures of approximately 200 K (fig. 4.7). However no desorption peak of water is observed in the temperature range in which hydrogen is desorbed, i.e. between 20 and 100 K.

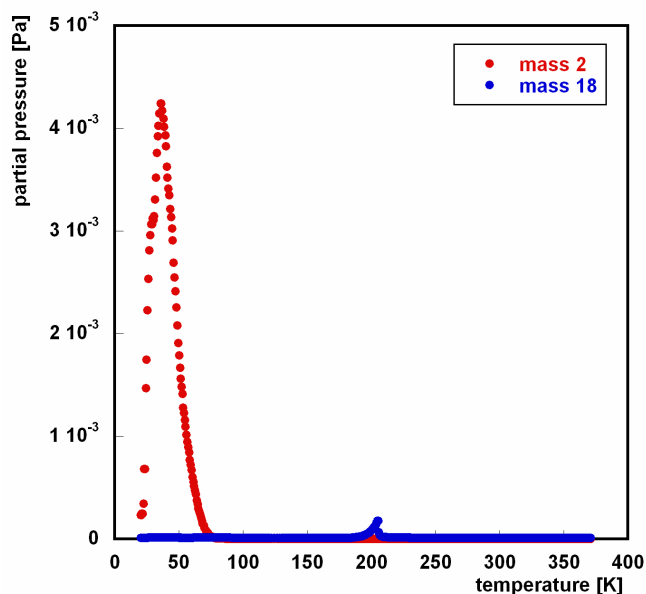


Fig. 4.7: Desorption spectrum for activated carbon III obtained with a heating rate of 0.1 K s^{-1} . Both mass 2 and mass 18 were recorded over the whole temperature range.

Figures 4.8 and 4.9 show the desorption spectrum of hydrogen in activated carbon and in purified SWCNTs II, respectively, in the range between 20 K and 120 K. The

desorption curves were both recorded up to 370 K. Above 80 K the amount of hydrogen desorbed is negligible (< 0.1 wt%) (Fig. 4.7).

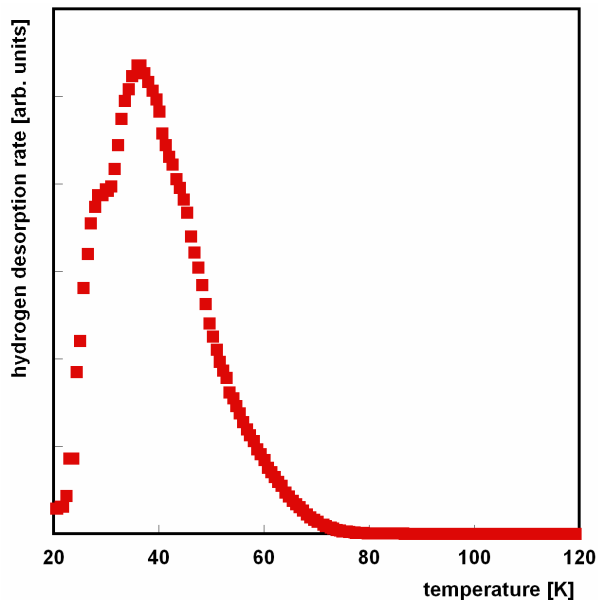


Fig. 4.8: Desorption spectrum of hydrogen in activated carbon with a heating rate of 0.1 K s^{-1} .

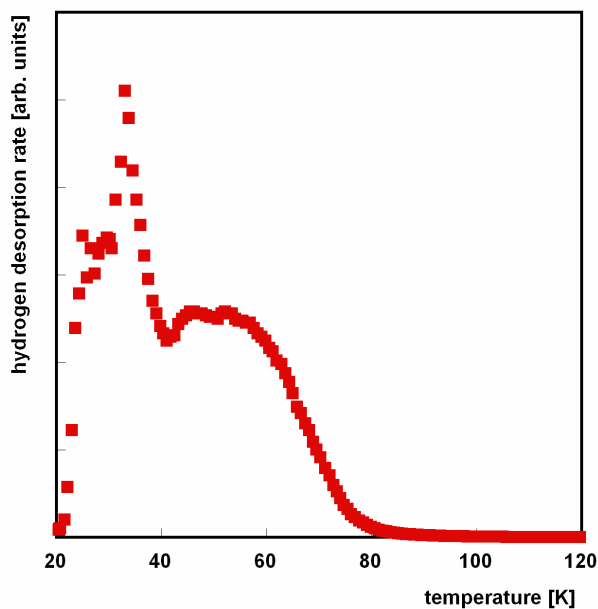


Fig. 4.9: Desorption spectrum of hydrogen in SWCNTs with a heating rate of 0.1 K s^{-1} .

Both spectra show a small shoulder around 25 K, which is often also observed at the same temperature for other samples. Apart from this low-temperature shoulder, the

shape of the thermal desorption spectra is different for both materials. For SWCNTs the desorption curve exhibits two distinct peaks, one sharp peak at a temperature of ~34 K and a broad peak at ~51 K. In contrast, for activated carbon the spectrum shows a single broad desorption peak with a maximum at approximately 37 K.

Using the calibration procedure shown in chapter 3.2 and measuring the area of the desorption curve it is possible to calculate the amount of hydrogen desorbed from the two carbon materials. The total amount of desorbed hydrogen corresponds to a storage capacity of 2.6 wt% and 2.5 wt% for SWCNTs and activated carbon, respectively. In both cases this amount corresponds with an error of 0.2 wt% to the saturation uptake measured from the adsorption isotherms at 77 K and high hydrogen pressures (fig. 4.1 and A-1), which yield a value of 2.4 wt% for SWCNTs and 2.7 wt% for activated carbon.

4.3.2. Discussion

The small desorption shoulder, which occurs at low temperatures (approximately 25 K) and is present for both carbon materials, can be attributed to some amount of liquid hydrogen or to weak adsorption of hydrogen on top of the monolayer. Indeed the desorption temperature corresponding to this shoulder is very near the critical temperature of hydrogen.

The desorption spectrum of H₂ on SWCNTs shows, in addition, two well separated desorption maxima, corresponding to different activation energies of desorption: a sharp peak at approximately 34 K and a broader peak around 51 K. The presence of two distinct peaks in the desorption spectrum is clear evidence that at least two different adsorption sites for hydrogen exist in SWCNTs, which possess different adsorption potentials.

Considering the model of a two dimensional lattice of ordered nanotubes in a bundle, four distinct sites, where hydrogen could be adsorbed, may be considered: the surface, the grooves, the interstitial channels and the pores of open nanotubes (fig. 2.9). The binding energy of hydrogen on these sites has been theoretically calculated to have the following order: $E(\text{channels}) > E(\text{grooves}) > E(\text{pores}) > E(\text{surface})$ ^[21]. No treatment to open the tubes was performed on the sample of SWCNTs II, so that

adsorption on the inner surface of the tubes can be excluded, unless defects in the tube walls give access to hydrogen in the inner pores. The sample possesses an apparent specific surface area of $854 \text{ m}^2 \text{ g}^{-1}$ measured with N_2 gas. This corresponds to the theoretical value for a bundle of approximately 7 closed SWCNTs with a diameter close to 1.3 nm.^[70] The SWCNTs investigated by TDS were produced by the HIPco method, which typically yields a smaller tube diameter of about 1 nm. Nevertheless, allowing a certain deviation, the experimental results can be explained by this model, which estimates by Grand Canonical Monte Carlo simulations the surface area and the potential energy of each adsorption site. The strongest sites are the interstitial channels with a potential energy of 11 kJ mol^{-1} . However, these sites contribute only with a SSA of $31 \text{ m}^2 \text{ g}^{-1}$ of the bundle. Owing to this small value it is possible to neglect the adsorption in the interstitial channels. The rest of the specific surface area derives from the outer convex surface and the grooves which possess theoretical potential energies of adsorption of 5 kJ mol^{-1} and 9 kJ mol^{-1} , respectively. Considering this order of energies, the hydrogen desorption peak at 34 K which corresponds to the lowest enthalpy of adsorption can be assigned to adsorption on the external surface of the carbon nanotubes. In addition the sharpness of the peak indicates that most of the molecules are adsorbed with similar energy on the surface. The desorption peak observed at approximately 51 K can be correlated to hydrogen adsorbed in the grooves. Similar results are obtained both from inelastic neutron scattering (INS)^[71] and from low temperature hydrogen adsorption isotherms of closed single-walled carbon nanotubes.^[72] By INS Georgiev et al.^[71] observed the filling of stronger binding sites at low hydrogen coverage, which are assigned to the grooves or the interstitial sites in a bundle of nanotubes. Finally, at higher coverage a second weaker adsorption site is observed, assigned to physisorption on the convex surface of the tube. T. Wilson et al.^[72] came to the same conclusion observing a two regime adsorption of hydrogen in the isotherms recorded at different temperatures: adsorption on high energy binding sites and adsorption on the graphite-like outside surface. In contrast to SWCNTs, the desorption spectrum of hydrogen in activated carbon shows a broad maximum around 37 K, which corresponds to a broad distribution of adsorption sites with similar energies. This result reflects the disordered structure of activated carbon, which consists of distances between

graphene layers ranging from a few Å up to sizes of micropores as pointed out in section 2.2.1.

A further comparison between the desorption behaviour of SWCNTs and activated carbon is presented in fig. 4.10, which shows the relation between the surface coverage, θ , and the temperature. At temperatures close to 20 K a coverage of $\theta = 1$ is assumed, since the amount adsorbed corresponds to the saturation value determined at 77 K and high pressures (see 4.1 and A-1).

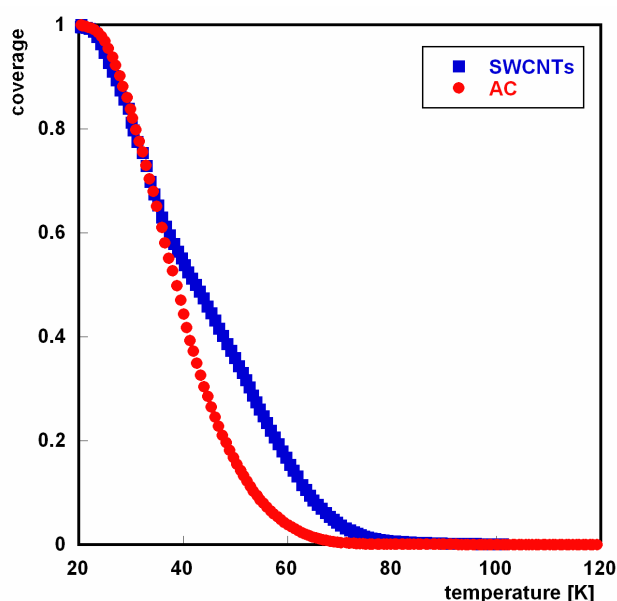


Fig. 4.10: Coverage of hydrogen adsorbed on SWCNTs (blue squares) and on activated carbon (red circles) versus temperature in vacuum.

At temperatures less than 40 K the desorption behaviour of hydrogen is similar for both carbon samples. In fact, the low desorption temperatures have been attributed to hydrogen weakly adsorbed on the external surface of the carbon material. The external surface of nanotubes and activated carbon differs only by the curvature of the nanotubes. The interaction of hydrogen with the external surface is therefore expected to be almost equal for both types of carbon nanostructures which is in good agreement with the desorption behaviour. Indeed, the heat of adsorption on a convex tube surface has been estimated to be 3.4 kJ mol^{-1} against 3.8 kJ mol^{-1} on a flat graphite surface.^[71] At higher desorption temperatures, i.e. higher energies, the

adsorption potential is influenced by pore dimensions and pore distribution of the adsorbent, which are different for activated carbon and SWCNTs. In SWCNTs the fractional coverage of hydrogen decreases more slowly with the temperature than in activated carbon, indicating stronger interactions with H₂ molecules in the adsorption sites of the nanotubes. Nevertheless, at temperature of about 80 K all hydrogen is completely desorbed from both materials.

It is very difficult to estimate the activation energies of desorption from TDS, especially when weak interactions between adsorbate and adsorbent are involved. The Redhead's analysis (eq. 3.7) yields an activation energy of desorption of 9 kJ mol⁻¹ and 13 kJ mol⁻¹ for the two adsorption sites of SWCNTs and 10 kJ mol⁻¹ for activated carbon. Compared to the adsorption potential of only -5.3 kJ mol⁻¹ calculated in section 4.2 for an activated carbon sample, the values of enthalpies obtained from TDS are very high and probably overestimated. Also theoretical calculations suggest under these conditions binding energies of only -9 kJ mole⁻¹ for adsorption in the grooves and -5 kJ mole⁻¹ for physisorption on the outer surface.^[70] Furthermore similar values are obtained from the low temperature adsorption isotherms.^[72]

In summary, it has been shown that low temperature desorption spectroscopy is a powerful technique to identify the adsorption sites for hydrogen in different carbon materials. Moreover, after appropriate calibration TDS offers an alternative method to measure the maximum hydrogen uptake of the adsorbent, corresponding to the complete monolayer coverage. In addition, the low desorption temperatures indicate that the adsorption of hydrogen on carbon materials takes place without strong binding and that all hydrogen can be reversibly removed in vacuum at temperatures above 80 K.

4.4 Raman spectroscopy of adsorbed hydrogen in carbon materials

4.4.1 Results

Figure 4.10 shows the Q-branch of free hydrogen at room temperature and 20 bar. The corresponding Q-lines are labelled in the figure. At RT the spectrum exhibits four Q-lines corresponding to the initial rotational states with $J = 0, 1, 2$ and 3 .

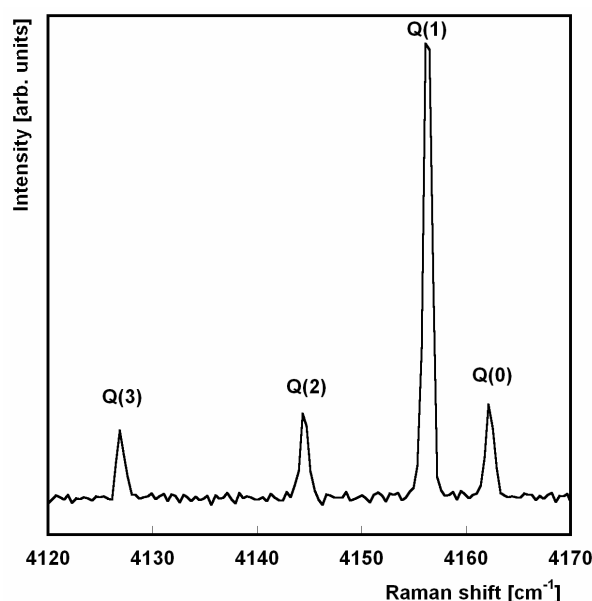


Fig. 4.10: Q-branch of hydrogen gas at 20 bar and room temperature.

In contrast, at temperatures of 40 K, only the Q(0) and Q(1)-lines can be observed, due to the low population of the excited rotational levels.

Fig. 4.10 shows the symmetric Q(1) and the Q(0)-lines of free hydrogen at 40 K and different pressures, obtained with a laser radiation of 514 nm. The Q(0)-line, corresponding to $J = 0$, occurs at higher Raman shifts around 4162 cm^{-1} (depending on the pressure), while the Q(1)-line occurs at approximately 4154 cm^{-1} .

Under the same conditions of temperature and pressure the Raman spectrum for hydrogen was measured with the cell filled with macro crystalline natural graphite (fig. 4.12). Graphite possesses a negligible porosity, and therefore it can be assumed that the fraction of hydrogen adsorbed on the surface is insignificant. Therefore, the spectrum is similar to that obtained when the Raman cell is filled only with hydrogen

gas. The difference consists in smaller intensities of the Q-lines, due to the shorter optical path of the radiation through the free hydrogen gas and in smaller broadenings.

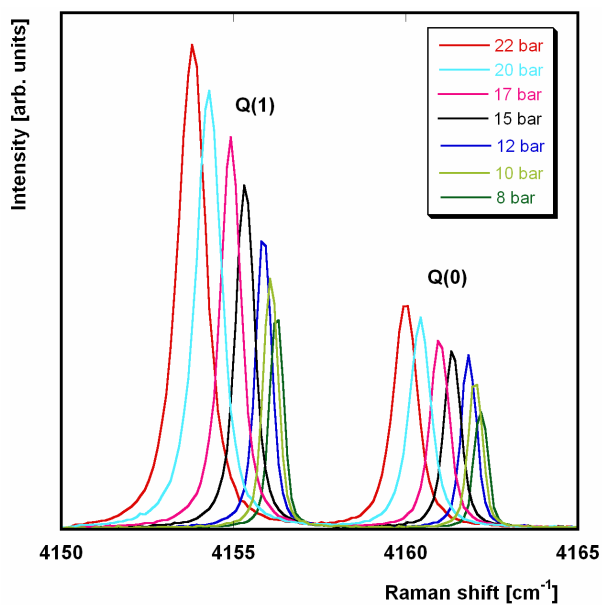


Fig. 4.11: Q(1) and Q(0)-lines of free hydrogen at 40 K and at variable pressure.

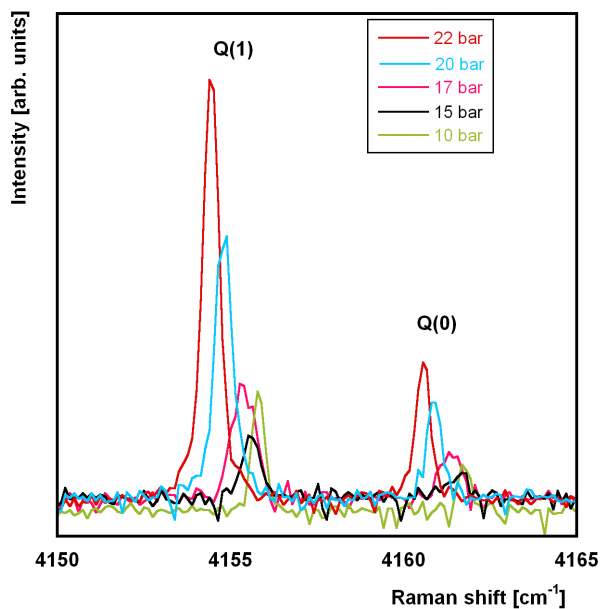


Fig. 4.12: Q(1) and Q(0)-lines of hydrogen in presence of graphite at 40 K and variable pressure.

When the Raman cell is filled with SWCNTs, the spectrum of hydrogen in presence of the sample exhibits at 40 K a different shape and pressure dependence (fig. 4.13). In particular at low hydrogen pressures only one single $Q(J)$ -peak is observed at 4162 and 4156 cm^{-1} for $J = 0$ and $J = 1$, respectively. With increasing pressure a shoulder at lower frequencies arises in both lines. Above 17 bar an additional peak occurs at lower Raman shifts. Fig. 4.14 shows as an example the $Q(1)$ -line at 40 K and 20 bar, which can be fairly well described by three distinct peaks.

A comparison with the Raman spectrum of hydrogen on graphite, i.e. non-adsorbed hydrogen, allows to assign the peak at lower Raman shifts in each Q -line to free hydrogen gas (fig. A-9). Consequently the peaks at higher Raman shifts in each Q -line can be attributed to adsorbed hydrogen. As for graphite (fig. 4.12), the peak of free hydrogen is only visible at high pressures, due to the shorter optical path. In contrast, the hydrogen adsorbed on the nanotubes gives rise to a stronger signal already at low pressures, owing to its higher density. Accordingly, for SWCNTs sample I, which is a very compact powder, the optical path through the free hydrogen gas is even smaller and only adsorbed hydrogen is measured (fig. A-8).

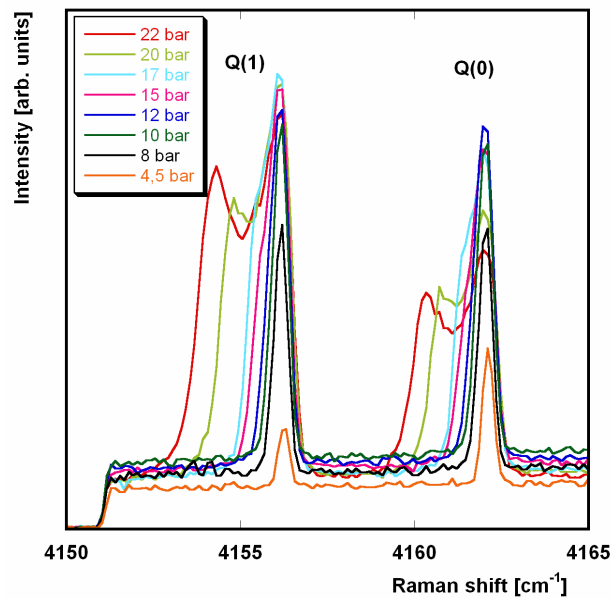


Fig. 4.13: $Q(1)$ and $Q(0)$ -lines of hydrogen adsorbed on SWCNTs at 40 K and variable pressure.

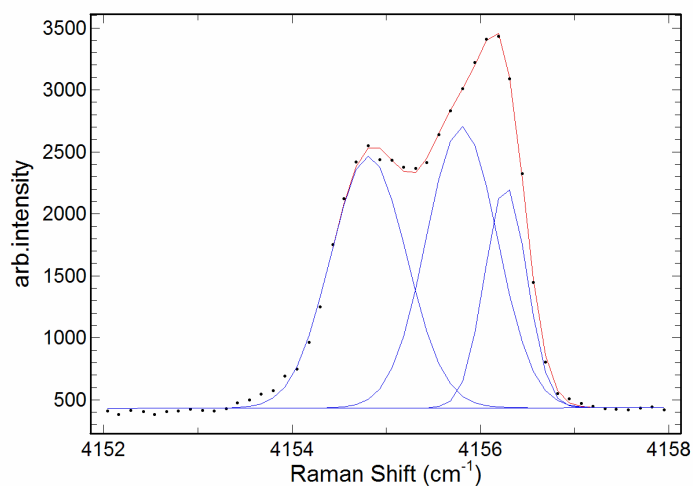


Fig. 4.14: Q(1)-line of hydrogen adsorbed on SWCNTs at 40 K and 20 bar. The dots show the measured spectrum. The red line corresponds to the sum of the three peaks shown in blue.

However, at RT no difference is observed in the Raman spectrum of hydrogen adsorbed on SWCNTs compared to free hydrogen gas. Fig. 4.15 reports the Raman spectrum of free hydrogen compared to hydrogen in presence of SWCNTs at 298 K and 20 bar.

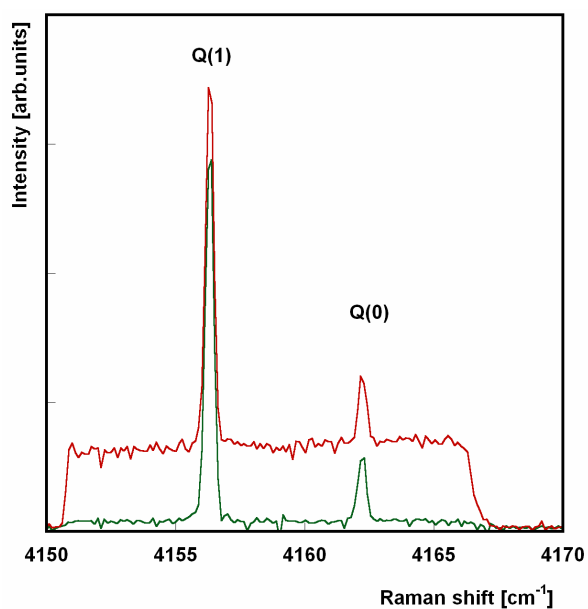


Fig. 4.15: Q(1) and Q(0)-line of free hydrogen gas (green) and hydrogen in presence of SWCNTs (red) at 20 bar and room temperature.

The higher background corresponds to the signal produced by the nanotubes. The positions of the Q-lines match perfectly for both spectra and no splitting is observed, indicating that both spectra correspond to non adsorbed hydrogen gas.

Analogous measurements were performed for hydrogen physisorbed on activated carbon, which in contrast to SWCNTs possesses a completely disordered nanostructure. Fig. 4.16 shows the Q(1) and Q(0)-peaks of hydrogen adsorbed on activated carbon at 40 K and different pressures.

A similar splitting in the Q-lines is observed for hydrogen adsorbed in activated carbon as for SWCNTs. A closer analysis of the single spectrum, reveals that each Q-line is composed of one peak assigned to adsorbed hydrogen and a second peak or shoulder at lower Raman shifts. This peak occurs at the same frequency as hydrogen gas measured in presence of graphite (fig. 4.12) and is therefore assigned to free H₂. However at the highest measured pressure (22 bar) a third peak at intermediate frequencies between the two other peaks is observed.

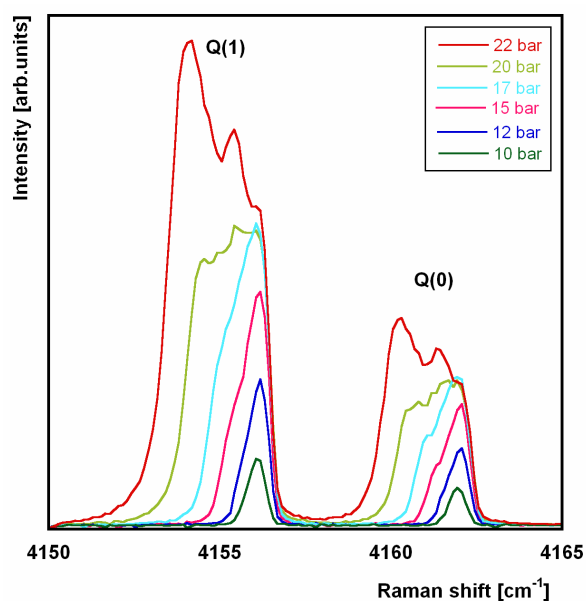


Fig. 4.16: Q(1) and Q(0)-lines of hydrogen adsorbed on activated carbon at 40 K and variable pressure.

In addition to the Q-branch, the pure rotational transition for $J = 0 \rightarrow J = 2$ was measured for free and adsorbed hydrogen. Figures 4.17 and 4.18 show the S₀(0)-line

at 40 K and variable pressure for hydrogen gas and for hydrogen adsorbed on SWCNTs (sample I), respectively.

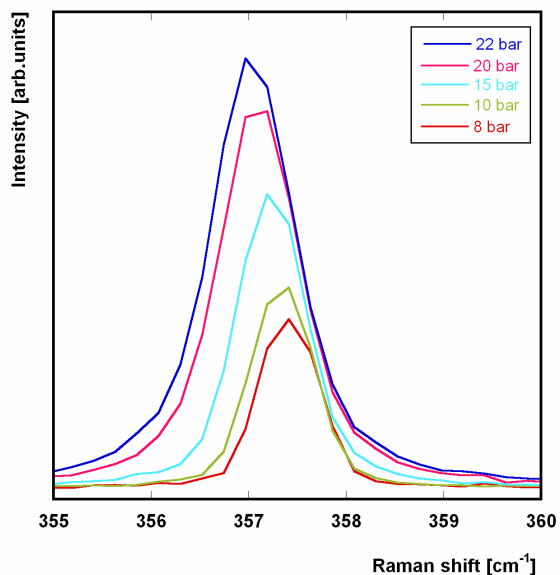


Fig. 4.17: $S_0(0)$ -line of free hydrogen at 40 K and variable pressure.

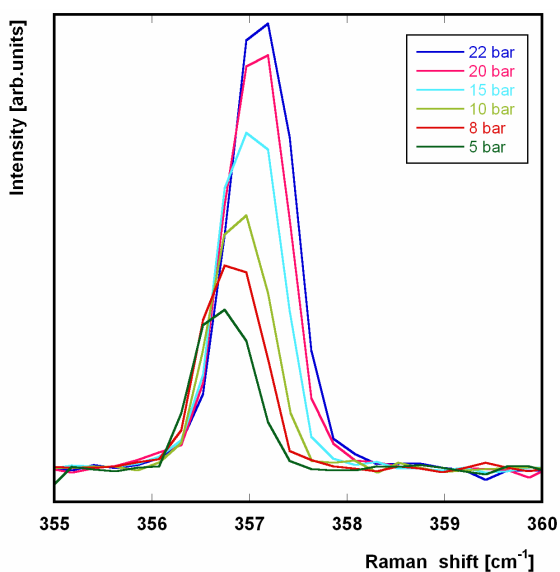


Fig. 4.18: $S_0(0)$ -line of hydrogen adsorbed on SWCNTs (sample II).

As for the Q-branch, the contribution to the spectrum of the free hydrogen is negligible for this sample. Therefore the $S_0(0)$ -line measured in SWCNTs can be assigned to purely adsorbed hydrogen. However, in contrast to the $Q(0)$ and $Q(1)$ -line no splitting of the $S_0(0)$ -line is observed.

The pure rotational spectra both for free and adsorbed hydrogen consist of one symmetric peak. For free hydrogen gas the $S_0(0)$ -line shifts towards lower wavenumbers with increasing pressure. In contrast, for H_2 on SWCNTs the Raman shift of the line increases with pressure.

Apart from measuring the roto-vibrational spectrum of free and adsorbed hydrogen, Raman spectroscopy was employed to identify and characterize the sample itself. In fact single-walled carbon-nanotubes possess characteristic phonon modes, which are influenced by the diameter, the metallic character and the presence of defects and disorder. Figure 4.19 shows the Raman spectrum of the SWCNTs II sample obtained with an excitation radiation of 514 nm. The three spectra correspond to the SWCNTs under vacuum at room temperature and exposed to a hydrogen pressure of 20 bar at room temperature and 40 K, respectively. Two distinct modes can be observed in each spectrum: the G-band, or tangential mode, which is positioned around 1600 cm^{-1} is assigned to the C-C bond in the graphitic structure; the D-band, around 1350 cm^{-1} , is related to the disorder or crystallographic defects located in the nanotube walls or ends.^[73]

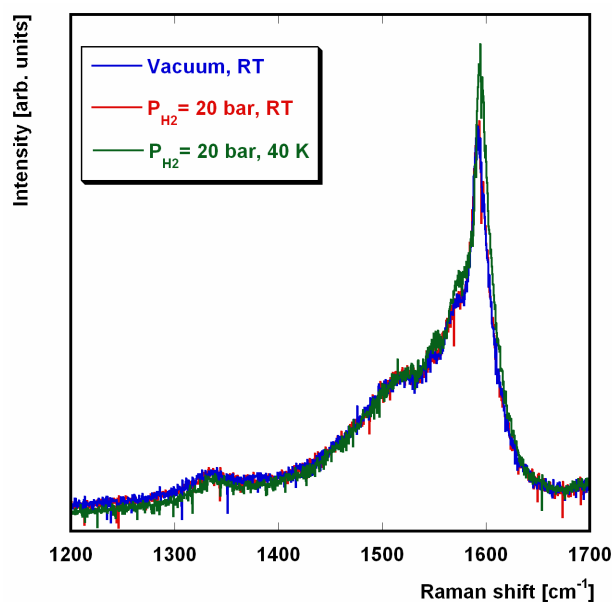


Fig. 4.19: Raman spectrum of SWCNTs, under vacuum and at room temperature (blue), under a hydrogen pressure of 20 bar, at room temperature (red) and 40 K (green).

A comparison of the spectra of SWCNTs under different conditions of temperature and hydrogen pressure shows almost no difference in the Raman spectrum of the sample under vacuum and under hydrogen gas at room temperature. Even at 40 K and 20 bar the shift of the tangential mode due to hydrogen adsorption accounts only for $+2 \text{ cm}^{-1}$.

Raman spectra are recorded also for SWCNTs (sample I) (fig. A-10), for activated carbon (fig. A-11) and graphite (fig. A-12). Graphite exhibits a characteristic single line around 1570 cm^{-1} while activated carbon presents a G-band at 1600 cm^{-1} and a strong D-band at approximately 1340 cm^{-1} .

4.3.2 Discussion

The position of the Q-band of free hydrogen depends on the density and the pressure of the hydrogen gas. It may be described conveniently in terms of a power series of the density, ρ .^[74,75,76]

$$[Q(J)]_{\rho} = Q(J) + a_J \rho + b_J \rho^2, \quad (4.11)$$

where $Q(J)$ is the frequency of the vibrational Raman transition of the free isolated hydrogen molecule in the rotational state J , a_J and b_J are J -dependent and temperature-dependent constants with $|a_J| \gg |b_J/\rho|$, $a_J < 0$ and $b_J > 0$. In particular, a_J depends on the isotropic intermolecular forces and on the vibrational coupling of pairs of molecules. Eq. 4.11 derives from a combination of repulsive and attractive intermolecular interactions, which at room temperature almost compensate each other,^[76] so that no pressure dependence of the position of the Q-line is observed. In contrast at low temperatures, i.e. at high hydrogen densities a downshift of the Q-band position is observed with increasing pressure (fig. 4.8). In the investigated pressure region a linear correlation between the position of the $Q(J)$ -lines and the pressure is obtained, indicating that the second order term is negligible (fig. 4.20).

For hydrogen adsorbed on a porous material the same dependence of the Q-line on the density is assumed (eq. 4.11). However, the vibrational frequency of the adsorbed

molecule, $Q(J)$, and the intermolecular interaction, a_J and b_J , are expected to be modified.

For SWCNTs at 40 K and high pressures each Q-line is composed of three peaks. The peak at lower wavenumbers occurring only at high pressures is assigned to free hydrogen gas, whereas the other two peaks are attributed to adsorbed hydrogen. Figure 4.20 shows the position of these two peaks in the Q(1)-line as a function of the pressure. In addition the pressure of the Q(1)-line in free hydrogen gas is shown. For free hydrogen the Q(1)-line position depends linearly on the H₂ pressure, due to the correlation to the density reported in eq. (4.11). The experimental curve for free hydrogen gas yields a $Q(J)$ value of 4157.9 cm⁻¹ from the intercept and an a_J value of -0.18 cm⁻¹ bar⁻¹ from the slope. In contrast, the position of the two peaks attributed to adsorbed hydrogen is independent of the applied hydrogen pressure. This indicates that for the adsorbed hydrogen the density does not change with pressure in this temperature and pressure region.

Nevertheless, if we assume that eq. (4.11) is valid also for hydrogen in the adsorbed state, we can use it for a qualitative analysis of the spectra.

For a given pressure P and temperature T it is possible to write:

$$[Q(J)]_{P,T}^{free} = Q(J)^{free} + a_J \rho_{P,T}^{free} \quad (4.12)$$

for free hydrogen, and

$$[Q(J)]_{P,T}^{ads} = Q(J)^{ads} + a_J^{ads} \rho_{P,T}^{ads} + b_J^{ads} \rho_{P,T}^{ads^2} \quad (4.13)$$

for adsorbed hydrogen.

For the adsorbed state the second order term cannot be neglected due to the high densities of adsorbed hydrogen. The pressure dependence shown in fig. 4.20 can be divided into two regions. In region I, at pressures below approximately 10 bar the Q-line of the adsorbed hydrogen is shifted to lower values than that of the free hydrogen. In region II, at higher pressures, Q-line is observed at higher Raman shifts than for free H₂.

According to equation (4.12) and (4.13) one possible effect causing region I is:

$$Q(J)^{ads} < Q(J)^{free}, \quad (4.14)$$

where $Q(J)^{ads}$ and $Q(J)^{free}$ are the frequencies of the vibrational Raman transition of a single adsorbed hydrogen molecule and of the isolated hydrogen gas molecule, respectively.

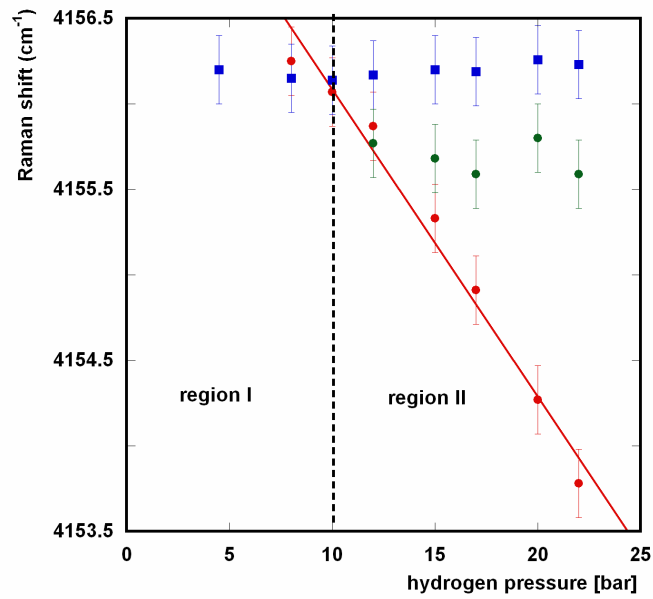


Fig. 4.20: Raman shift as a function of pressure for the Q(1)-peak of free hydrogen (red), and for the two components of the Q(1)-peak attributed to adsorbed hydrogen in SWCNTs.

The shift of the Q-line of a single adsorbed molecule compared to the free molecule is influenced by the Lennard-Jones potential between H₂ molecule and adsorbent and can be expressed in the following form^[76]:

$$\Delta \nu = Q(J)^{ads} - Q(J)^{free} = \frac{K^{rep}}{r^{12}} - \frac{K^{att}}{r^6}, \quad (4.16)$$

where the first term corresponds to the repulsive contribution between the hydrogen molecule and the adsorbent at distance r from each other and the second term is the

attractive contribution. Together with equation (4.14), $\Delta\nu < 0$ indicates that the attractive term is stronger than the repulsive interaction, as expected when the equilibrium is shifted on the side of the adsorption.

In contrast, region II can be related to higher densities of hydrogen in the adsorbed state than in the gas, i.e.:

$$\rho_{P,T}^{ads} > \rho_{P,T}^{free} \quad (4.17)$$

Indeed, while a_J is negative^[74], b_J is positive^[77], and becomes more important at higher densities due to the quadratic term in equation (4.13). Similar conclusions were obtained by Centrone et. al^[76] for hydrogen adsorbed on activated carbon.

The presence of two distinct peaks of the Q(J)-lines assigned to adsorbed hydrogen in SWCNTs may indicate the presence of two different adsorption sites. This is in good agreement with the thermal desorption measurements of hydrogen in SWCNTs, which show two distinct desorption maxima. The possibility to use Raman spectroscopy to identify different adsorption sites has been predicted by molecular dynamics simulation of a single hydrogen molecule adsorbed in carbon nanotubes^[78]. Owing to the small shift compared to free hydrogen gas, the peak occurring at approximately 4155.5 cm^{-1} could as well be attributed to weak multilayer adsorption. Similarly, Williams et al. observed for H_2 on SWCNTs and C_{60} at 85 K and pressures below 8 bar a weak splitting in the Q-lines of hydrogen.^[79] In particular they could identify for hydrogen on nanotubes a main central peak assigned to free hydrogen gas and two weakly separated shoulders at higher and lower wavenumbers, respectively, which were assigned to adsorbed hydrogen.

In all cases, the shift of the Q-lines between the free and the adsorbed hydrogen is only a few wavenumbers (fig. 4.20). This small shift points to a very weak interaction between adsorbate and adsorbent without any significant charge transfer. Similar results were obtained by Centrone et al.^[76] in measurements of the Raman shift of H_2 on activated carbon. They observed at 40 K a shift of the peak assigned to adsorbed hydrogen of approximately $2\text{-}3 \text{ cm}^{-1}$ towards higher frequencies compared to free hydrogen. Similar small shifts are also obtained in the present work for hydrogen on activated carbon (fig. 4.15) and on the SWCNTs sample I (fig. A-8)

indicating that the adsorption is almost independent of the long-range order or curvature of the graphene sheets and that the interaction of hydrogen with carbon samples is comparable for both ordered and disordered carbonaceous materials. Similar conclusions are obtained from the study of the rotational transition of para-hydrogen in different carbon nanostructured by inelastic neutron scattering.^[80] In addition, the Raman spectra of free hydrogen and hydrogen on SWCNTs measured at room temperature show no evident differences, indicating that the amount of hydrogen adsorbed under these conditions is very small. This agrees with the low uptake values determined from the adsorption isotherms (< 0.5 wt%).

Moreover, the pure rotational transition of free and adsorbed hydrogen has been investigated. In figure 4.21 the Raman shift of the S(0)-line for adsorbed and free hydrogen is plotted versus the applied hydrogen pressure at 40 K. For free hydrogen gas the Raman shift is decreasing with increasing pressure, whereas for adsorbed hydrogen it rises with pressure.

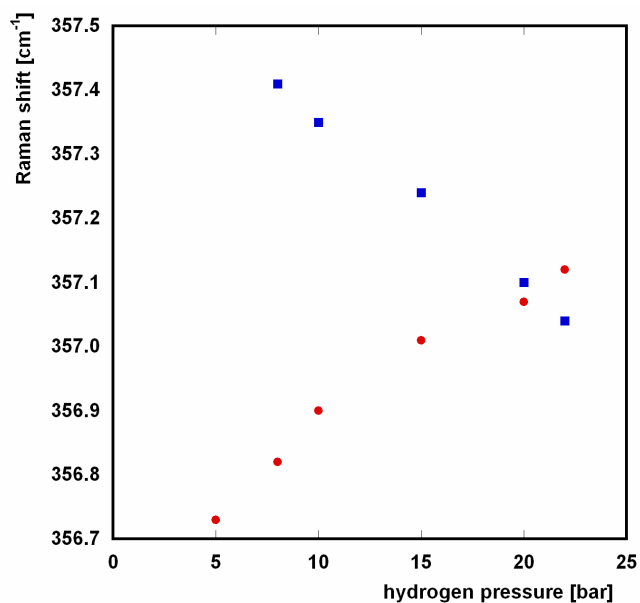


Fig. 4.21: Raman shift of the S₀(0)-line of free hydrogen (blue squares) and of adsorbed hydrogen (red circles) as a function of the hydrogen pressure at 40 K.

For the $S_0(0)$ -line position of free hydrogen gas a linear relation with the applied pressure as for the Q-line has been obtained. This experimental relation yields a slope of $-0.026 \text{ cm}^{-1} \text{ bar}^{-1}$.

For a linear molecule, which is free to rotate in the three dimensions, in the approximation of the rigid rotor the rotational energy levels are given by equation (4.17)

$$E_J = BJ(J + 1), \quad (4.17)$$

where J is the rotational number and B the rotational constant. B is inversely proportional to the square of the hydrogen bond length. If the rotational transition $J = 0 \rightarrow J = 2$ is considered, the transition will occur approximately at Raman shifts of $6B$. Extrapolating the experimental curve for free hydrogen gas at zero pressure (fig. 4.21), yields a value for $6B$ of 357.6 cm^{-1} .

In contrast, for a molecule, which is completely confined to rotate in a plane, the rotational energy levels are given by eq (4.18)

$$E_J = BJ^2 \quad (4.18)$$

Here the transition between $J = 0$ and $J = 2$ would occur at Raman shifts equal to $4B$ (238 cm^{-1}), that is at lower frequencies than for a molecule which is free to rotate in three dimensions. The Raman spectrum of an adsorbed hydrogen molecule which rotates only on the surface, would therefore exhibit a $S_0(0)$ -line at lower frequencies of about 120 cm^{-1} compared to the free rotating molecule. For adsorbed hydrogen, the experimental results show at lower pressures a downshift of the $S_0(0)$ -line compared to free hydrogen gas. However, here the shift corresponds to only -1 cm^{-1} , which is comparable to the shift in liquid hydrogen.^[81] This weak shift indicates that the adsorbed molecule is able to rotate almost freely and that only a very weak perturbation of the rotation takes place. This perturbation, even if small, reaches the maximum value at low pressures, where the H_2 - H_2 interaction can be neglected and the rotation of the hydrogen molecules is primarily influenced by the carbon surface.

Schimmel et al. observed at 15 K the rotational transition $J = 0 \rightarrow J = 1$ of hydrogen adsorbed in SWCNTs by inelastic neutron scattering. In contrast to Raman spectroscopy, the change in the nuclear spin of the molecule is permitted in INS and the transition with $\Delta J = \pm 1$ can be observed. In their work a weak splitting of the rotational peak into several components is assigned to different adsorption sites and to multilayer formation. In contrast we could not observe such a splitting in the rotational transition $J = 0 \rightarrow J = 2$, while this splitting is observed for the vibrational transition.

The Raman spectrum of the material itself shows characteristic modes of well ordered single-walled carbon nanotubes (fig. 4.22). In contrast to graphite, which exhibits only one single line corresponding to the tangential mode vibrations of the carbon atoms (fig. A-12), the G-band of SWCNTs is composed of several peaks, due to phonon wave confinement along the tubes' circumferential direction and to symmetry breaking effect associated with the surface curvature.^[82] This band is sensitive to charge transfer from dopant addition to the nanotubes.^[83]

At RT the spectra of the SWCNTs in vacuum and exposed to a hydrogen pressure of 20 bar do not show any evident difference in position or intensity. Indeed, it has been shown previously by uptake measurements, that at RT the adsorbed hydrogen is highly diluted, and the effect of the adsorbed hydrogen on the nanotube sample are expected to be very small. In contrast, at 40 K and 20 bar it can be assumed that complete surface saturation with hydrogen is reached. As calculated in sect.4.2.2, this corresponds to 6 hydrogen molecules adsorbed on 20 carbon hexagons. Despite this relatively high concentration the shift of the tangential mode due to hydrogen adsorption accounts only for $+2 \text{ cm}^{-1}$.

Rao et al. investigated the effect on the Raman spectrum of SWCNTs upon charge transfer in doped nanotubes.^[83] They found that the tangential mode was shifted to higher frequencies by about $+24 \text{ cm}^{-1}$, for electron-accepting dopants, like bromine, and to substantially lower frequencies for electron-donors, like potassium and rubidium. Both effects indicate a strong charge transfer from or to the dopant. In contrast for iodine, which is simply physisorbed on the surface of the nanotubes, they found only a shift of about -3 cm^{-1} . A similar situation as for iodine adsorbed on

SWCNTs is obtained in the present studies for adsorbed hydrogen. The weak shift is a further indication of a weak dispersive interaction between hydrogen molecules and SWCNTs occurring without charge transfer.

4.5 Summary

A great variety of carbon materials possessing different nanostructures and texture were investigated for hydrogen adsorption. The volumetric measurements show that for all materials the adsorption isotherms possess the same shape. These were described with a Langmuir model at 77 K and a Henry-type behaviour at room temperature. The mechanism is further characterized by fast kinetics and by the complete reversibility of the hydrogen adsorption/desorption process, indicating that the mechanism for hydrogen storage in carbon materials is physical adsorption. The best material, which is high grade activated carbon with an apparent specific surface area near to the maximum theoretical surface of a double sided graphene sheet, shows a maximum H₂ uptake of 4.5 wt% at 77 K. At room temperature all carbon materials possess a storage capacity of less than 0.5 wt% at pressures of 65 bar. In addition, it has been demonstrated that the storage capacity of carbon materials is correlated with the specific surface area both at room temperature and 77 K and is independent of the type of nanostructure, long range order, curvature or array of the graphene sheets. The obtained correlation is in good agreement with the theoretical model, and the maximum adsorbed density corresponds to 80% of the density of liquid hydrogen. Even though the hydrogen uptake does not depend on the structure of the carbon material, but on the SSA, different adsorption sites for H₂ can be identified for diverse nanostructures. Thermal desorption spectra of hydrogen on SWCNTs show the presence of two distinct adsorption sites for H₂ possessing different activation energies for desorption. These were assigned to hydrogen adsorbed on the convex surface of the tubes and in the grooves. In contrast, for activated carbon a broad distribution of adsorption sites with similar potentials is observed for hydrogen, which reflects the disordered structure of porous carbons. Using an appropriate calibration it was possible to quantify the amount of hydrogen desorbed from the distinct adsorption sites. For both materials the hydrogen is desorbed in vacuum at temperatures less than 80 K, which further proves that simple physical adsorption takes place and in good agreement with the adsorption results this demonstrates that the process is completely reversible even at low temperatures.

Furthermore, Raman spectroscopy was used to investigate both the effect of the adsorbent on the hydrogen molecules as well as the effect of H₂ on the adsorbent. A splitting in the Q-lines of hydrogen adsorbed on SWCNTs is observed at 40 K. In particular at high pressure three different peak components are presents. Two of them are assigned to adsorbed hydrogen, while the peak at lower frequencies corresponds to free hydrogen gas. The shift in the Raman position of the Q-lines of adsorbed hydrogen on SWCNTs compared to free hydrogen gas corresponds to less than 2 cm⁻¹ at 40 K and 20 bar and similar shifts are obtained for H₂ adsorbed on activated carbon. This weak shift indicates that no charge transfer takes place between the hydrogen molecules and the carbon material. No difference between the spectrum of free hydrogen and of hydrogen on SWCNTs is observed at room temperature and 20 bar, so that it is assumed that the amount of hydrogen adsorbed under these conditions is very small compared to free hydrogen gas. This result is in perfect agreement with the volumetric measurements which demonstrates that even at high pressures only a small amount of hydrogen is adsorbed at room temperature. Accordingly, no change in the Raman position is observed for the tangential mode of the SWCNTs upon adsorption of hydrogen at room temperature and even at 40 K and 20 bar the shift accounts for only +2 cm⁻¹ indicating a weak perturbation of the TM mode owing to van der Waals interactions with hydrogen gas. In contrast to the Q-branch of adsorbed hydrogen no splitting for the pure rotational transition $J = 0 \rightarrow J = 2$, i.e. the S₀(0)-line is observed.

5 Metal-organic frameworks

5.1 Sample preparation, structure and characterization

Different types of metal-organic frameworks, based on Zn^{2+} , Cu^{2+} , Ni^{2+} , and Al^{3+} as central metal ions and on different organic ligands were investigated.

MOF-5 or IRMOF-1 (Isorecticular metal-organic framework 1) consists of four Zn_4O clusters in octahedral subunits which are connected to each other by terephthalate groups to give a three-dimensional very porous open network^[84]. MOF-5 possesses large channels of approximately 12 Å in diameter. In reality the different orientation of the ligand in the framework produces two types of pores with slightly different diameter. Figure 5.1 shows the cubic unit cell of MOF-5 with the four Zn_4O tetrahedra (in yellow) at each corner of the cube, which share an oxygen atom in the centre of the octahedral $Zn_4O(CO_2)_6$ subunit. The representation of the crystal structure is obtained from single crystal data by Li et al.^[32]

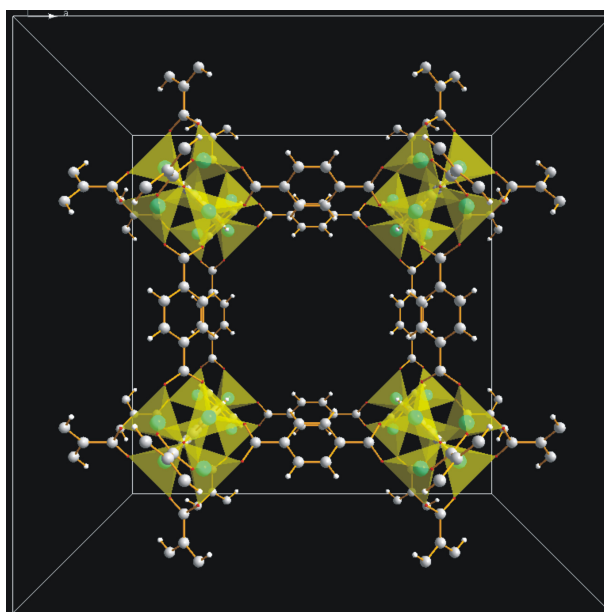


Fig. 5.1: MOF-5 unit cell, with four Zn_4O tetrahedra (yellow), which give an octahedral subunit at each corner of the cubic cell (Zn, green; O, red; C, grey; H, white).

Two types of MOF-5 samples have been investigated. High quality crystals of MOF-5 were provided by BASF^[85,38], and MOF-5 powder was prepared by a laboratory small-scale synthesis^[86].

The high quality MOF-5 crystallites were produced applying a large scale and fast synthesis which has been optimized compared to previously reported synthesis.^[31,86] This synthesis gives uniformly large crystals of MOF-5, which are activated at 60°C in vacuum after washing with acetone. Electron micrographs reveal well-shaped cubic crystals between 50 and 200 μm diameter size (fig 5.2) and the powder X-ray diffraction pattern¹ (fig. 5.3) fully matches the MOF-5 pattern derived from single crystal structure data^[32].

The BET and Langmuir specific surface areas of this sample are 2296 m² g⁻¹ and 3840 m² g⁻¹, respectively. These value is slightly higher than reported by others^[87], and they are three to four times higher than for the MOF-5 sample obtained from the small scale synthesis.^[86]

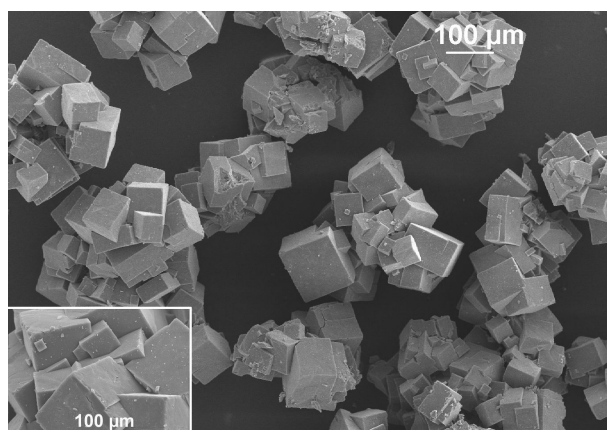


Fig. 5.2: SEM (scanning electron microscope) picture of high quality MOF-5 cubic crystals with an enlargement in the left corner.

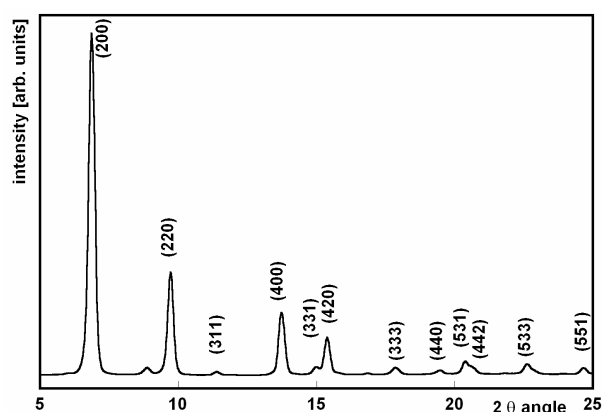


Fig. 5.3: Powder X-ray diffraction pattern (Cu Kα-radiation) of MOF-5.

¹ Powder X-ray diffraction data were recorded with a Siemens D5000 powder diffractometer using CuKα radiation and a secondary monochromator.

This laboratory synthesis of MOF-5 was performed following Huang et al.^[88] zinc nitrate and the protonated form of benzenedicarboxylic acid (BDC) were dissolved in dimethylformamide and triethylamine was slowly added to the solution. Immediately after adding the organic base a white product appeared in the solution. The same synthesis was repeated, adding 3 drops of H₂O₂ to the solution of zinc nitrate and BDC. The sample was activated by heating in vacuum at approximately 473 K for several hours. The X-ray diffraction pattern of the white solid are congruent with a Le Bail profile matching^[89] based on the crystallographic data of Li et al.^[32] showing that the product has space group Fm-3m like MOF-5, with a refined lattice parameter of 25.80 Å (fig. B-1). When H₂O₂ is added to the solution the powder consists of cubic crystallites with a size of 500 nm, showing that the peroxide favours the crystallization (fig. B-2). In contrast, without addition of H₂O₂ the same XRD-pattern is observed, but the crystallites are smaller and show no cubic shape (fig B-3). This MOF-5 sample has a BET specific surface area (SSA) of 576 m² g⁻¹ and Langmuir specific surface area of 1010 m² g⁻¹, three times smaller than the high quality MOF-5 sample provided by BASF. This difference is obviously due to the different synthetic procedure or activation of the sample, which have great influence on the porosity of the material. In fact, after the synthesis the pores of the framework still contain the organic solvent, which is removed during the activation. If the activation procedure is not optimized, the removal of the solvent molecules can partly induce the collapse of the framework, which leads to partially amorphous regions that are not visible in the XRD pattern.

The crystal structure of the Zn-based metal-organic framework IRMOF-8^[35] is in principle identical to MOF-5. The difference is given only by the longer organic ligand, which is naphthalene-2,6-dicarboxylate (NDC) in IRMOF-8. Owing to the larger distance between the Zn₄O(CO₂)₆ clusters in the cubic structure, this framework possesses larger pores than MOF-5. However, it is still unclear if IRMOF-8 can build a catenated framework with two networks grown inside each other² resulting in a structure with smaller pores compared to the non-catenated one. Indeed frameworks possessing large pore size usually favour the formation of

² O. Yaghi, oral communication at the “Heraeus seminar on hydrogen storage with novel nanomaterials”, October 2005.

catenated networks, which can accommodate the metal-carboxylate cluster of a second network inside the first one. The IRMOF-8 sample was provided by BASF and possesses a BET SSA of $1215 \text{ m}^2 \text{ g}^{-1}$ and a Langmuir SSA of $1922 \text{ m}^2 \text{ g}^{-1}$, close to the values reported in literature.^[90]

$\text{Cu}_3(\text{BTC})_2(\text{H}_2\text{O})_3$ or Cu-BTC consists of $\text{Cu}_2(\text{COO})_4$ -paddle wheels with copper dimers as four connectors and benzene-1,3,5-tricarboxylate as three connectors in a cubic wide-open framework.^[91,37] Each Cu^{2+} ion is also coordinated by a water molecule in axial position, which can easily be removed in vacuum or by heating at temperatures above 373 K. The structure of Cu-BTC consists of main channels of a square cross-section of ca 9 \AA in diameter and tetrahedral side pockets with a diameter of ca 5 \AA which are connected to the main channels by a triangular window of 3.5 \AA in diameter.^[92] Figure 5.4 represents the unit cell of Cu-BTC along the [100] direction and gives a direct view on the main channel. Figure 5.5 shows the same structure along the [111] direction with a sight on the triangular windows of the smaller side pockets. For simplicity a planar representation of the unit cell was chosen in this last case. In order to give a three dimensional character to the figure, the darker atoms indicate that their position is deeper in space along the [111] direction than the brighter atoms. The crystallographic representation is based on the single crystal X-ray analysis of Chui et al.^[91]

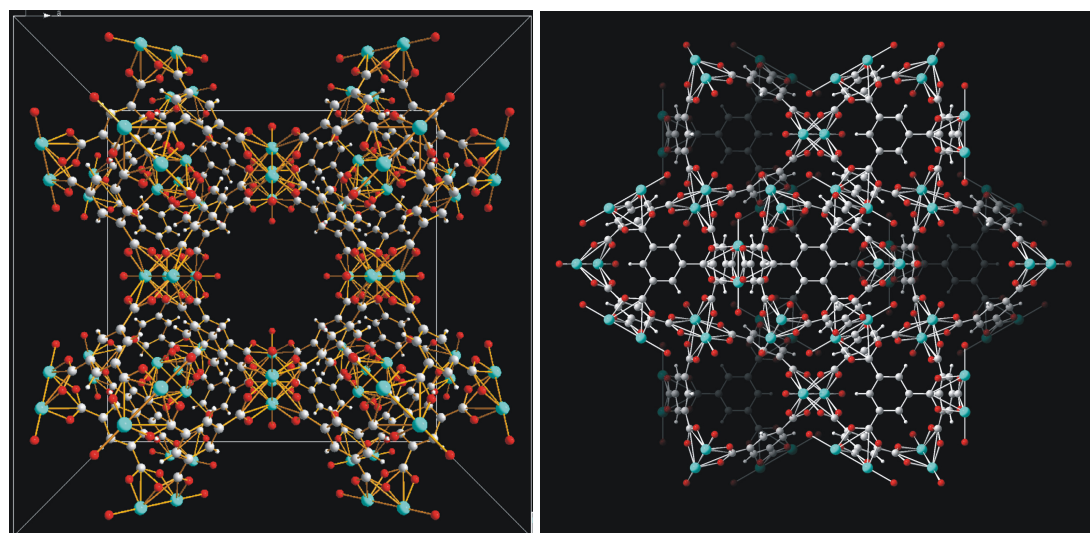


Fig. 5.4 (left): Unit cell of Cu-BTC along the [100] direction constructed from single crystal data in reference^[91] (Cu, green; O, red; C, grey; H white). The larger pore is in the middle of the cell.

Fig. 5.5 (right): View on the side pockets with triangular window along the [111] direction (Cu, green; O, red; C, grey; H, white).

Cu-BTC was provided by BASF and was produced by an electrochemical procedure,^[39] which is a new synthetic method compared to the previously reported synthesis under hydrothermal conditions^[91-94]. The obtained crystals have double sided pyramidal shape and a size of maximum 6 μm (fig. 5.6). The powder XRD pattern match perfectly with the single crystal analysis reported in literature^[91] (fig. 5.7). The specific surface area of the sample is 1154 $\text{m}^2 \text{g}^{-1}$ and 1958 $\text{m}^2 \text{g}^{-1}$ using the BET and the Langmuir equation, respectively, which is as high as reported for crystals produced under hydrothermal conditions.^[94]

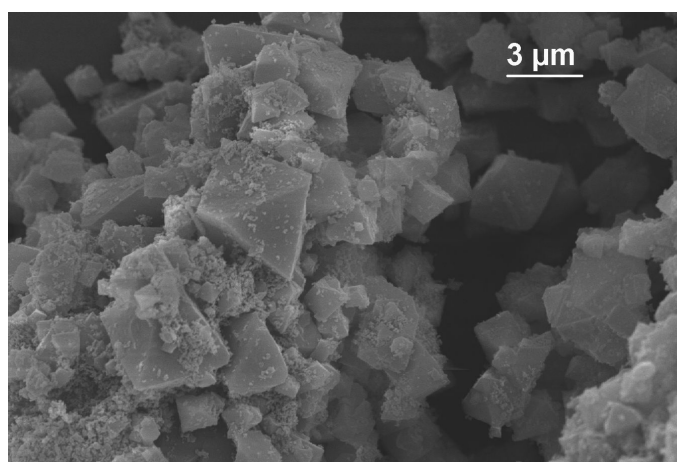


Figure 5.6: SEM picture of $\text{Cu}_3(\text{BTC})_2$ crystals.

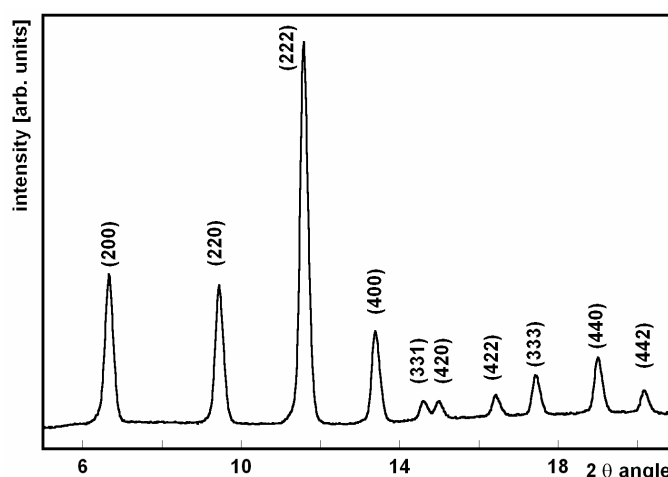


Figure 5.7: Powder X-ray diffraction pattern (Cu $\text{K}\alpha$ -radiation) of $\text{Cu}_3(\text{BTC})$.

The Ni-based metal-organic framework consists of Ni^{2+} ions coordinated by 2,5-dihydroxy-terephthalate giving a three-dimensional honeycomb-like network. At the intersections of the honeycomb are helical chains of cis-edged connected nickel-

oxygen octahedral, where one axial position is occupied by a water molecule. The chains are connected by the organic ligand with three adjacent chains in the honeycomb-like pore structure. The channels of this structure have a diameter of approximately 11 Å.^[95]

The Ni-MOF was prepared through hydrothermal synthesis by Dietzel et al.^[95] and activated by heating in vacuum for several hours at 100 °C. Fig. 5.8 shows the crystal structure with the uniform channels of the Nickel based MOF, obtained from the X-ray diffraction pattern reported in the work of Dietzel et al.^[95]

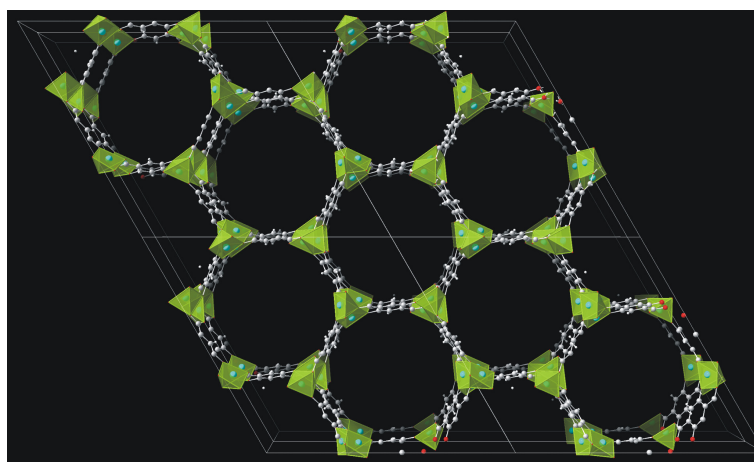


Fig. 5.8 Crystal structure of the Ni-MOF, obtained from the X-Ray diffraction data reported in reference^[95] (Ni, green; O, red; C, grey; H white). The Nickel-oxygen polyhedra are shown in green. Here the axial position occupied by the H₂O ligand is missing.

The Al-based MOF, provided by BASF, is a novel structure, which is still not completely investigated. Fig. 5.9 shows a similar structure to that of the Al-MOF sample with linear rows of aluminium-oxygen polyhedra connected with other four rows by the organic ligand. This metal-organic framework possesses one-dimensional channels. Due to the flexibility of the framework these channels can be compressed to a certain extent, providing a rather broad distribution of pore dimensions. The SEM picture of Al-MOF exhibits row-like crystallites which form two-dimensional casually oriented platelets (fig.5.10).

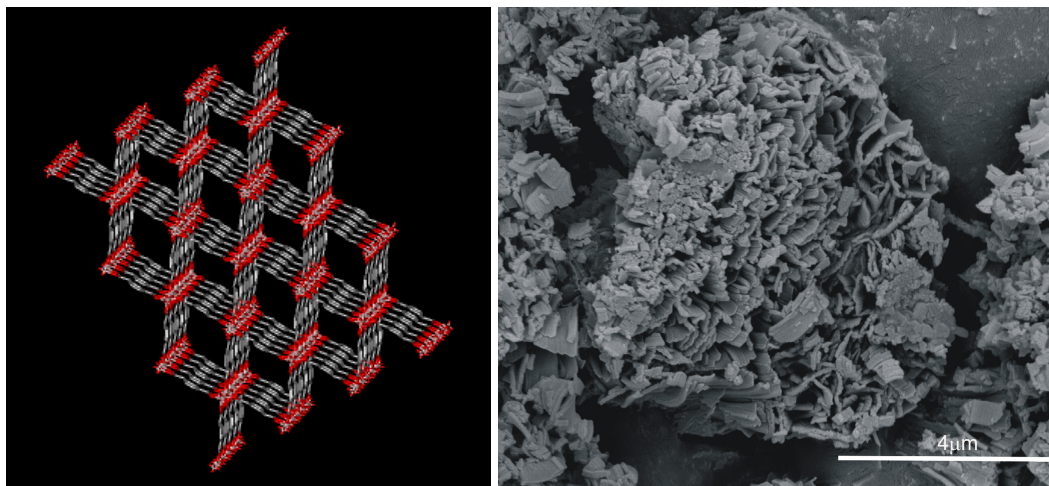


Fig. 5.9 (right): one dimensional channels, in the flexible framework of the in Al-MOF-like structure³.

Fig 5.10 (left): Micrograph picture of Al-MOF.

MR 3677 is a Cu-based metal-organic framework provided by BASF, synthesized by the same electrochemical procedure as Cu-BTC, and whose structure cannot be reported because of a pending patent. The values of the BET and Langmuir specific surface area are $359 \text{ m}^2 \text{ g}^{-1}$ and $886 \text{ m}^2 \text{ g}^{-1}$, respectively.

The multipoint BET and the Langmuir specific surface area of these samples were measured with an automatic gas sorption system using nitrogen gas at 77 K and at relative pressures of $0.05 < P/P_0 < 1$. Previous to these measurements the samples were degassed in vacuum and at 373 K overnight. Table 5-1 shows the surface properties of the investigated MOFs. The difference between the values of the SSA obtained with the BET and the Langmuir model for each structure is due to the fact that both models cannot adequately describe the N_2 adsorption isotherms of a microporous material, even though reproducing mathematically the shape of the isotherm. Nevertheless, these methods are commonly applied to characterize the SSA of microporous samples and can be used to compare similar porous materials. As an example the N_2 adsorption isotherm of MOF-5 described by a linear Langmuir equation over the whole P/P_0 range and by a BET-equation at low relative pressures are shown in fig B-9 and B-10, respectively.

³ Picture provided by U. Müller (BASF)

Table 5-1: Specific surface area of metal-organic frameworks determined by nitrogen adsorption at 77 K using the BET and the Langmuir model.

Sample	Central metal-ion	BET SSA m ² g ⁻¹	Langmuir SSA m ² g ⁻¹
MOF-5 high quality ^[85]	Zn ²⁺	2296	3840
MOF-5 lab. synthesis ^[86]	Zn ²⁺	572	1014
Cu-BTC ^[85]	Cu ²⁺	1154	1958
MR 3677	Cu ²⁺	359	886
Al-MOF	Al ³⁺	933	1779
IRMOF-8	Zn ²⁺	1215	1922
Ni-MOF ^[95]	Ni ²⁺	482	951

5.1 Volumetric measurements

5.1.1 Results

Hydrogen storage measurements were performed at different temperatures using a Sieverts' apparatus. Previous to the measurements the samples were activated in vacuum at temperatures of 373 to 473 K, depending on the thermal stability of the MOF-compound. Through this activation procedure, still occluded solvent molecules and adsorbed moisture were removed. The hydrogen adsorption isotherms were measured at pressures between ~ 1 bar and 75 bar at different temperatures. Each point of the isotherm was measured independently from the previous adsorption step after degassing in vacuum at higher temperatures.

Figures 5.11 and 5.12 show the adsorption isotherms of MOF-5 and Cu-BTC at 298 K, 200 K, 87 K and 77 K. At low temperatures the isotherms show a type I profile with an initial steep increase in the hydrogen uptake followed by a plateau at high pressures. For dilute surface coverage at room temperature (RT) the isotherm is more properly described through a linear Henry-type profile. Such types of isotherms are typical for physical adsorption of H₂ in microporous materials and are also obtained for hydrogen adsorption in carbon materials (see section 4.2). No change in the shape of the isotherm is observed after several numbers of adsorption-desorption cycles, indicating clearly the full reversibility of the adsorption process and the framework stability upon adsorption. Similar isotherms are measured at 77 K and RT for the other metal-organic frameworks (fig. B-4, B-5, B-6, B-7, B-8).

Using the Langmuir equation^[60] to describe the isotherms at 77 K it is possible to obtain the saturation or plateau value of the hydrogen storage (m_{sat}), which corresponds to the maximum of the hydrogen storage capacity. The adsorption properties of the investigated MOFs are reported in table 5-2.

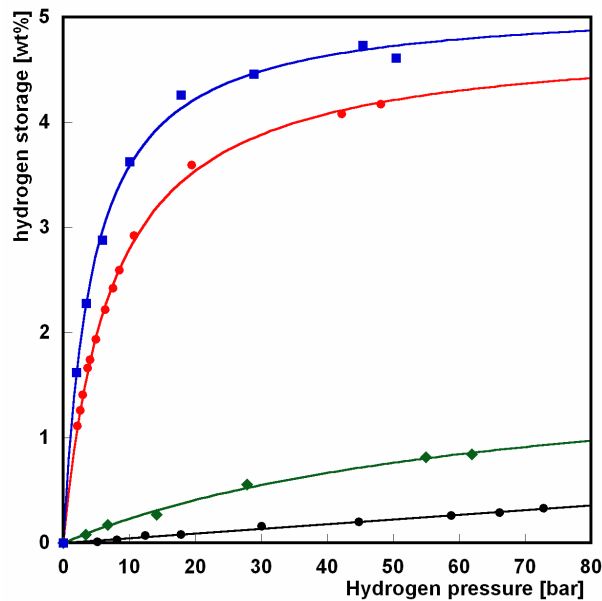


Fig. 5.11: Adsorption isotherms of MOF-5 at 77 K (blue), 87 K (red), 200 K (green) described with a Langmuir equation and 298 K (black) described with a linear equation.

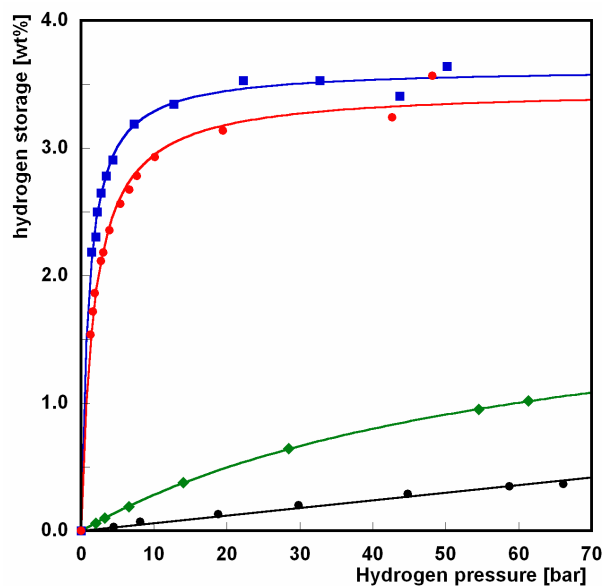


Fig 5.12 : Adsorption isotherms of $\text{Cu}_3(\text{BTC})_2$ at 77 K (blue), 87 K (red), 200 K (green) described with a Langmuir equation and 298 K (black) described with a linear equation.

With an uptake of 4.7 wt% at 50 bar and 77 K and a saturation value of 5.1 wt% MOF-5 exhibits the highest hydrogen storage capacity of all investigated crystalline microporous materials. Considering that the calculated crystal density of MOF-5 is 0.61 g cm^{-3} [32] the maximum volumetric hydrogen uptake corresponds to a value of 33 g l^{-1} .

Table 5-2: Adsorption properties of the metal-organic frameworks.

Sample	m_{sat} [wt%] at 77 K	H ₂ uptake [wt%] at RT and 65 bar	H ₂ uptake [wt%] at 200 K and 60 bar	Isotherm fig.
MOF-5 high quality ^[85]	5.1 ± 0.3	0.3 ± 0.1	0.9 ± 0.1	Fig. 5.11
MOF-5 lab. synth. ^[86]	1.6 ± 0.2	0.18 ± 0.07	1.0 ± 0.2	Fig. B-4
Cu-BTC ^[85]	3.6 ± 0.2	0.35 ± 0.1	n.d	Fig. 5.12
MR 3677	1.6 ± 0.3	0.1 ± 0.1	n.d	Fig. B-8
Al-MOF	2.9 ± 0.1	0.30 ± 0.05	n.d	Fig. B-6
IRMOF-8	3.5 ± 0.2	0.25 ± 0.07	n.d	Fig. B-7
Ni-MOF ^[95]	1.8 ± 0.1	0.24 ± 0,05	n.d	Fig. B-5

For the MOF-5 sample prepared by the laboratory small scale synthesis a maximum uptake of 1.6 wt% at 77 K was obtained. As mentioned previously, this sample had about a three to four times smaller SSA than the high quality MOF-5 crystals due to the different synthetic procedure. Therefore, the smaller hydrogen uptake value can be attributed to the lower specific surface area.

Cu₃(BTC)₂ exhibits at 77 K an uptake of 3.6 wt%, which is smaller than for high quality MOF-5. However compared to MOF-5 saturation is reached at much lower pressures. For the Cu-MOF sample 90 % of the saturation value at 77 K is obtained at a pressure of approximately 9 bar, whereas, MOF-5 needs a pressure of 40 bar to reach 90% saturation. In addition Cu-BTC possesses a higher crystal density (0.96 g cm⁻³)^[91], so that a maximum volumetric uptake of 36 g l⁻¹ is obtained.

At room temperature all samples show storage capacities less than 0.4 wt% but it is possible to triple the uptake by lowering the temperature to about 200 K.

For all metal-organic frameworks the maximum hydrogen storage capacity (m_{sat} , table 5-2) is plotted versus the BET specific surface area (table 5-1) in figure 5.13. An almost linear correlation is found independent of the framework type and of the building units of the network, like metal-centre or organic ligand. In order to show that this result is independent of the model used to determine the specific surface area of MOFs the maximum hydrogen uptake is also correlated to the Langmuir SSA in fig. B-11.

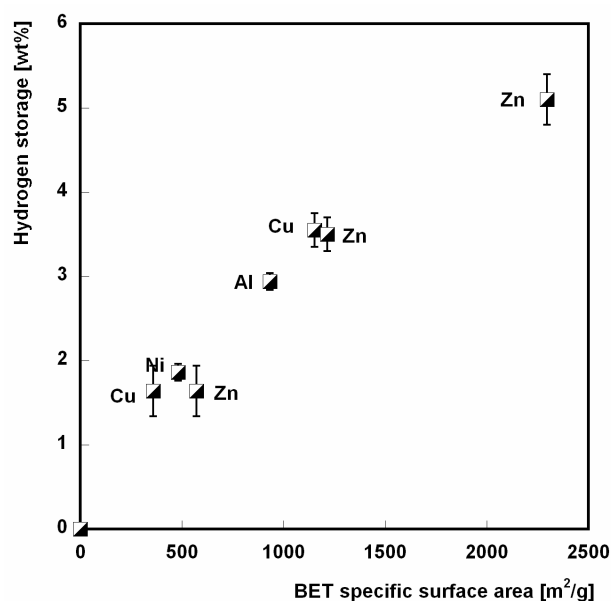


Fig. 5.13: Saturation value of the hydrogen storage capacity correlated to the apparent BET specific surface area. Corresponding metal centres are indicated.

5.2.2 Discussion

The highest maximum storage capacity of 5.1 wt% at 77 K is found for MOF-5, which possesses the largest SSA of all investigated MOFs. This uptake value is comparable with high grade activated carbon with a SSA of higher than 2500 m² g⁻¹ (sect. 4.1). Later similar values have been independently confirmed by Dailly et al. on high surface area MOF-5.^[90] Only recently higher hydrogen uptakes of 6.9 wt% and 6.2 wt%⁴ were measured for metal-organic frameworks possessing BET specific surface areas of 4746 m² g⁻¹ and 4024 m² g⁻¹, respectively^[34]. At room temperature a storage capacity of less than 0.4 wt% was measured for MOF-5, which is in good agreement with Monte Carlo simulations which yield an uptake of approximately 0.4 wt% at 65 bar.

Nevertheless, comparing different MOFs, reveals that the saturation is reached at different pressures. Fig. 5.14 shows the adsorption isotherms for MOF-5 and Cu-BTC. At pressures below 6 bar the hydrogen uptake is higher for Cu-BTC, then a

⁴ The authors report 7.5 wt% and 6.7 wt%, however defining it as percent mass of hydrogen per mass of sample, different from eq. 2.15

crossover in the adsorption isotherms of the two MOFs is observed and at higher pressures MOF-5 exhibits a larger storage capacity.

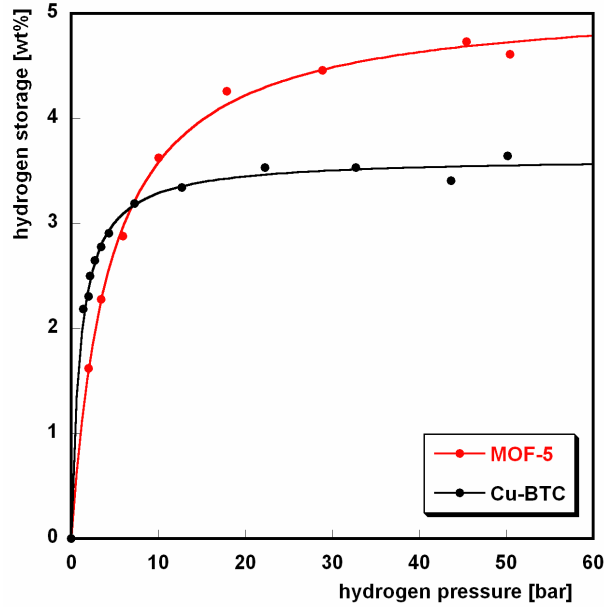


Fig. 5.14: Comparison between the adsorption isotherms of MOF-5 (red) and Cu-BTC (black) at 77 K.

This difference indicates a higher interaction energy between hydrogen and the adsorbent in the case of Cu-BTC. Therefore, the isosteric enthalpy of adsorption was calculated using the Clausius-Clapeyron equation (5.1) for the isotherms measured at 77 K and 87 K and neglecting any dependence of the adsorption enthalpy on the coverage.

$$\Delta h_{\text{ads}} = -\frac{R \cdot T_1 \cdot T_2}{T_2 - T_1} \cdot \ln \left(\frac{p_2}{p_1} \right)_\theta = -\frac{R \cdot T_1 \cdot T_2}{T_2 - T_1} \cdot \ln \frac{a_1}{a_2} \quad (5.1)$$

Here T_1 and T_2 are 77 K and 87 K, p_1 and p_2 are the hydrogen pressures corresponding to an equal fractional coverage θ , and a_1 and a_2 are the constants derived from the linearized Langmuir equation (5.2) at T_1 and T_2 , respectively (fig 5).

$$\left(\frac{p}{\theta} \right)_T = \frac{1}{a_T} + p, \quad (5.2)$$

where p is the equilibrium hydrogen pressure at a certain temperature T .

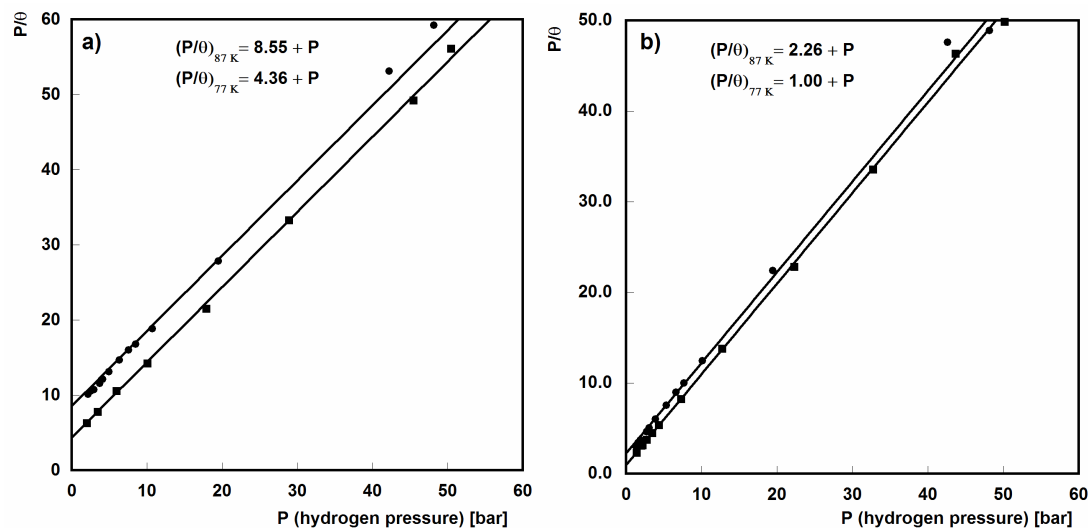


Fig. 5.15: Linearized Langmuir equation for a) MOF-5, and b) Cu-BTC at 77 K (squares) and 87 K (dots). The intercept with the vertical axis corresponds to the constant $1/a$ used to estimate the heat of adsorption.

For MOF-5 and Cu-BTC an enthalpy of adsorption of -3.8 kJ mol^{-1} and -4.5 kJ mol^{-1} , respectively is obtained. The Langmuir equation (5.2) is derived under the assumption that the adsorption enthalpy is independent from the surface coverage. Especially at low coverage this could lead to an underestimation of the adsorption enthalpy, nevertheless, these low values are characteristic for physical adsorption of hydrogen in metal-organic frameworks. Owing to the fact that each point of the isotherm is individually measured, in the data occurs at high pressures. This leads to a slight uncertainty for the saturation value resulting in a possible error of about $\pm 0.8 \text{ kJ mol}^{-1}$ for the absolute value of the heat of adsorption. However, the error in the difference between the two enthalpy values is considerably smaller. Furthermore, these results are in good agreement with the measurements of Dailly et al.^[90], who reported an enthalpy of adsorption of -4.1 kJ mol^{-1} for MOF-5 and with theoretical calculations which yield a value of -4.0 to -4.2 kJ mol^{-1} ^[16]. Recently low pressure isotherms ($< 1 \text{ bar}$) were reported for Cu-BTC at 77 K and 87 K, which yield an isothermic heat of adsorption of -6.1 kJ mol^{-1} .^[96] This higher value may be due to the different pressure range which was used to determine the enthalpy.

Simultaneously with the present work, a new Cu-based MOF has been developed and studied for hydrogen storage by the group of Yaghi.^[97] These authors assume that

high affinity of hydrogen molecules with Cu-MOF is due to the presence of open metal sites which are activated when water ligands are removed from the copper centre. Open metal sites are in fact coordinatively unsaturated central metal ions, which could induce a stronger polarization of the hydrogen molecule compared to metal centres with fully occupied coordination positions. While MOF-5 does not possess these highly active open metal sites, Cu-BTC does. Another possible explanation for the different heat of adsorption between the two samples could be attributed to different pore sizes. Indeed, small micropores produce an increased adsorbate-adsorbent interaction potential. Also from theoretical calculations on carbon structures it is well known that hydrogen adsorption is favoured in pores with a small diameter.^[15] Under the assumption that this dependence is also valid for metal-organic frameworks it would be reasonable that hydrogen is more strongly adsorbed in Cu-BTC, which has two types of pores: the main pores of 9 Å in diameter and smaller pores with windows of 3.5 Å.^[92] MOF-5 possesses bigger pores of 12 Å in diameter.^[84] Possibly both properties, open metal sites and pore size can influence the adsorption behaviour of MOFs.

As for carbon materials also for MOFs a linear correlation between the maximum hydrogen storage capacity at 77 K and the BET specific surface area is found.

Similar results were obtained for methane storage in metal-organic frameworks.^[36] In previous works^[87] no such correlation was found for hydrogen storage in MOFs, at 77 K and a pressure of 1 bar, since under these conditions no saturation is reached. As observed for MOF-5, and Cu₃(BTC)₂ the low pressure region of the adsorption isotherm is strongly dependent on the strength of the interaction between hydrogen molecules and the adsorbent. At low pressures the hydrogen uptake depends on both the heat of adsorption and the specific surface area, therefore no simple correlation can be observed. However, at pressures high enough to reach saturation the storage capacity is only dependent on the SSA of the material.

Grand Canonical Monte Carlo simulations performed for different metal-organic frameworks strongly support these experimental findings.^[98] In their calculations the authors find at low coverages a linear correlation between the hydrogen uptake and the isosteric heat of adsorption of different MOFs. In contrast, at higher pressures the

uptake is independent of the adsorption enthalpy and correlates with the SSA. Initially it was unclear if a correlation between the SSA and the hydrogen storage capacity may exist for MOFs^[87] as it was found for carbonaceous materials (sect. 4.2) However, recently the linear correlation found in the present work has been adopted by several groups and has been observed independently in other MOFs.^[34]

5.3 Thermal desorption spectroscopy of hydrogen in MOFs

5.3.1 Results

Figure 5.16 shows the desorption spectrum of hydrogen in Cu-BTC performed with two distinct heating rates of 0.1 K s^{-1} and 0.03 K s^{-1} , respectively. Prior to the measurement the sample was loaded with a hydrogen pressure of 25 mbar and then cooled down to 20 K.

Three distinct desorption peaks are observed for hydrogen in Cu-BTC with maxima at approximately 25 K, 35 K and 50 K. Above 70 K the amount of desorbed hydrogen is almost negligible. Nevertheless the spectra were recorded up to temperatures of 370 K. The amount of hydrogen desorbed from Cu-BTC corresponds to $4.5 \pm 0.3 \text{ wt}\%$.

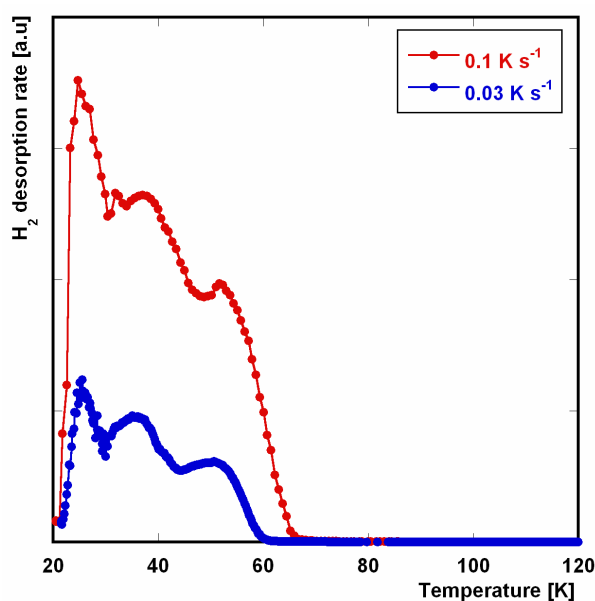


Fig. 5.16: Thermal desorption spectra of hydrogen desorbed from Cu-BTC. The red and the blue spectra were obtained with a heating rate of 0.1 K s^{-1} and 0.03 K s^{-1} , respectively.

Thermal desorption spectra of Al-MOF (fig. 5.17), of IRMOF-8, (fig. 5.18), and of the Cu-based metal-organic framework, MR 3677, (fig. 5.19) were measured under the same experimental conditions as for Cu-BTC.

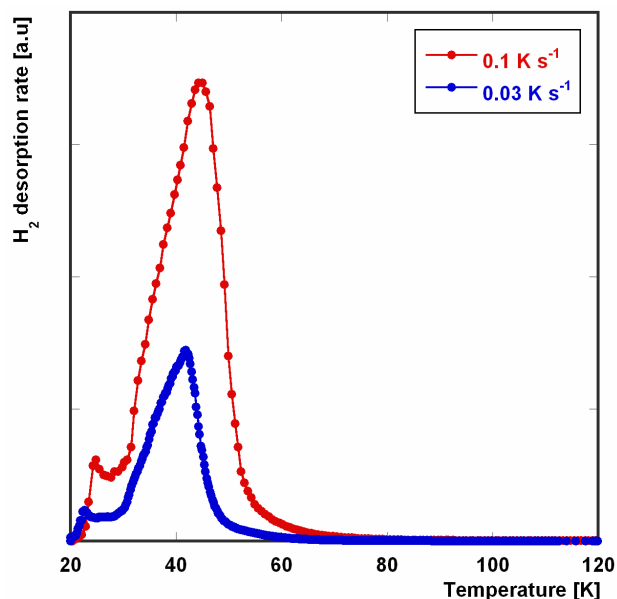


Fig. 5.17 (left): TDS spectra of hydrogen in Al-MOF with heating rates of 0.1 K s^{-1} (red) and 0.03 K s^{-1} (blue).

In the desorption spectrum of hydrogen on the Al-based metal-organic framework a main broad desorption peak with a maximum around 45 K and additionally a very small peak at approximately 25 K are observed. The desorbed hydrogen corresponds to an amount of $2.9 \pm 0.3 \text{ wt}\%$.

Figure 5.18 shows the desorption spectrum of hydrogen in IRMOF-8 recorded with the two heating rates. The TDS spectrum of IRMOF-8 exhibits several desorption maxima: a very sharp peak at 25 K, a larger peak at 35 K with a shoulder at temperatures of approximately 40 K, a small maximum at 60 K, and a very small peak at 83 K accounting for less than 0.02 wt% of hydrogen. In total the area under the desorption curve corresponds to $2.9 \pm 0.4 \text{ wt}\%$ hydrogen.

The desorption curve of the Cu-based metal-organic framework, MR 3677, is recorded with heating rates of 0.1 K s^{-1} and 0.03 K s^{-1} (fig. 5.19). The curve presents two desorption maxima at 27 K and 45 K, respectively, and a shoulder at a temperature around 57 K. A total amount of $1.2 \pm 0.2 \text{ wt}\%$ of hydrogen is desorbed from the surface of MR 3677.

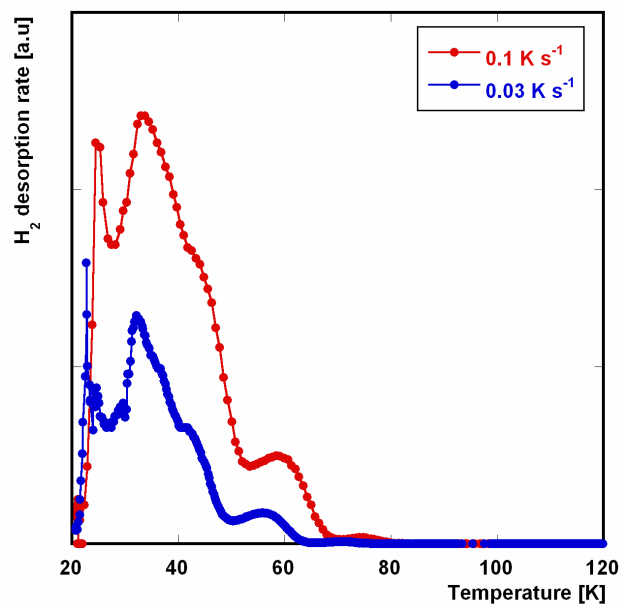


Fig. 5.18: TDS spectrum of hydrogen in IRMOF-8 obtained with a heating rate of 0.1 K s^{-1} (red) and 0.03 K s^{-1} (blue).

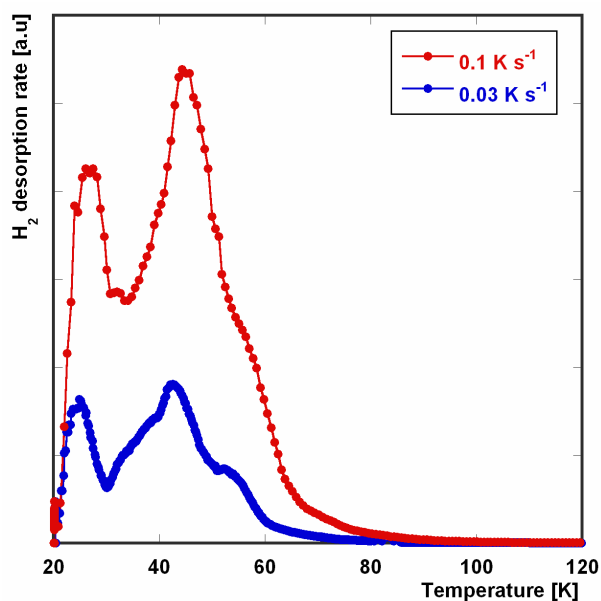


Fig. 5.19 (left): TDS spectra of hydrogen adsorbed on MR 3677 recorded with a heating rate of 0.1 K s^{-1} (red) and 0.03 K s^{-1} (blue).

5.3.2 Discussion

For all the investigated metal-organic frameworks desorption of hydrogen takes place at temperatures between 20 K and 80 K. At higher temperatures the amount of hydrogen desorbed is negligible ($< 0.02 \text{ wt}\%$). The low temperatures of desorption

indicate a reversible character of the adsorption process in metal-organic frameworks, which is typical for physisorption. This observation is in good agreement with the gravimetric measurements performed by Rowsell et al. on MOF-5 which show that at 77 K and under vacuum all hydrogen could be reversibly removed from the surface.^[87]

For all samples the desorption spectrum measured with a small heating rate is shifted towards lower temperatures. This shift of the desorption maxima indicates that the hydrogen release is thermally activated. For both heating rates the time-dependent area under the desorption curve is almost equal and corresponds to the same amount of desorbed hydrogen (eq. 3.5). In addition, the ratio between the temperature-dependent area measured with rates of 0.1 K s^{-1} and 0.03 K s^{-1} corresponds to the ratio between the heating rates.

All desorption spectra exhibit a hydrogen desorption peak at approximately 25 K independent of the adsorbent material. Owing to the low temperature of desorption, which is close to the evaporation temperature of hydrogen, this desorption peak is assigned to liquid hydrogen or H_2 weakly adsorbed on top of the monolayer. In order to calculate the amount of hydrogen which is desorbed from the surface of the metal-organic framework the contribution of the desorption peak at 25 K was subtracted from the total desorption area. The obtained values can be compared with the maximum amount of hydrogen adsorbed at 77 K and high pressure which corresponds to the saturation uptake of hydrogen. In table 5-3 these two quantities are compared for MOFs and for the carbon materials investigated in sect. 4.3. The errors reported in the last column of table 5-3 correspond to the standard deviation of a series of measurements. However an additional uncertainty of $\sim 10\%$ should be considered for the values measured from the area of the desorption spectrum, due to the assumptions made for calibration and for the determination of the amount of liquid hydrogen.

Nevertheless, a fairly good agreement of the two values is obtained for almost all investigated samples. Only for the metal-organic framework sample MR 3677 and IRMOF-8 a larger deviation is found. For MR3677 the hydrogen desorption spectrum exhibits a very broad peak at 25 K, which has been excluded for the determination of the amount of hydrogen desorbed. However, it is not clear if the

entire quantity of hydrogen desorbed at this temperature is simply liquid H₂ or if some amount is also adsorbed directly on the framework.

The comparable values obtained from thermal desorption spectroscopy and from the high pressure adsorption isotherms demonstrate that under different physical conditions complete monolayer coverage is obtained, i.e. 25 mbar at 20 K and high pressures and 77 K. This gives confidence that all adsorption sites are occupied by hydrogen molecules when the temperature program for desorption in vacuum is started.

Table 5-3: Maximum hydrogen uptake of MOFs and carbon materials measured from the adsorption isotherms at 77 K and high pressures compared to the total amount of hydrogen desorbed, measured from the thermal desorption spectra.

Adsorbent	Maximum uptake at 77K (isotherm) [wt%]	Amount desorbed in vacuum (TDS) [wt%]
Al-MOF	2.9 ± 0.1	2.8 ± 0.2
Cu-BTC	3.6 ± 0.2	3.3 ± 0.2
MR 3677	1.6 ± 0.3	0.9 ± 0.2
IRMOF-8	3.5 ± 0.2	2.9 ± 0.4
SWCNTs	2.4 ± 0.3	2.6±0.1
Activated carbon	2.7 ± 0.3	2.5±0.3

The hydrogen desorption curve of Cu-BTC shows additionally to the peak at 25 K two distinct peaks (fig. 5.16). The presence of two desorption maxima is a strong evidence for the existence of at least two distinct adsorption sites for hydrogen, possessing different energies. As shown in the previous section Cu-BTC possesses two different pores: larger channels of 9 Å in diameter and smaller side pockets of approximately 5 Å in diameter. Grand Canonical Monte Carlo simulations for argon adsorption in Cu-BTC, combined with experimental adsorption isotherms suggest that these two pore types are distinct adsorption places for argon.^[92] From static energy optimization the authors obtain that the small side pockets are, with an adsorption enthalpy of $-14.5 \text{ kJ mol}^{-1}$, preferential adsorption sites for argon, compared to the main channels which possess an adsorption enthalpy of only -2.4 kJ mol^{-1} .

Similar assumption can be made for hydrogen adsorbed in Cu-BTC. Indeed hydrogen molecules, like argon atoms, are small enough to access the side pockets through the triangular windows of 3.5 Å in diameter. According to the studies of Ar

adsorption, we can assume that the hydrogen desorption peak at higher temperatures, which is related to higher adsorption energies, corresponds to the hydrogen adsorbed in the small tetrahedral pockets. In contrast, the desorption maximum at 35 K is assigned to hydrogen weakly adsorbed at the surface of the main pores. Owing to the smaller polarizability of the hydrogen molecule compared to Ar atoms, different adsorption enthalpies are expected for H₂ compared to Ar in the sites of Cu-BTC.

As mentioned in section 4.3 the absolute values of the adsorption enthalpies measured from TDS seem to be overestimated. Nevertheless considering eq. (3.7) it is possible to give a rough estimation of the relative ratio of the desorption energies for the two distinct sites from the corresponding temperatures of desorption. A ratio of 1.4 between the desorption temperatures of the two maxima indicates that hydrogen is adsorbed in the tetrahedral side pockets with an enthalpy which is approximately 1.4 times greater than in the larger pores. These main pores can accommodate ca. 2 wt% of hydrogen, while an amount of 1.3 wt% can fit in the side pockets. These values correspond to 6.0 molecules of hydrogen per formula unit or to 97 molecules per unit cell, in the larger pores and 4 H₂ molecules per formula unit or 63 molecules per unit cell in the smaller pores. Here the dehydrated form of Cu-BTC is considered, i.e. 9675 g per unit cell and 605 g per mol of formula unit.

Similarly, IR-spectra of hydrogen adsorbed on Cu-BTC reported by Prepistino et al. exhibit two groups of bands corresponding to hydrogen adsorbed in different sites. The authors assign these two bands to adsorption of H₂ molecules in unspecific interaction sites and to hydrogen coordinated to the copper centres, respectively, rather than to adsorption in pores with different sizes.^[99] Their result is in principle compatible with the findings here presented if it is considered that in the smaller pores the hydrogen molecules are more strongly influenced by the polarizing effect of the Cu(II) centres than in the larger pores.

The desorption spectrum of hydrogen on Al-MOF exhibits additionally to the peak at 25 K only one broad desorption maximum at 45 K (fig. 5.17). In the previous section the structure of Al-MOF has been described. Al-MOF possesses uniform one-dimensional channels, however due to the very flexible structure, these can be compressed to a certain extent. This leads to a broad distribution of pores with

different diameters. Considering that different pore sizes correspond to different potential depth for hydrogen adsorption this would correspond to a broad distribution of desorption temperatures in the TDS curve. Therefore, the hydrogen desorption spectrum of Al-MOF reflects the distribution of pore sizes in the crystalline structure, in a similar way as obtained for disordered activated carbon.

Hydrogen adsorbed on IRMOF-8 exhibits a very complex desorption spectrum (fig. 5.18). At least four adsorption sites for H₂ corresponding to different desorption temperatures can be identified in this framework. It is difficult to correlate the available adsorption sites for hydrogen with the framework structure of IRMOF-8, as it is still not completely understood if catenation takes place for this framework. The large number of adsorption sites could be related to the fact that in IRMOF-8 interweaving can occur during the synthesis, i.e. the minimal displacement of two catenated frameworks, providing a rather complex but well defined framework structure. The effect of interweaving on the pore structure of MOFs has been investigated by J. Rowsell and O. Yaghi.^[100] They showed that an interwoven MOF possessing the same framework structure as IRMOF-8 exhibit two larger pores with slightly different pore dimensions and 6 smaller cavities defined by the four Zn₄OL₃ units, where L stands for the ligand.^[100] For a non catenated framework possessing the same building units only two larger pores exist, corresponding to two different orientation of the ligand in the framework. The complex desorption spectrum of hydrogen adsorbed on IRMOF-8, which exhibits at least 4 different adsorption sites, may indicate an interwoven framework structure. The two small desorption maxima at higher temperature could be associated with the smaller cavities which produce a deeper adsorption potential, while the broad peak and the shoulder at 35 and 40 K, respectively, are attributed to adsorption in the larger pores. Furthermore, it may be as well possible that both frameworks, i.e. a non-catenated and an interwoven are present in the sample which would lead to a smaller fraction of small pores. Fig. 5.20 shows the pore structure proposed by Rowsell and Yaghi for an interwoven cubic framework.^[100]

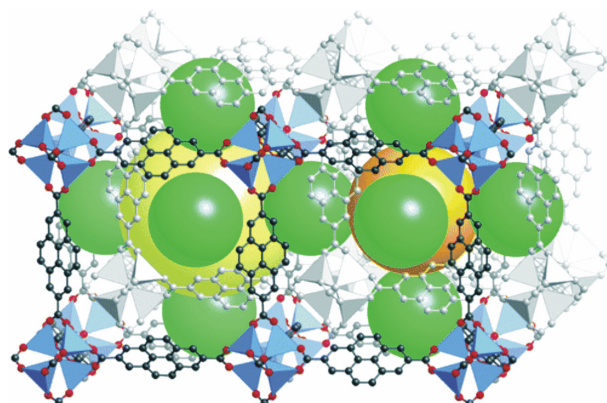


Fig. 5.20: Pore structure of an interwoven framework proposed by Rowsell and Yaghi, reproduced from reference [100]. The grey and the coloured framework are catenated one in the other. The green balls represent the smaller cavities and the yellow balls, the larger pores with slightly different dimensions due to different orientation of the framework.

A comparison of the hydrogen desorption behaviour for all investigated metal-organic frameworks is shown in fig. 5.21. The decrease of the surface coverage, θ , is reported versus the desorption temperature. At low temperature the coverage is higher than 1 as some amount of liquid hydrogen or hydrogen adsorbed on top of the monolayer is present.

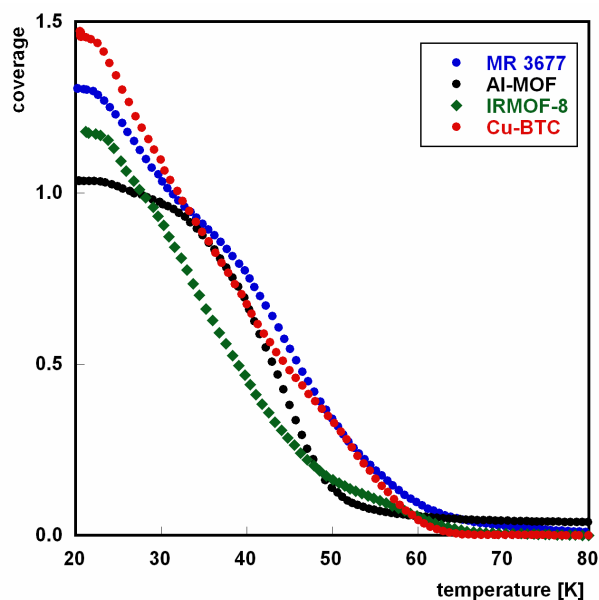


Fig. 5.21: Hydrogen surface coverage versus the desorption temperature for MR 3677 (blue), Al-MOF (black), IRMOF-8 (green) and Cu-BTC (black).

The desorption temperature gives a qualitative measure of the interaction strength between adsorbate and adsorbent. For mobile applications materials which possess strong interaction with H₂ molecules are desirable. The two Cu-based metal-organic frameworks show a very similar desorption behaviour. The hydrogen is released at higher temperature, making Cu-based MOFs interesting candidates for hydrogen physisorption. Of all these materials IRMOF-8 shows the less desirable desorption behaviour, as most of the adsorbed H₂ is released under vacuum at very low temperatures, indicating a weak adsorption potential for this metal-organic framework.

To the best of my knowledge this is the first report on quantitative thermal desorption spectroscopy of hydrogen in metal-organic frameworks. Moreover the measurements have been extended down to 20 K which allows for the first time to identify different adsorption sites in MOFs with this technique. In addition a correlation between the pore-structure of MOFs and the potential adsorption sites has been proposed.

5.3 Raman spectroscopy of adsorbed hydrogen in Cu-BTC

5.3.1 Results

Hydrogen adsorption in Cu-BTC was investigated by inelastic light scattering both at room temperature and at 40 K.

Previous to the measurements in the high pressure Raman cell, a spectrum of Cu-BTC was recorded over a range of Raman shifts from 100 to 1400 cm^{-1} with a commercial Raman Microscope spectrometer using an excitation radiation of 632.82 nm (He-Ne laser) and with a laser power of 4 mW. In order to prevent hydration of the sample, which could influence the spectrum of the framework, Cu-BTC had been previously introduced under argon atmosphere into a sealed quartz tube. Fig 5.22 shows the Raman spectrum of dehydrated Cu-BTC in the range of 100 to 1050 cm^{-1} . Several distinct peaks are observed at 230 (I), 463 (II), 515 (III), 745 (IV), 827 (V), and 1005 cm^{-1} (VI). The measured spectrum was subsequently used to recognize the sample in the high pressure cell.

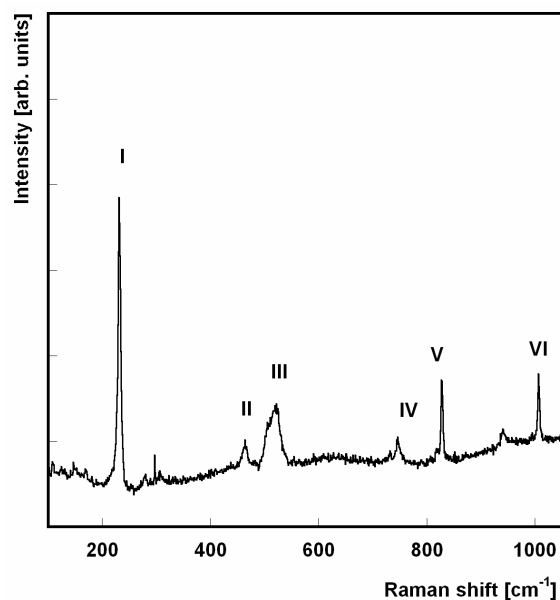


Fig. 5.22: Raman spectrum of dehydrated Cu-BTC recorded under Ar-atmosphere.

The Raman spectra of hydrogen in Cu-BTC were recorded with a small laser power of only 5 mW in order to avoid decomposition of the framework due to local

overheating of the sample. In order to remove adsorbed moisture and the water ligands coordinating the Cu^{2+} ion, Cu-BTC was evacuated in situ for approximately 14 h, prior to the experiment.

The Q-branch of adsorbed hydrogen on Cu-BTC was recorded with an Ar-ion laser emitting at 514 nm. The investigated region of Raman spectra lies in between 4000 and 4350 cm^{-1} and a best resolution of 0.4 cm^{-1} was achieved. Figure 5.23 shows the Q(1) and Q(0)-line of H_2 on Cu-BTC and of free H_2 at 20 bar and 299 K. In both cases the Q(1) and Q(0)-line are observed at 4156 and 4162 cm^{-1} , respectively. The spectrum recorded for hydrogen on the MOF exhibits a higher background which derives from the framework itself.

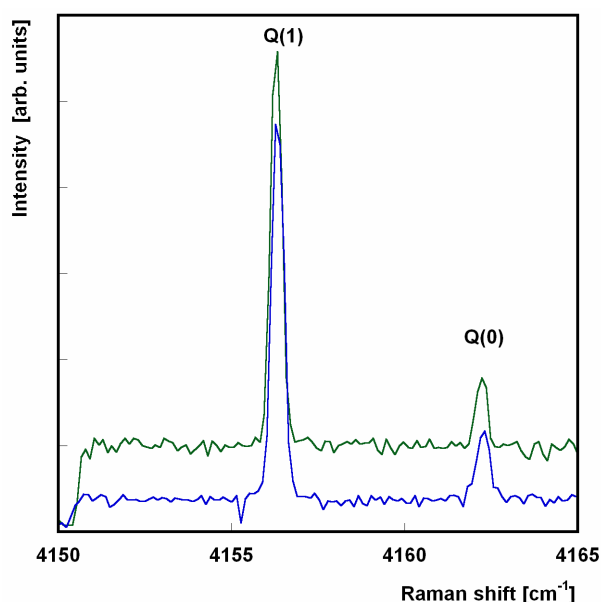


Fig. 5.23: Q(1) and Q(0)-line of free hydrogen (blue line) and of hydrogen on Cu-BTC at 299 K and 20 bar.

At 40 K the Raman spectra of hydrogen adsorbed on Cu-BTC were recorded at pressures ranging from 8 bar to 22 bar. Figure 5.25 shows the Raman spectrum of hydrogen adsorbed on Cu-BTC at 40 K and variable pressure with the Q(1)-line around 4155 cm^{-1} and Q(0)-line around 4162 cm^{-1} .

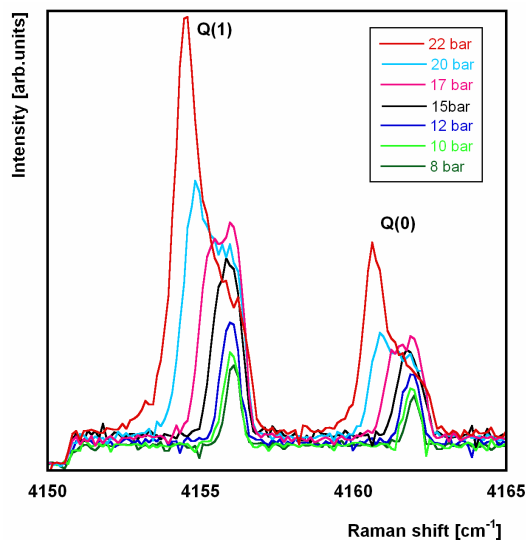


Fig. 5.24: Q(1) and Q(0)-lines of hydrogen adsorbed in Cu-BTC at 40 K and variable pressure.

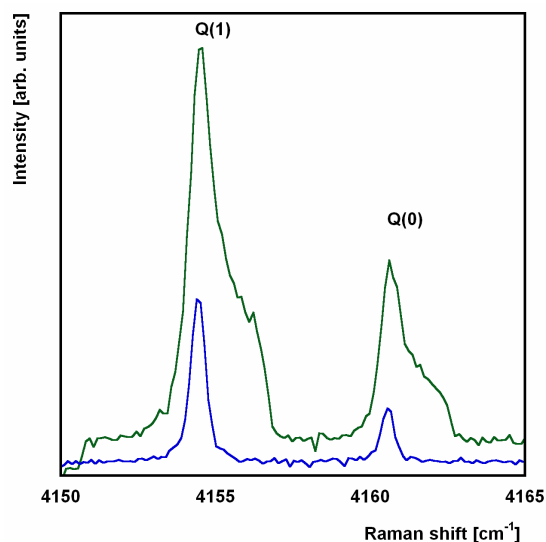


Fig. 5.25: Comparison between the Q-lines of hydrogen in presence of graphite (blue) and hydrogen adsorbed on Cu-BTC (green) at 40 K and 22 bar.

At low hydrogen pressures the spectra exhibit a single peak for each Q-line, occurring at 4156 and 4162 cm^{-1} for $J = 1$ and $J = 0$, respectively. The area of this peak increases with pressure, while the position does not change. At higher pressures for each Q-line a second well defined peak occurs at lower frequencies. In figure 5.24 the symmetric Q-lines of hydrogen on graphite, i.e. non adsorbed hydrogen, are compared to the Raman spectrum of H_2 adsorbed on the metal-organic framework both recorded under the same experimental conditions, i.e. 40 K and 22 bar. The peak

component of hydrogen in Cu-BTC, which arises at lower Raman shifts, matches very well with the Q(1) and Q(0)-line position of H₂ on non-porous graphite, i.e. at 4154.4 and 4160.5 cm⁻¹. These peaks are therefore assigned to free hydrogen gas. In contrast, the peak component at higher energies derives evidently from the adsorbed hydrogen and is visible even at lower pressures.

5.3.2 Discussion

The vibrational properties of the Cu-BTC framework have been recently investigated by Raman spectroscopy by Prestipino et al.^[99] A good agreement is found between the spectrum presented in their work and the one observed in the present study. The authors assigned the bands I, II and III, occurring at Raman shifts between 230 and 515 cm⁻¹ to vibrations associated with the Cu-ions, while the vibrations at higher frequencies are due to the organic part of the framework, i.e. benzene-tricarboxylate. Moreover the three bands at 230, 463 and 515 cm⁻¹ are observed in this position only for the dehydrated form of Cu-BTC indicating that the axial water ligands have been removed in vacuum.

Hydrogen Raman spectra were measured both at 298 K and at low temperatures. At room temperature similar spectra were recorded for free H₂ and for hydrogen molecules in the presence of Cu-BTC. This confirms that the amount of hydrogen adsorbed is negligible and that only free hydrogen gas can be observed by Raman spectroscopy under these conditions. The obtained result is in good agreement with the amount of hydrogen measured from the adsorption isotherms, which yielded an uptake of only 0.13 wt% in Cu-BTC at 20 bar and 298 K. Similar results were obtained from Raman spectra of hydrogen on SWCNTs measured at room temperature (sect. 4.4). In contrast, at 40 K a clear difference between the lines of free and adsorbed hydrogen is observed. The Raman position of the Q-line of adsorbed hydrogen does not change with pressure and is shifted to higher frequencies compared to free H₂. The maximum displacement of the Q-line of adsorbed hydrogen compared to free hydrogen molecules corresponds to a value of only 1.5 cm⁻¹, comparable to hydrogen adsorbed in SWCNTs and activated carbon (sect. 4.4). As for hydrogen in carbon materials, this small value indicates physisorption of

hydrogen in metal-organic frameworks taking place without charge transfer. At high pressures the Q-line of adsorbed hydrogen is shifted towards higher frequencies compared to the gas phase because the density of H₂ adsorbed on the surface of the metal-organic framework is considerably higher than that of free hydrogen gas under the same conditions of temperature and pressure. According to equation 4.11, at high hydrogen densities the quadratic term of the virial expansion prevails and as a result a shift of the Q(J)-line towards higher Raman shift is observed.

The thermal desorption spectrum of Cu-BTC shows the presence of two distinct adsorption sites, while in the Raman spectrum of H₂ only one peak is related to physisorbed hydrogen which could be a convolution of hydrogen in both sites.

Recently, Centrone et al. investigated hydrogen adsorption in MOF-5 by Raman spectroscopy.^[101] Owing to the strong fluorescence produced by the MOF-5 framework in their measurements the Raman spectrum of adsorbed hydrogen is very noisy. The authors observed for hydrogen at room temperature and deuterium at 40 K a strong shift of about 10 cm⁻¹ to lower energies of all the Q-lines of adsorbed H₂ and D₂ compared to the gas phase. They attributed this shift to strong polarising sites in MOF-5. In the present Raman measurements of Cu-BTC and carbon materials a five times smaller shift is observed. Furthermore for Cu-BTC higher adsorption enthalpies have been determined, compared to MOF-5. Further investigations are therefore needed to clarify these discrepancies.

5.5 Summary

Several metal-organic frameworks possessing different structure and composition were investigated for hydrogen storage. Owing to the highest specific surface area MOF-5, a Zn-based MOF, exhibits the highest gravimetric uptake with a saturation value of 5.1 wt% at 77 K. However, at low pressures a higher uptake is observed in Cu-BTC, which possesses smaller pores and so-called open metal-sites, i.e. metal centres with unsaturated coordination positions. This crossover in the adsorption isotherms is attributed to two factors: i) at low hydrogen pressures the hydrogen uptake is influenced by the heat of adsorption, which is higher for hydrogen in Cu-BTC, ii) at higher pressures the storage capacity is influenced by the specific surface area of the adsorbent. In addition, it has been demonstrated, that for all investigated MOFs the saturation value of the hydrogen uptake is correlated with the SSA, and is independent of the type of framework or of the composition. These conclusions are also supported by Grand Canonical Monte Carlo simulations reported in literature.^[98] Moreover Cu-BTC exhibits also the highest volumetric hydrogen uptake of 36 g l⁻¹, so that at moderate pressures this Cu-based MOF is the best candidate for hydrogen storage. At room temperature all metal-organic frameworks possess a storage capacity of less than 0.4 wt%, but the uptake can be tripled by lowering the temperature to 200 K. The measured isosteric heat of adsorption for hydrogen on MOFs corresponds to approximately 4 kJ mol⁻¹, a value which is characteristic for physical adsorption. Moreover it has been shown that the adsorption/desorption process is reversible, indicating that the frameworks are stable upon adsorption of hydrogen.

Thermal desorption spectroscopy has been employed to identify the adsorption sites for hydrogen in the well defined structures of MOFs. The desorption spectra show that at temperatures below 80 K more than 99.98% of the hydrogen is desorbed which is congruent with the low adsorption enthalpies determined from the adsorption isotherms. Furthermore, the total amount of hydrogen adsorbed at 25 mbar and 20 K is equal to the saturation value measured at 77 K and high pressures. For Cu-BTC two distinct adsorption sites, with different activation energies of desorption are identified by TDS. These are assigned to hydrogen adsorption in the

main pores which have a diameter of 11 Å, and to adsorption in the smaller side pockets. In contrast, Al-MOF exhibits a broad distribution of adsorption sites with similar activation energies for desorption. This result is in good agreement with the rather broad distribution of pore sizes in the Al-based framework. IRMOF-8 exhibits a hydrogen desorption spectrum with four maxima which is possibly related to the catenation of the framework. This phenomenon can lead to a complex pore structure. The highest desorption temperatures were measured for the Cu-based metal organic framework, which indicate stronger adsorption sites for hydrogen compared to the other MOFs. Owing to the interesting hydrogen adsorption and desorption properties, Cu-BTC was additionally investigated by Raman spectroscopy. At room temperature and 20 bar the Q-lines of hydrogen on Cu-BTC and of free hydrogen are identical, as the amount of hydrogen adsorbed under these conditions is very small. This result is in good agreement with the low storage capacity measured from the adsorption isotherm at RT (~0.1 wt% at 20 bar). At 40 K higher adsorption densities are achieved and a shift of the Q-line of adsorbed hydrogen compared to free hydrogen towards higher frequencies is measured. This shift corresponds to a value of 1.5 cm⁻¹ which indicates that hydrogen is adsorbed by weak van der Waals interactions and that no charge transfer takes place between adsorbent and adsorbate.

6 Comparison between nanostructured materials with high SSA

For metal-organic frameworks and carbon materials a linear correlation between the hydrogen saturation uptake at 77 K and the BET apparent SSA has been found. In figure 6.1 this correlation is shown both for MOFs and carbon materials.

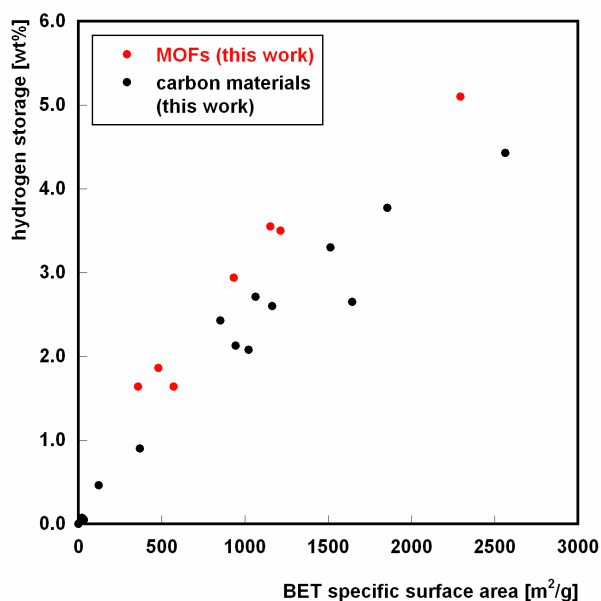


Fig. 6.1 : Maximum hydrogen storage capacity versus BET specific surface area, for MOFs (red dots) and carbon materials (black dots).

The comparison can be extended to the results reported recently by Wong-Foy et al. on MOFs^[34] and to the uptake measurements shown by Texier-Mandoki et al. on porous carbons^[64] (fig. 6.2). Including these results a very broad range of hydrogen uptake values and of apparent specific surface areas is covered both for MOFs and for carbon materials.

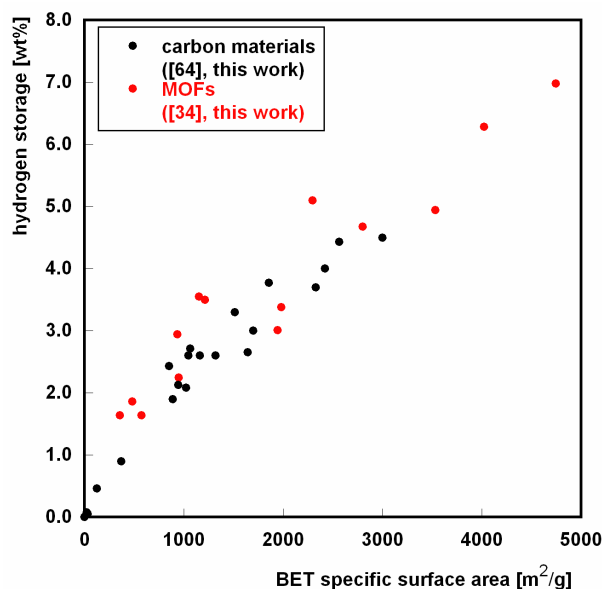


Fig. 6.2: Maximum hydrogen storage capacity versus BET SSA for MOFs reported in chapter 5.2 and by Wong-Foy et al.^[34] (red dots), for carbon nanostructures reported in chapter 4.2 and for porous carbons reported by Texier-Mandoki^[64] (black dots).

In this comparison a third class of porous materials can be included, the zeolites. Zeolites are completely inorganic and possess cations inside their cavities. Langmi et al. have investigated a great number of zeolite types and have found that also for this class of materials the uptake is a linear function of the specific surface area and is rather independent of the zeolite structure^[41,102]. Only for zeolites A and Rho, a slight deviation is found due to the restricted access of nitrogen molecules in the small pores of these structures. For almost all zeolites the saturation is reached at pressures lower than 15 bar. Figure 6.3 shows a general correlation between the saturation value for the hydrogen uptake and the BET specific surface area for MOFs (sect. 5.2 and reference^[34]), carbon nanostructures (sect. 4.2), porous carbon^[64] and zeolites^[41,102]. Storage data of prussian blue analogues, which are porous coordination polymers of the type $M_3[Co(CN)_6]_2$ are finally added.^[103] The scattering of the data may probably be attributed to an uncertainty in the measurements of the apparent specific surface area using the BET model and the comparison of data from different laboratories. Nevertheless, a general linear trend can be recognized for all porous materials. These results show that, independently of texture, structure and

composition, the specific surface area is the only property which determines the maximum uptake of hydrogen in these materials.

Owing to the highest specific surface area, metal-organic frameworks exhibit the highest maximum hydrogen uptake of all porous materials reported in literature.

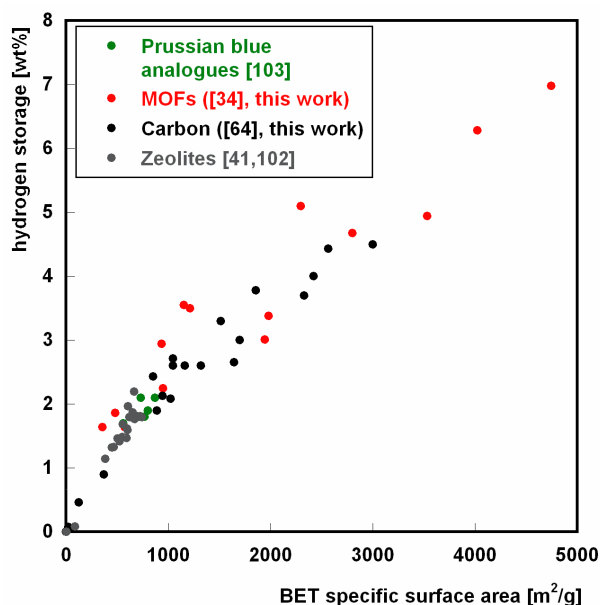


Fig. 6.3: maximum hydrogen uptake versus BET specific surface area for carbon nanostructure (red circles), Zeolites (grey circles), MOFs (black circles) and prussian blue analogues (green circles).

In addition, this general correlation is valid only if the saturation value of the hydrogen uptake will be considered, which can be reached at different pressures for different materials. Indeed, while for zeolites the hydrogen pressure for reaching the maximum uptake is less than 15 bar, for MOFs it has been observed that the hydrogen pressure at which the plateau of the adsorption isotherm is achieved, varies considerably for different frameworks. Therefore, the found correlation cannot be related to the affinity between hydrogen molecules and the adsorbent under unsaturated conditions.

Another quantity which is important for the application of hydrogen storage materials is the volumetric storage capacity, i.e. the amount of hydrogen stored per volume of adsorbent. The carbon nanostructure with the highest gravimetric uptake

of 4.5 wt% is high grade activated carbon, which is similar to AX-21.^[25] Considering that this kind of activated carbon possesses a bulk density of 0.3 g cm^{-3} ^[15] this uptake value corresponds to a volumetric storage capacity of only 14 g l^{-1} . For SWCNTs, which can have bulk densities ranging from $1.3\text{-}1.4 \text{ g cm}^{-3}$ ^[104] a volumetric uptake of approximately 33 g l^{-1} is obtained. The metal-organic frameworks MOF-5 and Cu-BTC show a maximum volumetric hydrogen uptake of 33 g l^{-1} and 36 g l^{-1} respectively, over twice the value for high grade activated carbon. These values have been evaluated from the theoretical crystal density of MOFs and not from the packing density of the material so that some deviation from these values has to be considered for practical applications. The maximum volumetric hydrogen storage capacity reported for zeolites at 77 K and 15 bar by Langmi et al. corresponds to 31 g l^{-1} , for zeolite CaX, which possesses also the highest gravimetric uptake of 2.19 wt%.^[102]

Fig. 6.4 reports the gravimetric hydrogen uptake versus the volumetric storage capacity for some selected metal-organic frameworks (MOF-5, Cu-BTC, Ni-MOF), for high grade activated carbons and SWCNTs and for several zeolite types.^[102] The best materials are those which possess both high gravimetric and volumetric uptake and therefore occupy the upper left corner of the diagram. For MOFs the volumetric hydrogen uptake strongly depends on the framework type, as the crystal density varies considerably for different MOFs. Among all materials MOF-5 and Cu-BTC exhibit both high gravimetric and volumetric uptake values. Zeolites Y and X have volumetric hydrogen storage capacities which range from 21 g l^{-1} to 31 g l^{-1} , but show very low gravimetric storage capacities, due to the low SSA. The investigated carbon materials have the disadvantage of possessing high gravimetric uptakes but low volumetric storage capacity like in high grade activated carbon possessing low bulk density, or the opposite situation like in carbon nanotubes. Both values, i.e. gravimetric and volumetric uptake are here determined as saturation values from the adsorption isotherms. In contrast, the storage capacity at low pressures is influenced by the enthalpy of adsorption, which is strongly material dependent as it has been observed for metal-organic frameworks (sect. 5.2). A different result will be therefore obtained, if the hydrogen uptake at a smaller hydrogen pressures is considered.

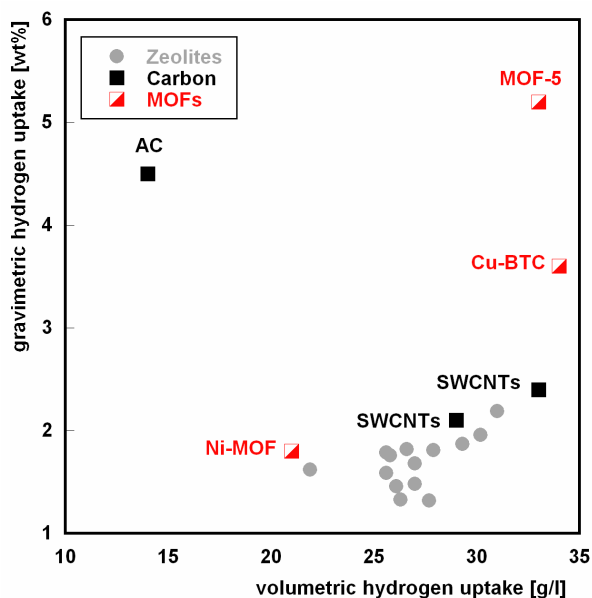


Fig. 6.4 Gravimetric hydrogen storage capacities versus volumetric hydrogen storage capacities for some selected MOFs (Cu-BTC, MOF-5 and NI-MOF, red squares), for high grade activated carbon (AC) and purified SWCNTs (black squares) and zeolites (grey dots)^[102] at 77 K and at pressures corresponding to the saturation.

As an example fig. 6.5 reports the gravimetric and volumetric hydrogen storage capacity of the same materials as in fig. 6.4, however at a pressure of only 4 bar and 77 K. Under these conditions the gravimetric uptake of MOF-5 is smaller than for high grade activated carbon, with comparable specific surface area and Cu-BTC exhibits both higher gravimetric and volumetric uptake than MOF-5. This indicates that far from saturation conditions the gravimetric and volumetric uptake are strongly material dependent and the specific surface area plays a secondary role.

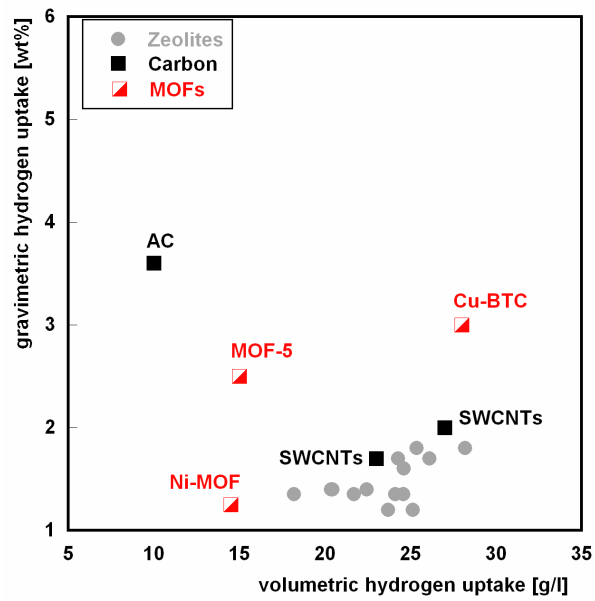


Fig. 6.5 Gravimetric hydrogen storage capacities versus volumetric hydrogen storage capacities for some selected MOFs (Cu-BTC, MOF-5 and Ni-MOF, red squares), for high grade activated carbon and purified SWCNTs (black squares) and zeolites (grey dots)^[102] at 77 K and 4 bar.

7 Conclusions

Hydrogen adsorption on a great variety of carbon materials with ordered and disordered structures and on metal-organic frameworks possessing different central metal-ions and organic ligands, as well as different network topologies, have been investigated.

Three experimental techniques, especially designed for studying low temperature physisorption were used.

Storage capacities and adsorption isotherms were measured with a Sieverts' apparatus up to high pressures and at different temperatures. This technique allowed to investigate the adsorption of hydrogen on porous materials up to the saturation regime, providing information on two important quantities for mobile applications: the maximum uptake value and the hydrogen pressure necessary to reach it. Especially for metal-organic framework this pressure regime was hardly investigated before^[4] and only recently a few reports on saturation of hydrogen in MOFs appeared.^[34,90]

Thermal desorption spectroscopy was used at low pressures and at temperatures down to 20 K providing a spectrum of the adsorption sites for H₂. Additionally, through appropriate calibration this technique was successfully used as a quantitative method.

Finally, the adsorption of hydrogen was studied by means of Raman spectroscopy at room temperature and 40 K. Here the changes in the energy of the vibrational and rotational transitions of adsorbed hydrogen compared to free hydrogen were measured in order to study the effect of the adsorbent on H₂ molecules.

The obtained results are summarized in the following points:

1. Independent of the network topology of MOFs or of the long-range order in carbon materials the maximum hydrogen uptake always correlates linearly with the specific surface area. The comparison between different classes of porous materials, including zeolites, showed that this correlation is material independent under saturation conditions at 77 K.

The correlation obtained on carbon materials confirms the results obtained by Nijkamp et al. in the low pressure regime^[26] and comes close to the values obtained from the theoretical model^[65] where the density of liquid hydrogen on a graphene sheet is considered. A comparison between the theoretical value and the obtained experimental value showed that at 77 K the maximum density of hydrogen adsorbed on carbon materials corresponds to approximately 80% of the density of liquid hydrogen.

For metal-organic framework the correlation between maximum hydrogen uptake and specific surface area was found here for the first time and subsequently adopted and confirmed for different MOFs by other groups.^[34]

2. At room temperature all investigated materials exhibit storage capacities lower than 0.5 wt%. However, high uptake values, up to ~5 wt%, were obtained at 77 K both for carbon nanostructures and metal-organic frameworks. Among these classes of porous materials the best samples are high-grade activated carbon and MOF-5, respectively.
3. Furthermore, the desorption spectra of hydrogen adsorbed on different porous materials show a relation between the hydrogen adsorption sites and the pore-structure both for carbon materials and metal-organic frameworks. Pores with different dimensions correspond to adsorption sites with different energy.

These are the first reports on TDS extended to very low temperatures of about 20 K to investigate the adsorption of hydrogen on porous materials. The desorption spectra show that at about 80 K all hydrogen is already desorbed from carbon materials and metal-organic frameworks under vacuum conditions. Therefore, only if extended to very low temperatures, thermal desorption spectroscopy can be employed to investigate hydrogen physisorption on porous materials. Under these conditions this technique is a powerful method to investigate the presence of different adsorption sites in porous materials. Owing to the calibration with well known metal hydrides it was possible to quantify the amount of hydrogen adsorbed in each site.

4. The results obtained on Raman spectroscopy of hydrogen adsorbed on different porous carbonaceous samples at 40 K confirm the small difference in the Raman shift of adsorbed and free hydrogen observed recently on

activated carbon.^[76] This small shift is characteristic for hydrogen adsorbed through weak van der Waals forces on the surface of all carbonaceous materials without any charge transfer between adsorbate and adsorbent. Additionally, two distinct peak components were observed for hydrogen adsorbed at high pressure and 40 K on SWCNTs, which indicate that H₂ molecules are physisorbed on this sample with two different energies, probably corresponding to two different adsorption sites. In addition, the TM-mode of SWCNTs, which is typically sensitive to charge transfer from or to the adsorbate was investigated. At 40 K and a hydrogen pressure of 20 bar the frequency of this mode was shifted by only 2 cm⁻¹. Both small shifts in the lines of the adsorbate and of the adsorbent confirm the weak interaction energies of the physisorption process.

The investigations on the S-band of adsorbed hydrogen, corresponding to the pure rotation of the molecule, indicate that the H₂ molecules are almost free to rotate on the surface of the SWCNTs.

Small shifts in wavelength of adsorbed compared to free hydrogen were also obtained for H₂ on Cu-BTC, in contrast to previous results obtained on MOF-5.^[101]

The low number of publications on Raman spectroscopy of adsorbed hydrogen indicates that this technique is still not completely recognized as a tool to study hydrogen physisorption on porous materials. However, the present results confirm the possibility to successfully use Raman spectroscopy to investigate adsorbent-adsorbate interactions.

5. A comparison of two well defined metal-organic frameworks showed that MOFs, which possess smaller pores exhibit a higher adsorption enthalpy and higher storage capacities at low pressures, while at higher pressures the specific surface area determines the hydrogen uptake. The correlation between hydrogen uptake and adsorption enthalpy at low pressures and specific surface area at high pressures was recently confirmed by Grand Canonical Monte Carlo simulations on metal-organic frameworks.^[98]

In the present work the physisorption of hydrogen in microporous materials was systematically investigated applying different experimental techniques. The results clearly indicate that a large specific surface area is needed for a high hydrogen storage capacity and that small pores are necessary to increase the interaction energy. This new understanding may help to tailor new materials with optimized hydrogen storage properties.

8. Zusammenfassung

Einleitung und Motivation

Wasserstoff ist der ideale Energieträger, da er völlig schadstofffrei verbrennt und einen potentiell hohen Energiegehalt pro Masse besitzt. Die größte Herausforderung für den Gebrauch von Wasserstoff als Kraftstoff für Fahrzeuge ist die Wasserstoffspeicherung in sicheren und kostengünstigen Systemen. Es existieren zwei kommerzielle Methoden, um H_2 zu speichern: Wasserstoffgas in Druckflaschen aus Stahl oder aus Verbundwerkstoffen und flüssiger Wasserstoff in Tieftemperaturtanks. Beide Methoden haben schwerwiegende Nachteile, wie z.B. das große Volumen, das gasförmiger Wasserstoff bei Raumtemperatur einnimmt oder die tiefen Temperaturen von ca. 20 K, die nötig sind, um H_2 zu verflüssigen.

Eine mögliche Alternative ist die Wasserstoffspeicherung in leichten Festkörpern. Man kann drei unterschiedliche Mechanismen dafür unterscheiden: i) Dissoziation von H_2 Molekülen und Absorption in Metallen, ii) Bildung von Hydriden mit ionischem Charakter und iii) Physisorption von Wasserstoffmolekülen auf der Oberfläche von porösen Materialien.^[1,2]

Im Vergleich zur chemischen Speicherung hat die physikalische Adsorption von H_2 mehrere Vorteile. Durch Physisorption wird Wasserstoff reversibel gespeichert, und da keine Energiebarriere zwischen der Gasphase und dem adsorbierten Zustand besteht, ist eine schnelle Adsorptions- und Desorptionskinetik gewährleistet. Aufgrund der niedrigen Adsorptionswärme, die in der Physisorption von Wasserstoff frei wird, wären keine zusätzlichen Wärmeregulierungssysteme in Kraftfahrzeugen notwendig. Allerdings ist die niedrige Adsorptionsenthalpie auch der Grund dafür, dass durch molekulare Adsorption in porösen Materialien nur bei tiefen Temperaturen von ca. 80 K technologisch relevante Speicherdichten erreicht werden.

Die physikalische Adsorption eines Gases auf einem Festkörper kann als Anreicherung von Molekülen an der Grenzfläche zwischen der Oberfläche des

Festkörpers und der Gasphase beschrieben werden.^[5] Zuständig für dieses Phänomen sind attraktive van der Waals oder Londonsche Dispersionskräfte. Diese Art von Wechselwirkung hat ihren Ursprung in der Anziehung zwischen fluktuierenden und induzierten Dipolen zwischen Molekülen in der Gasphase und Atomen auf der Oberfläche des Festkörpers. Da es sich um einen Prozess an einer Oberfläche handelt, sind hoch poröse Materialien mit hoher spezifischer Oberfläche für die Physisorption von Wasserstoff besonders geeignet.

Ziel dieser Doktorarbeit ist es, poröse Materialien, die unterschiedliche Porosität, Struktur und Zusammensetzung besitzen, für die physikalische Adsorption von Wasserstoff zu untersuchen. Insbesondere werden zwei Klassen von potentiellen Adsorbentien mit hoher spezifischer Oberfläche erforscht: kohlenstoffbasierte Materialien und metallorganische Gerüste. Durch unterschiedliche Messmethoden soll vor allem der Zusammenhang zwischen der Wasserstoffaufnahme sowie der Wechselwirkung mit H₂ Molekülen und der Struktur und Textur des Adsorbentien verstanden werden. Nur dieses Verständnis kann zu einer Optimierung der Struktur des Adsorbentien für eine Steigerung der Wasserstoffaufnahme führen. Die Messapparaturen, die für diese Untersuchungen angewandt worden sind, wurden außerdem speziell konstruiert, um sehr große Druck- und Temperaturbereiche abzudecken.

Messmethoden

Volumetrische Messungen:

Wasserstoffadsorptionsisothermen wurden bei unterschiedlichen Temperaturen von 77 bis 300 K und bei Drücken von 1,3 bis 70 bar mit einer manuell bedienten Sieverts Apparatur, die aus kleinen Volumina besteht, gemessen. Der Einsatz von kleinen Volumina ermöglicht es auch für kleine Probenmassen (150 mg - 300 mg), die Exzesswasserstoffaufnahme genau zu messen. Die Anlage wurde mit bekannten Metallhydriden kalibriert, und Sand wurde als nicht adsorbierendes Referenzmaterial benutzt.

Thermische Desorptionspektroskopie (TDS):

Die Anlage für thermische Desorptionspektroskopie wurde speziell gebaut, um bei tiefen Temperaturen zu messen. Die Probe wurde bei einem Druck von 25 mbar mit H_2 beladen und bis 20 K mit flüssigem He abgekühlt. Die Temperatur der Probe wurde dann mit einer konstanten Aufheizrate erhöht, und mit einem Quadrupolmassenspektrometer wurde der Partialdruck des desorbierten Wasserstoffs im Vakuum gemessen. Durch diese Messmethode kann man untersuchen, bei welcher Temperatur die H_2 -Moleküle von der Probe desorbiert werden. Diese Temperatur hängt mit der Aktivierungsenergie des Desorptionsprozesses zusammen. Adsorptionsplätze mit unterschiedlicher Aktivierungsenergie ergeben dabei verschiedene Maxima im Desorptionsspektrum. Nach einer geeigneten Kalibrierung der Anlage mit Metallhydriden wurde außerdem die Menge an desorbiertem Wasserstoff bestimmt. Zum ersten Mal wurde thermische Desorptionspektroskopie quantitativ bei diesen tiefen Temperaturen für die Untersuchung von H_2 -Adsorption angewandt.

Ramanspektroskopie:

Ramanspektroskopie ist eine optische Messmethode, die es ermöglicht, Vibrations- und Rotationsübergänge von homonuklearen zweiatomigen Molekülen wie H_2 zu untersuchen. Dafür wurde die das System Probe–Wasserstoff, mit einem Laser bestrahlt und die Frequenz der zurück gestreuten Strahlung gemessen. Die Frequenzdifferenz zwischen eingehender Laserstrahlung und zurück gestreuter Strahlung enthält die Information über die Energieänderung des Systems im Übergang. In dieser Arbeit wurde die Ramanspektroskopie angewandt, um die adsorbierte Wasserstoffphase zu untersuchen. Insbesondere wurden die Energie der Rotations- und Vibrationsvorgänge von freiem und adsorbiertem H_2 verglichen, da man erwartet, dass die Ramanverschiebung eines Moleküls von dessen Umgebung beeinflusst wird. Ramanspektroskopie wurde daher als Untersuchungsmethode benutzt, um die Wechselwirkung von H_2 an den Adsorptionsplätzen zu erforschen.

Poröse Materialien

Kohlenstoffnanostrukturen

Verschiedene Kohlenstoffmaterialien mit unterschiedlicher Struktur und Textur wurden für die Physisorption von Wasserstoff untersucht. Obwohl diese Materialien alle aus graphitähnlichen Kohlenstoffsechsecken bestehen, kann die Anordnung dieser C-Hexagone für verschiedene Proben sehr unterschiedlich sein. Ein Beispiel für eine geordnete Struktur sind einwandige Kohlenstoffnanoröhrchen, die in einem Bündel ein zweidimensionales, geordnetes Gitter bilden (Fig. 2.9). Im Gegensatz dazu sind in der Aktivkohle die Graphitplättchen regellos angeordnet, wodurch der Abstand zwischen Kohlenstoffebenen von wenigen Ångstrom, wie im Graphit, bis zur Mikroporengröße variieren kann^[24]. Außerdem wurden andere röhrenförmige Kohlenstoffmaterialien wie amorphe Nanoröhrchen^[53] und Mischungen aus einwandigen und mehrwandigen Kohlenstoffnanoröhrchen^[56] untersucht. Schließlich wurde poröser Kohlenstoff mit uniformer Porengröße, die durch Anwendung einer porösen Matrize synthetisch erhalten werden kann, erforscht.^[25]

Die untersuchten Proben besitzen eine BET^[11] (Brunauer-Emmet-Teller) spezifische Oberfläche, die von 22 m² g⁻¹ bis 2560 m² g⁻¹ reicht (Tab. 4-1).

Metallorganische Gerüste (MOFs)

Metallorganische Gerüste (MOFs) sind kristalline Koordinationspolymere, in denen Metallionen als Konnektoren durch organische Linker in einem dreidimensionalen und porösen Netzwerk verbunden sind.^[31] Typischerweise sind diese Konnektoren Ionen der Übergangsmetalle und die Linker aromatische Moleküle mit Karboxylatgruppen, die das Metallion koordinieren. Durch die Vielfalt an Metallionen und organischen Linkern, die eingesetzt werden können, ist es möglich, eine Vielzahl von verschiedenen Strukturen mit unterschiedlicher Porengröße herzustellen.

In dieser Arbeit wurden eine Reihe von MOFs mit unterschiedlicher Struktur und bestehend aus verschiedenen Bausteinen untersucht. Diese besitzen BET spezifische Oberflächen von $482 \text{ m}^2 \text{ g}^{-1}$ bis $2296 \text{ m}^2 \text{ g}^{-1}$ (Tabelle 5-1).

Ergebnisse und Diskussion

Kohlenstoffnanostrukturen

Für alle untersuchten Kohlenstoffmaterialien wurden die gleichen Isothermentypen für die H_2 -Adsorption erhalten: Bei 77 K zeigen alle Proben Typ I Isothermen mit Sättigung und Monolagenbildung bei hohem Druck (z.B. Fig. 4.1, Fig. 4.2). Bei Raumtemperatur (RT) steigt die Isotherme linear mit dem Druck an, was typisch für niedrige Adsorbatkonzentrationen ist. Bei tiefen Temperaturen wurden die Adsorptionsisothermen mit einem Langmuir Modell beschrieben, während sich bei RT die adsorbierten Moleküle wie ein ideales Gas verhalten weshalb die Isotherme mit einer linearen Henry Gleichung angepasst wurden.

Der Mechanismus des Adsorptions- und Desorptionsprozesses ist durch schnelle Kinetik und komplette Reversibilität charakterisiert, was darauf hinweist, dass Wasserstoff auf Kohlenstoffmaterialien durch Physisorption gespeichert wird. Das beste Material ist hoch poröse Aktivkohle, deren spezifische Oberfläche so groß wie die theoretische Oberfläche beider Seiten einer Graphitebene ist. Diese Probe speichert bei 77 K 4.5 gew% Wasserstoff. Im Gegensatz dazu beträgt die H_2 Speicherkapazität aller Materialien bei Raumtemperatur weniger als 0.5 gew% bei einem Maximaldruck von 65 bar.

Es wurde gezeigt, dass die Wasserstoffaufnahme auf Kohlenstoffnanostrukturen sowohl bei Raumtemperatur als auch bei 77 K mit ihrer spezifischen Oberfläche linear korreliert und unabhängig von weit reichender Ordnung, Krümmung oder Anordnung der Graphitplättchen im Material ist (Fig. 4.3). Die erhaltene Korrelation ist in guter Übereinstimmung mit dem theoretischen Modell^[65], und die maximale gespeicherte Dichte entspricht 80% der Dichte von flüssigem Wasserstoff. Obwohl die Wasserstoffaufnahme nicht von der Struktur des Materials abhängt, sondern nur von der spezifischen Oberfläche, wurden verschiedene Adsorptionsplätze für

Wasserstoff auf Kohlenstoffmaterialien mit unterschiedlicher Struktur beobachtet. Das thermische Desorptionsspektrum von Wasserstoff auf einwandigen Nanoröhrchen weist eindeutig auf die Anwesenheit von zwei Adsorptionsplätzen mit unterschiedlicher Energie hin, von denen H_2 bei unterschiedlicher Temperatur desorbiert wird (Fig. 4.9). Diese Plätze wurden der konvexen Oberfläche der Nanoröhrchen und der Position zwischen zwei nebeneinander liegenden Röhrchen, den so genannten „grooves“, zugeordnet. Im Gegensatz dazu zeigt das Desorptionsspektrum von H_2 auf Aktivkohle ein einziges, breites Maximum, das auf eine Verteilung unterschiedlicher Adsorptionsplätze mit ähnlicher Energie hinweist (Fig. 4.8). Dieses Spektrum spiegelt die Porenstruktur von Aktivkohle, die Poren mit unterschiedlichem Radius von wenigen Ångstrom bis Mikroporengröße besitzt wieder. Bei beiden Materialien, Kohlenstoffnanoröhrchen und Aktivkohle, wird bei Temperaturen unter 80 K 99.98 % des gesamten Wasserstoffgehalts desorbiert, was noch einmal zeigt, dass H_2 reversibel adsorbiert wird. Durch Kalibrierung der TDS-Anlage war es möglich, quantitativ die Menge an desorbiertem Wasserstoff zu bestimmen, die in beiden Fällen der Monolagenbedeckung entspricht.

Ramanspektroskopie wurde angewandt, um die Wechselwirkung des Adsorbers auf die adsorbierten Wasserstoffmoleküle zu untersuchen. Insbesondere kann man in der Q-Bande des Wasserstoffs, die dem Übergang mit $\Delta\nu = 1$ und $\Delta J = 0$ entspricht, bei 40 K und einem Druck von maximal 22 bar eine Aufspaltung in drei unterschiedliche Maxima beobachten (Fig. 4.14). Ein Maximum wurde dem freien Wasserstoff zugeordnet, während die beiden anderen Maxima, die um maximal 2 cm^{-1} zu höheren Ramanverschiebungen im Vergleich zu freiem Wasserstoff beobachtet wurden, dem adsorbierten H_2 zugeordnet wurden. Der kleine Unterschied ist charakteristisch für eine schwache van der Waals Wechselwirkung ohne Ladungstransfer zwischen Adsorber und H_2 -Molekülen.^[76] Außerdem wurde unter gleichen Druck- und Temperaturbedingungen das Ramanspektrum der Kohlenstoffnanoröhrchen untersucht (Fig. 4.19). Im Vergleich zur selben Probe in Vakuum wurde unter Wasserstoffdruck und 40 K eine Verschiebung von nur 2 cm^{-1} in der TM-Mode, einer charakteristische Phonon-Mode von einwandigen Kohlenstoffnanoröhrchen, gemessen. Dieses Ergebnis stimmt mit der kleinen

Verschiebung, die man in den Ramanspektren des adsorbierten H₂ beobachtet hat, überein.

Metallorganische Gerüste:

Verschiedene metallorganische Gerüste mit unterschiedlicher Struktur und Zusammensetzung wurden für die Physisorption von Wasserstoff vermessen. Aufgrund der höchsten spezifischen Oberfläche zeigt MOF-5^[84,32], ein Zn²⁺-basiertes MOF mit einem Sättigungswert von 5.1 gew% bei 77 K die größte Wasserstoffaufnahme (Fig. 5.11). Allerdings ist bei niedrigem Druck die Wasserstoffaufnahme in Cu-BTC^[91], das kleinere Poren und ungesättigte Cu²⁺-Zentren besitzt, größer (Fig. 5.12, Fig. 5.14). Die unterschiedliche Druckabhängigkeit in den Adsorptionisothermen von Cu-BTC und MOF-5 hängt mit zwei Faktoren zusammen: Bei niedrigen Drücken ist die Wasserstoffspeicherkapazität von der Adsorptionenthalpie beeinflusst, die negativer für die Adsorption von H₂ auf Cu-BTC ist. Im Gegensatz dazu ist bei hohem Druck die H₂-Aufnahme von der spezifischen Oberfläche des Adsorbers, die für MOF-5 größer ist als für Cu-BTC, abhängig.

Es wurde außerdem gezeigt, dass, ähnlich wie bei Kohlenstoffmaterialien, der Sättigungswert der H₂-Adsorptionisothermen aller MOFs, mit der spezifischen Oberfläche der metall-organischen Gerüste korreliert und unabhängig von ihrer Struktur oder Zusammensetzung ist (Fig. 5.13). Diese Schlussfolgerungen stimmen gut mit Grand Canonical Monte Carlo Simulationen aus der Literatur überein.^[98]

Bei Raumtemperatur ist die Wasserstoffspeichermenge in allen MOFs kleiner als 0.4 gew%, allerdings kann dieser Wert bei 200 K verdreifacht werden. Die isosterische Adsorptionwärme von H₂ in den untersuchten MOFs entspricht ungefähr 4 kJ mol⁻¹, ein Wert der charakteristisch für die Physisorption von Wasserstoff ist. Außerdem wurde gezeigt, dass Wasserstoff reversibel in MOFs gespeichert wird, was darauf hinweist, dass metallorganische Gerüste durch Adsorption von H₂ nicht kollabieren.

Thermische Desorptionsspektroskopie wurde bei tiefen Temperaturen angewandt, um die Adsorptionsplätze in den genau definierten Strukturen der MOFs zu bestimmen. Ähnlich wie bei Kohlenstoffmaterialien zeigen die Desorptionsspektren

von H₂ auf MOFs, dass in Vakuum bei Temperaturen bis 80 K der gesamte Wasserstoffgehalt desorbiert wird (Fig. 5.21). Dieses Ergebnis stimmt mit den niedrigen Adsorptionseenthalpien, die aus den Isothermen bestimmt wurden, überein. Für Cu-BTC wurden mit thermischer Desorptionsspektroskopie zwei Adsorptionszentren für H₂ mit unterschiedlicher Energie bestimmt (Fig. 5.16). Diese wurden jeweils den Hauptporen, die einen Durchmesser von 11 Å haben, und den kleineren Seitenporen der Struktur zugeordnet. Analog dazu konnten für die anderen metallorganischen Gerüste die Adsorptionsplätze, die durch die TDS Messungen bestimmt wurden, mit der Porenstruktur des kristallinen Netzwerkes korreliert werden. Cu-basierte metallorganische Gerüste zeigten unter allen MOF-Proben die interessantesten Eigenschaften für die Wasserstoffspeicherung: Hohe Wasserstoffaufnahme bei niedrigem Druck und hohe Desorptionstemperaturen, die beide ein Hinweis für die stärkere Wechselwirkung von H₂ mit den Cu-MOFs im Vergleich zu anderen metallorganischen Gerüsten sind. Aus diesem Grund wurde die Wasserstoffadsorption auf Cu-BTC auch mit Ramanspektroskopie untersucht. Ähnlich wie bei Kohlenstoffnanoröhrchen und Aktivkohle zeigt die Q-Linie von molekularem Wasserstoff eine Aufspaltung. Ein Maximum dieser Linie wurde den freien H₂-Molekülen zugeordnet, während das zweite Maximum, das ca. 1.5 cm⁻¹ zu höheren Wellenzahlen verschoben ist, von adsorbiertem Wasserstoff stammt (Fig. 5.24, Fig. 5.25). Die kleine Wellenzahlverschiebung im Vergleich zum freien Wasserstoff zeigt, dass auch für metallorganische Gerüste die Speicherung von Wasserstoff durch schwache van der Waals Kräfte stattfindet und der Ladungstransfer zwischen H₂-Molekülen und Adsorber vernachlässigt werden kann.

Schlussfolgerungen

Zwei unterschiedliche Klassen von porösen Materialien, kohlenstoffmaterialien und metallorganische Gerüste, wurden für die Physisorption von Wasserstoff untersucht. Ein Vergleich zwischen den hier vorgestellten Messungen und den Literaturdaten über Zeolite und andere poröse Materialien, zeigten, dass für alle Materialien die maximale Speicherkapazität bei 77 K ähnlich mit der spezifischen Oberfläche korreliert und unabhängig von der Zusammensetzung und der Struktur des Adsorbers

ist. Allerdings ist der Druck, bei der dieser Sättigungswert erreicht wird, stark materialabhängig. So wurde zum Beispiel mit einem Vergleich zwischen zwei metallorganischen Gerüsten mit genau definierter Porenstruktur gezeigt, dass Materialien mit kleineren Poren eine stärkere Wechselwirkung mit H₂-Molekülen besitzen und daher bereits bei niedrigerem Druck den Sättigungswert erreichen. Weiterhin wurde zum ersten Mal thermische Desorptionsspektroskopie bei Temperaturen nahe an 20 K für die Untersuchung von Wasserstoffspeicherung auf Kohlenstoffmaterialien und metallorganischen Gerüste angewandt. Diese Methode ermöglichte es, die Adsorptionsplätze mit der Porenstruktur des Adsorbers sowohl für Kohlenstoffproben als auch für MOFs zu korrelieren. Außerdem konnte man durch geeignete Kalibrierung zum ersten Mal ein quantitatives Desorptionsspektrum von Wasserstoff adsorbiert auf porösen Materialien messen.

Die erhaltenen Ergebnisse zeigten, dass thermische Desorptionsspektroskopie bei tiefen Temperaturen eine geeignete Methode zur Untersuchung von Adsorptionsplätzen in porösen Materialien ist und im Vergleich zu anderen, aufwendigeren Methoden, wie inelastische Neutronenbeugung, eingesetzt werden kann. Außerdem wurde die Ramanspektroskopie als alternative Methode benutzt, um die Umgebung des adsorbierten Wasserstoffs zu untersuchen und Informationen über die Wechselwirkung mit dem Adsorber zu erhalten.

Die benutzten Messmethoden sind im Bereich der Physisorption von Wasserstoff außerdem vollkommen neu, so sind in der Literatur keine quantitative TDS-Messungen bei tiefen Temperaturen bekannt, welche die Identifizierung von Wasserstoffadsorptionsplätzen in porösen Materialien ermöglichen. Ramanspektroskopie für die Untersuchung von adsorbiertem H₂ wurde zum ersten Mal im Jahr 2002 auf Kohlenstoffnanoröhrchen angewandt,^[79] zwei weitere Arbeiten über Aktivkohle und MOF-5 erschienen erst im letzten Jahr.^[76,101] Die geringe Anzahl an Publikationen über Ramanmessungen zur Untersuchung der Wechselwirkung von H₂ mit porösen Materialien zeigt, dass das Potential dieser Messmethode noch nicht völlig erkannt worden ist. Mit Messungen auf unterschiedlichen Kohlenstoffmaterialien, wie einwandige Nanoröhrchen und Aktivkohle wurde in dieser Arbeit gezeigt, dass bei tiefen Temperaturen Ramanspektroskopie erfolgreich für diese Art von Untersuchungen eingesetzt

werden kann. Die erhaltenen Ergebnisse bestätigen frühere Arbeiten, in Bezug der kleinen Verschiebungen der Ramanlinien entsprechend der Vibration von adsorbiertem im Vergleich zum freien Wasserstoff. Außerdem wurde die Untersuchung auch auf die Rotation von den adsorbierten Wasserstoffmolekülen und auf die Phonon-Mode der Nanoröhrchen erweitert. Die Ramanmessungen von Wasserstoff auf Cu-basierten metallorganischen Gerüsten unterscheiden sich stark von den Ergebnissen aus der Literatur, sind allerdings in guter Übereinstimmung mit den Messungen auf Kohlenstoffproben.

In den letzten zwei Jahren ist die Anzahl an Publikationen über MOFs deutlich gestiegen, was das große wissenschaftliche Interesse an diesen Systemen beweist. In dieser Doktorarbeit wurden neue metallorganische Gerüste untersucht und neue Erkenntnisse über MOFs, die schon bekannt waren aber nur beschränkt untersucht worden waren, erbracht. So hatte man z. B. die Speicherkapazität in MOF-5 und IRMOF-8 schon in 2004 bei niedrigen Drücken untersucht.^[87] In dieser Doktorarbeit wurden die Adsorptionsisothermen bis in den Sättigungsbereich gemessen und die Untersuchungen auf die Unterschiede zwischen verschiedenen MOFs konzentriert. So wurde auch zum ersten Mal die Korrelation zwischen maximalem Adsorptionswert und spezifischer Oberfläche auch für MOFs erkannt, die später auch von anderen Gruppen bestätigt wurde.^[34]

Die hier vorgestellten Ergebnisse zeigen eine Möglichkeit auf, poröse Materialien so zu strukturieren, dass technologisch relevante Wasserstoffdichten erreicht werden können. Dementsprechend wurde nachgewiesen, dass nicht nur eine hohe spezifische Oberfläche ausschlaggebend ist, sondern auch die Porenstruktur des Adsorbers. Kleine Poren erwiesen sich als notwendig, um auch bei niedrigem Druck hohe Speicherkapazitäten zu erreichen.

Appendix A

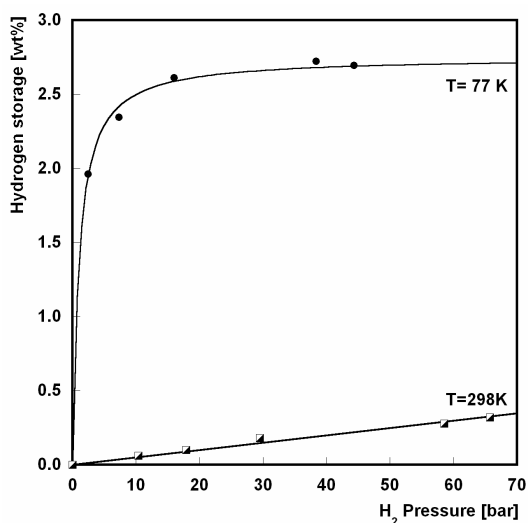


Fig. A-1 (left): Hydrogen adsorption isotherm of activated carbon III, measured at 77 K (circles) and room temperature (squares).

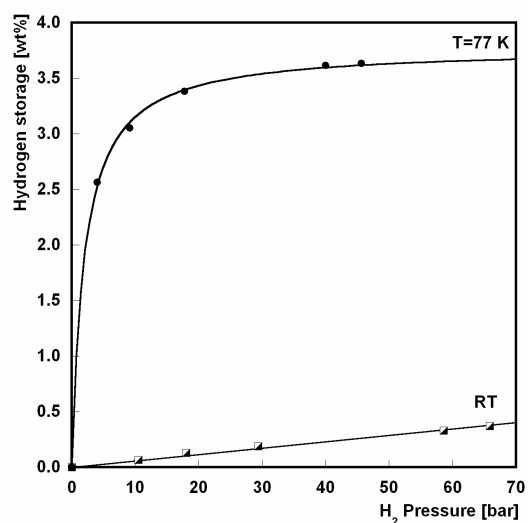


Fig. A-2 (right): Hydrogen adsorption isotherm of activated carbon II, measured at 77 K (circles) and room temperature (squares).

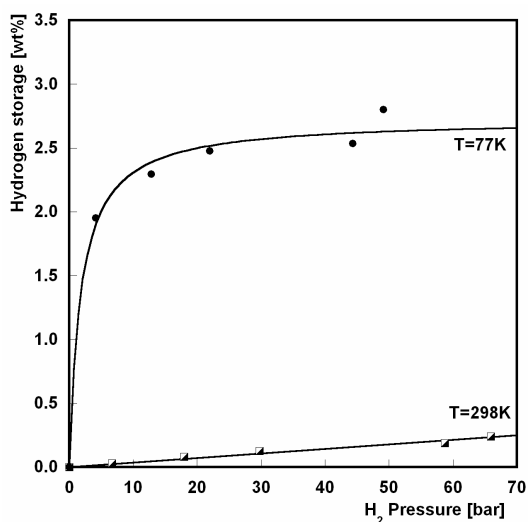


Fig. A-3 (left): Hydrogen adsorption isotherm of porous carbon I, measured at 77 K (circles) and room temperature (squares).

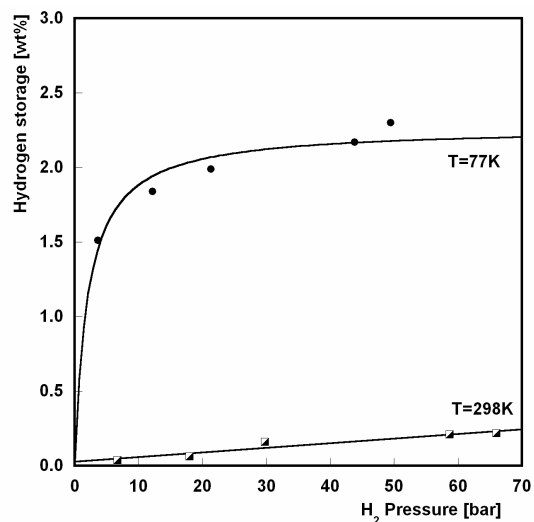


Fig. A-4 (right): Hydrogen adsorption isotherm of porous carbon II, measured at 77 K (circles) and room temperature (squares).

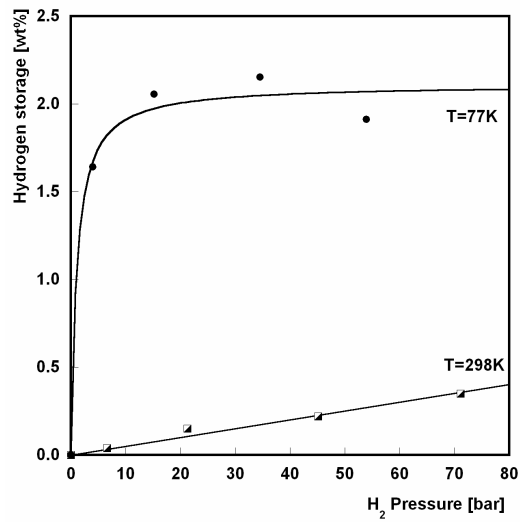


Fig. A-5: Hydrogen adsorption isotherm of purified SWCNTs I, measured at 77 K (circles) and room temperature (squares).

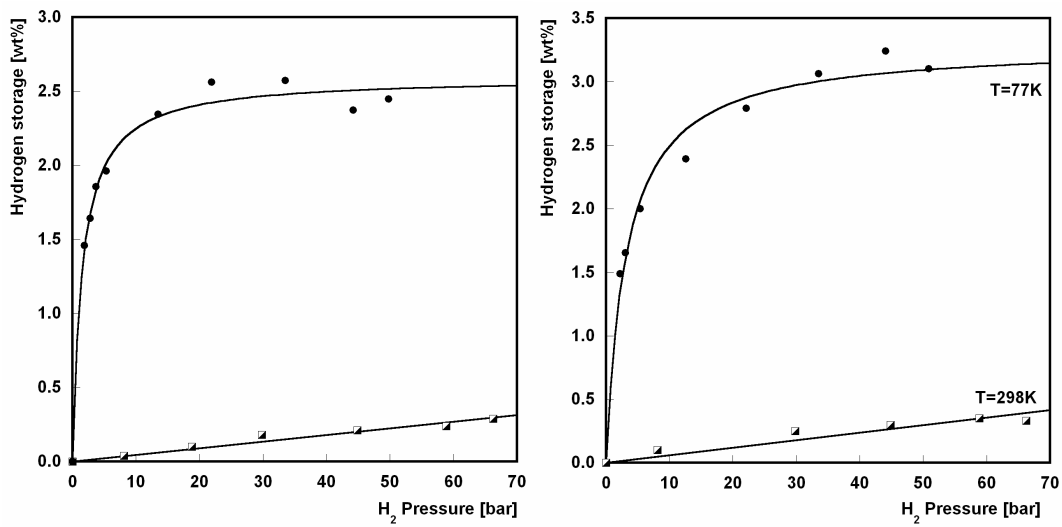


Fig. A-6 (left): Hydrogen adsorption isotherm of porous carbon III, measured at 77 K (circles) and room temperature (squares).

Fig. A-7: Hydrogen adsorption isotherm of porous carbon IV, measured at 77 K (circles) and room temperature (squares).

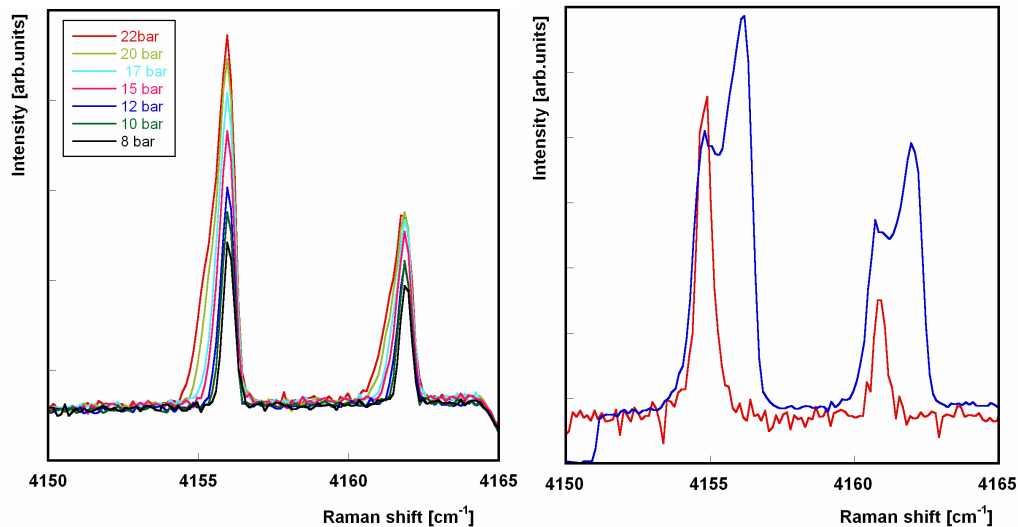


Fig. A-8 (left): Q(1) and Q(0) lines of hydrogen adsorbed on SWCNTs sample I at 40 K and variable pressure.

Fig. A-9 (right): Q(0) and Q(1)-line of hydrogen adsorbed on SWCNTs sample II at 40 K and 20 bar (blue) compared to the Q(0) and Q(1) line of hydrogen in presence of graphite at 40 K and 20 bar (red). Owing to the small intensity of the lines of hydrogen in presence of graphite, two different intensity scales are chosen.

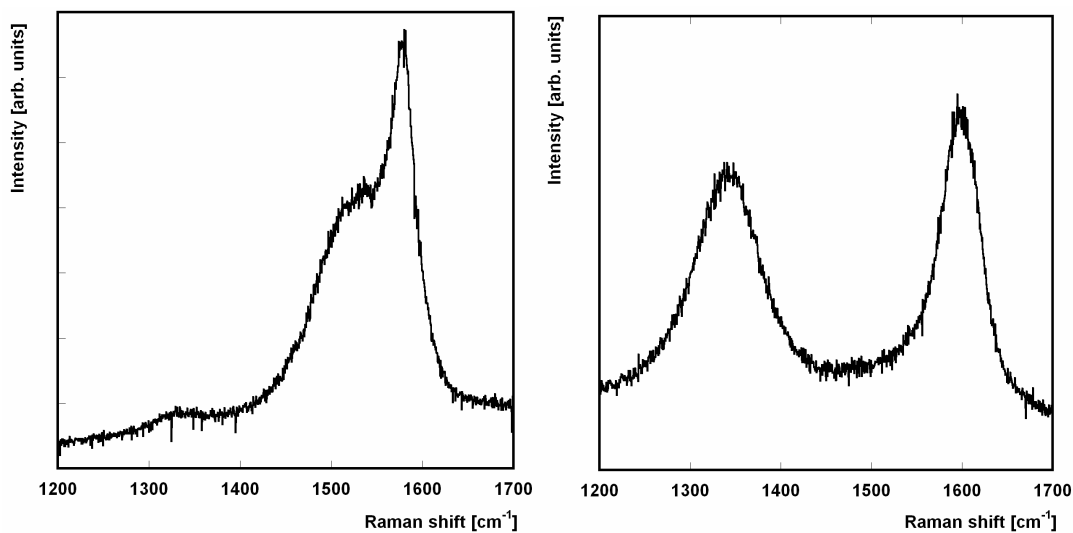


Fig. A-10 (left): Raman spectrum of SWCNTs sample I, obtained with a laser radiation of 514 nm.

Fig. A-11 (right): Raman spectrum of activated carbon, obtained with a laser radiation of 514 nm.

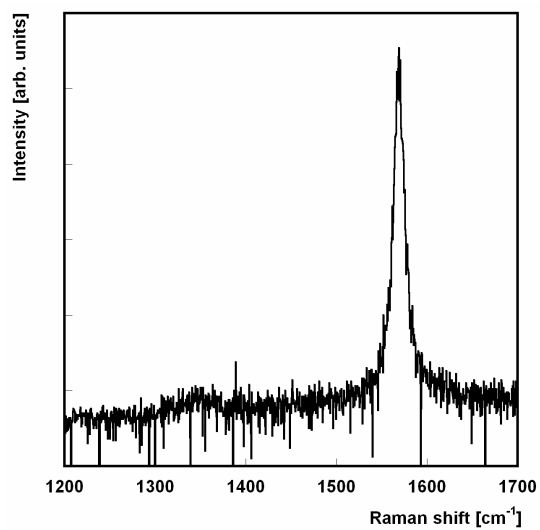


Fig. A-12: Raman spectrum of graphite, obtained with a laser radiation of 514 nm

Appendix B

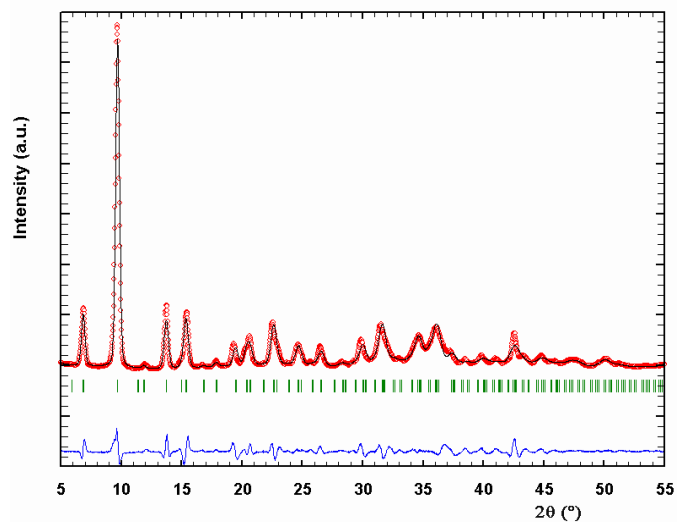


Fig. B-1: X-Ray diffraction pattern of MOF obtained with the laboratory synthesis, the Le Bail profile matching in black, the difference between measured and calculated intensities in blue and Bragg-position for MOF-5 in green.^[86]

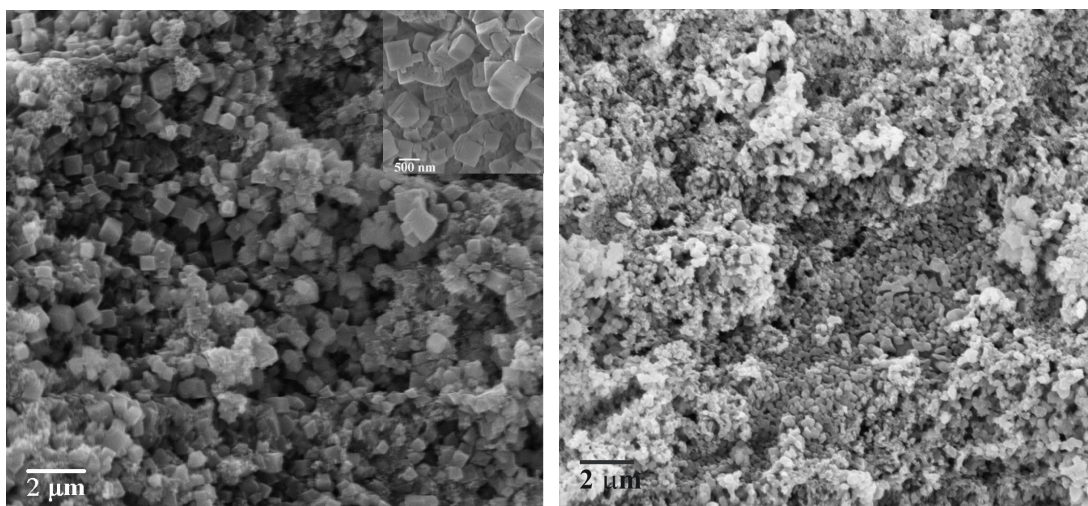


Fig. B-2 (left): SEM picture of cubic crystallites of MOF-5 produced through the small scale laboratory synthesis adding H_2O_2 .^[86]

Fig. B-3 (right): SEM picture of cubic crystallites of MOF-5 produced through the small scale laboratory synthesis, without H_2O_2 .^[86]

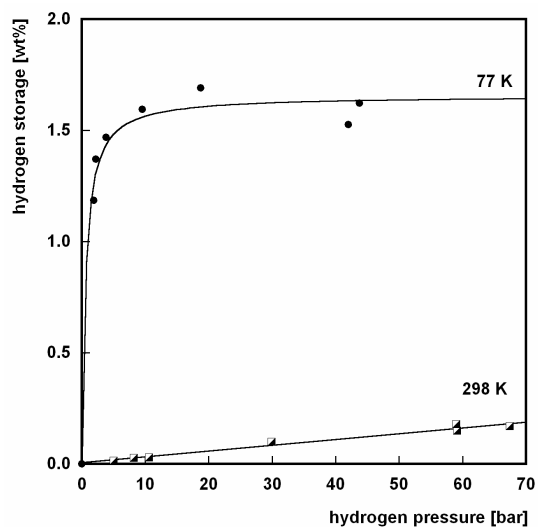


Fig. B-4 (left): Hydrogen adsorption isotherm of MOF-5 at 77 K (circles) and 298 K (squares), prepared by laboratory synthesis.

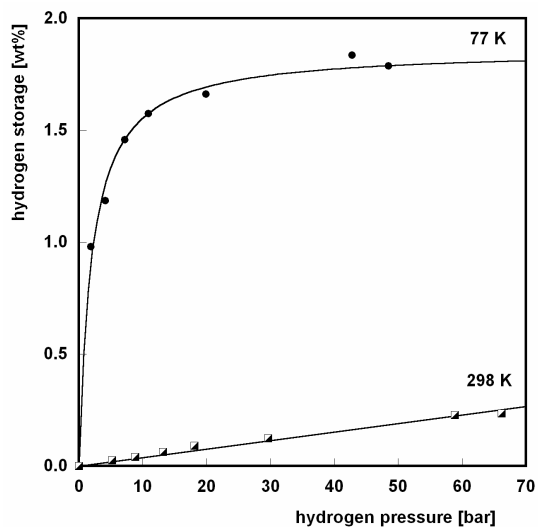


Fig B-5 (right): Hydrogen adsorption isotherm of Ni-MOF (circles) at 77 K and 298 K (squares).

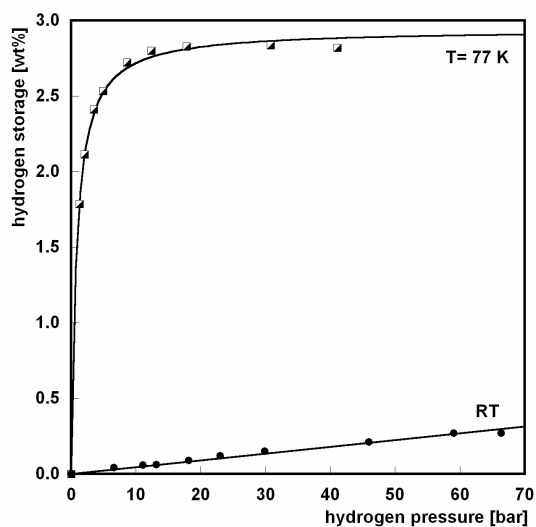


Fig. B-6 (left): Hydrogen adsorption isotherm of Al-MOF at 77 K (squares) and 298K (circles).

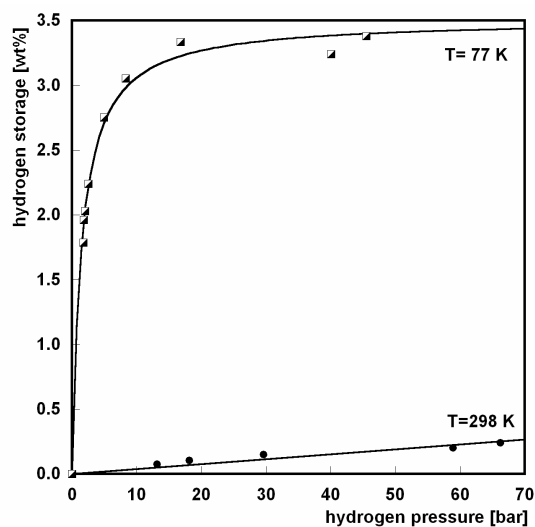


Fig. B-7 (right): Hydrogen adsorption isotherm of IRMOF-8 measured at 77 K (squares) and 298 K (circles).

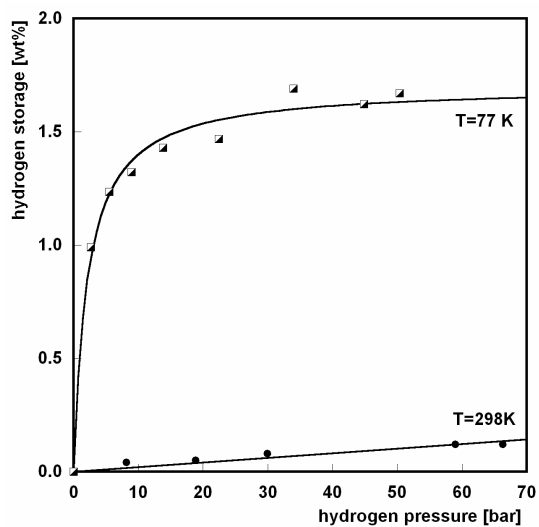


Fig. B-8: Hydrogen adsorption isotherm of MR 3677 measured at 77 K (squares) and 298 K (circles).

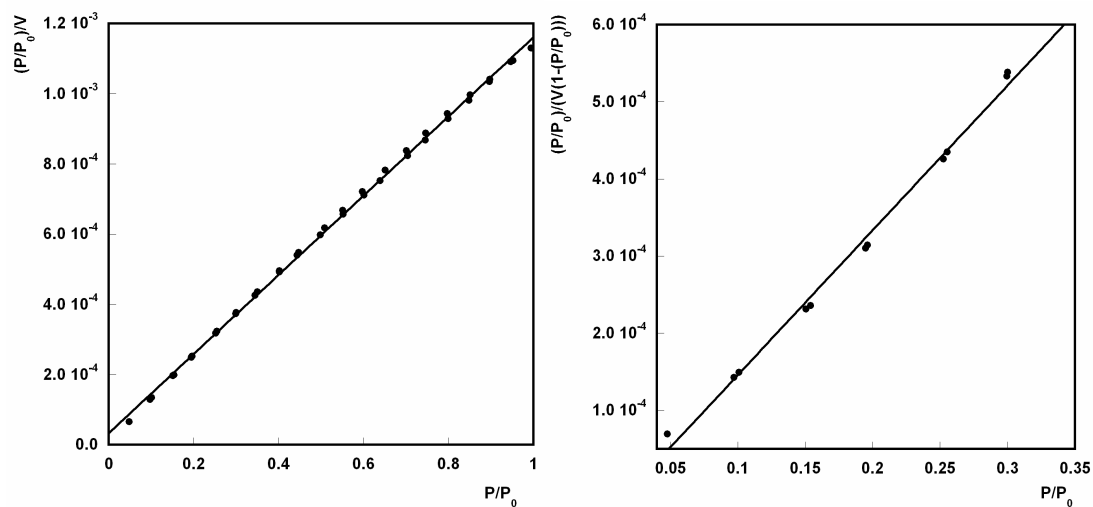


Fig. B-9 (left): BET-plot of the N₂ adsorption isotherms of MOF-5 at 77 K, P/P₀ is the relative pressure and V the volume of the adsorbed gas.

Fig. B-10 (right): Langmuir-plot of the N₂ adsorption isotherm of MOF-5 at 77 K, P/P₀ is the relative pressure and V the volume of the adsorbed gas.

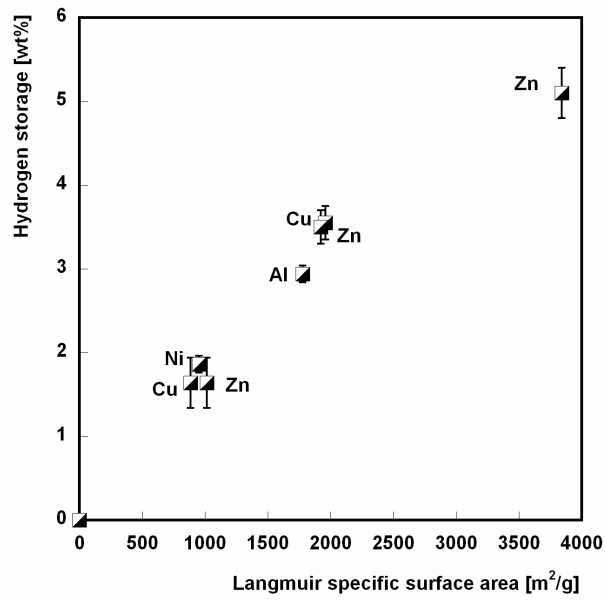


Fig. B-11: Saturation value of the hydrogen storage capacity of MOFs correlated to the Langmuir specific surface area. Corresponding metal centres are indicated.

References

- [1] L. Schlapbach, A. Züttel, *Nature* 414 (2001) 353.
- [2] A. Züttel, *Naturwissenschaften* 91 (2004) 157.
- [3] N. L. Rosi, J. Eckert, M. Eddaoudi, D. T. Vodak, J. Kim, M. O'Keeffe, O. M. Yaghi, *Science* 300 (2003) 1127.
- [4] G. Férey, M. Latroche, C. Serre, F. Millange, T. Loiseau, A. Percheron-Guégan, *Chem. Comm.* 24 (2003) 2976.
- [5] F. Rouquerol, J. Rouquerol, K. Sing, *Adsorption by Powders and Porous Solids*, Academic Press, San Diego, London, Boston, New York, Sidney, Tokyo, Toronto, 1999.
- [6] IUPAC Recommendations, *Pure Appl. Chem.* 57 (1985) 603.
- [7] S. Lowell, J. E. Shields, *Powder Surface Area and Porosity*, 3rd Edition. Chapman & Hall, 1991.
- [8] I. Langmuir, *J. Am. Chem. Soc.* 22 (1916) 2221.
- [9] Y. Ye, C. C. Ahn, C. Witham, B. Fultz, J. Liu, A. G. Rinzler, D. Colbert, K. A. Smith, R. E. Smalley, *Appl. Phys. Lett.* 74 (1999) 2307.
- [10] M. Shiraishi, T. Takenobu, M. Ata, *Chem. Phys. Lett.* 367(5-6) (2003) 633.
- [11] S. Brunauer, P. H. Emmett, E. Teller, *J. Am. Chem. Soc.* 60 (1938) 309.
- [12] M. T. González, A. Sepúlveda-Escribano, M. Molina-Sabio, F. Rodríguez-Reinoso, *Langmuir* 11 (1995) 2151.

- [13] A. L. Myers, P. A. Monson, *Langmuir* 18 (2002) 10261.
- [14] E. Ozdemir, Chemistry of the adsorption of carbon dioxide by Argonne premium coals and a model to simulate CO₂ sequestration in coal seams, PhD thesis.
- [15] Q. Wang, J. K. Johnson, *J. Chem. Phys.* 110 (1999) 577.
- [16] G. Garberoglio, A. I. Skoulidas, J. K. Johnson, *J. Phys. Chem, B* 109 (2005) 13094.
- [17] C. V. Raman, K.S. Krishan, *Nature* 121 (1928) 501.
- [18] J. I. Steinfeld, *Molecules and radiation: an introduction to modern molecular spectroscopy*, The MIT Press, Cambridge, Massachusetts, London, England, 1979.
- [19] *Pure and Applied Cryogenics Vol. 5: Liquid Hydrogen*, Pergamon Press, Oxford, London, New York, Paris Braunschweig, Edinburgh, Toronto, 1966.
- [20] G. Savage, *Carbon-Carbon Composites*, Chapman & Hall, 1993.
- [21] B. K. Pradhan, G. U. Sumanasekera, K. W. Adu, H. E. Romero, K. A. Williams, P. C. Eklund, *Physica B* 323 (2002) 115.
- [22] M. J. Bronikowski, P. A. Willis, D. T. Colbert, K. A. Smith, R. E. Smalley, *J. Vac. Sci. Technol. A* 19 (2001) 1800.
- [23] K. Balasubramanian, M. Burghard. *Small*, 1 (2005) 180.
- [24] F. Schüth, K. S. W. Sing, J. Weitkamp, *Handbook of Porous Solids*, Vol. 3, Wiley-VCH, Weinheim, 2002.
- [25] R. Chahine, T. K. Bose, *Int. J. Hydrogen Energy*, 19 (1994) 161.

- [26] M. G. Nijkamp, J. E. M. J Raaymakers, A. J. van Dillen, K. P. de Jong, *Appl. Phys. A* 72 (2001) 619.
- [27] H. Darmstadt, C. Roy, S. Kaliaguine, S. J. Choi, R. Ryoo, *Carbon* 40 (2002) 2673.
- [28] R. Ryoo, S. H. Joo, S. Jun, *J. Phys. Chem. B*, 103 (1999) 7743.
- [29] T. Kyotani, T. Nagai, S. Inoue, A. Tomita, *Chem. Mater.* 9 (1997) 609.
- [30] B. F. Hoskins, R. Robson, *J. Am. Chem. Soc* 111 (1989) 5962.
- [31] M. Eddaoudi, D. B. Moler, H. Li, B. Chen, T. M. Reineke, M. O’Keeffe, O. M. Yaghi, *Acc. Chem. Res.* 34 (2001) 319.
- [32] H. Li, M. Eddaoudi, M. O’Keeffe, O. M. Yaghi, *Nature* 402 (1999) 279.
- [33] J. L. C. Rowsell, O. M. Yaghi, *Angew. Chem. Int. Ed.* 44 (2005) 4670.
- [34] A. G. Wong-Foy, A. J. Matzger, O. M. Yaghi, *J. Am. Chem. Soc.* 128 (2006) 3494.
- [35] M. Eddaoudi, J. Kim, N. Rosi, D. Vodak, J. Wachter, M. O’Keeffe, O. M. Yaghi, *Science* 295 (2002) 469.
- [36] T. Düren, L. Sarkisov, O. M. Yaghi, R. Q. Snurr, *Langmuir* 20 (2004) 2683.
- [37] F. Schüth, K. S. W. Sing, J. Weitkamp, *Handbook of Porous Solids, Vol.2*, Wiley-VCH, Weinheim, 2002.

- [38] U. Müller, M. Schubert, F. Teich, H. Pütter, K. Schierle-Arndt, J. Pastré, J. Mater. Chem. 16 (2006) 626.
- [39] U. Müller, H. Pütter, M. Hesse, H. Wessel, German Patent 10355087, 2005.
- [40] M. P. Attfield. Science Progress 85 (2002) 319.
- [41] H. W. Langmi, A. Walton, M. M. Mamouri, S. R. Johnson, D. Book, J. D. Speight, P. P. Edwards, I. Gameson, P. A. Anderson, I. R. Harris. J. Alloys Comp. 356-357 (2003) 710.
- [42] G. G. Tibbetts, G. P. Meisner, C. H. Olk. Carbon 39 (2001) 2291.
- [43] hydpark.ca.sandia.gov.
- [44] M. Rzepka, P. Lamp. M. A. de la Casa-Lillo. J. Phys. Chem. B 102 (1998) 10894.
- [45] P. Malbrunot, D. Vidal, J. Vermesse, R. Chahine, T. K. Bose. Langmuir 13 (1997) 539.
- [46] Y. Ye, Interaction of hydrogen with novel carbon materials, PhD thesis.
- [47] F. von Zeppelin, H. Reule, M. Hirscher, J. Alloys Comp. 330-332 (2002) 723.
- [48] D. Blanchard, H. W. Brinks, B. C. Hauback, P. Norby, Materials Science and Engineering B 108 (2004) 54.
- [49] F. von Zeppelin, M. Haluška, M. Hirscher, Thermochemica Acta 404 (2003) 251.
- [50] E. Wicke, G. H. Nernst, Berichte der Bunsengesellschaft 68 (1964) 224.

- [51] A. Stern, A. Resnik, D. Shaltiel, *J. Phys. F: Met. Phys.* 14 (1984) 1625.
- [52] A. M. de Jong, J. W. Niemantsverdriet, *Surface Science* 233 (1990) 355.
- [53] Y. Liu, S. Xiaolong, Z. Tingkai, Z. Jiewu, M. Hirscher, F. Phillipp, *Carbon* 42 (2004) 1852.
- [54] U. Dettlaff-Weglisowska, S. Roth, XV Winterschool/ Euroconference Kirchberg. American Institute of Physics: Tirol Austria; 2001, p. 171.
- [55] A. V. Okotrub, L.G. Bulusheva, D. Tomanek, *Chem. Phys. Lett.* 289 (1998) 341.
- [56] V. A. Ryzhkov, *Physica B* 323 (2002) 324.
- [57] E. Terrés, B. Panella, T. Hayashi, Y. A. Kim, M. Endo, J. M. Dominguez, M. Hirscher, H. Terrones, M. Terrones, *Chem. Phys. Lett.* 403 (2005) 363.
- [59] S. Brunauer, S. Mikhail, E. E. Boder, *J. Collid Interface Sci.* 26 (1968) 45.
- [60] A. Züttel, P. Sudan, Ph. Mauron, T. Kiyobayashi, Ch. Emmenegger, L. Schlapbach. *Int. J. Hydrogen Energy* 27 (2002) 203.
- [60] K. Kadono, H. Kajiura, M. Shiraishi, *Appl. Phys. Lett* 83 (2003) 3392.
- [61] R. D. McCarty, *Hydrogen: Its technology and implications, Hydrogen properties Vol III.* Cleveland: CRC Press, 1975.
- [62] S.-P. Chan, G. Chen, X. G. Gong, Z.-F. Liu, *Phys. Rev. Lett.* 87 (20) (2001) 205502-1.

- [63] H. Atsumi, *J. Nucl. Mater.* 313-316 (2003) 543.
- [64] N. Texier-Mandoki, J. Dentzer, T. Piquero, S. Saadallah, P. David, C. Vix-Guterl, *Carbon* 42 (2004) 2744.
- [65] A. Züttel, P. Sudan, P. Mauron, P. Wenger, *Appl. Phys. A*, 78 (2004) 941.
- [66] F. Tran, J. Weber, T. A. Wesolowski, F. Cheikh, Y. Ellinger, F. Pauzat. *J. Phys. Chem. B.* 106 (2002) 8689.
- [67] J. S. Arellano, L. M. Molina, A. Rubio, J. A. Alonso, *J. Chem. Phys.* 112 (2000) 8114.
- [68] M. A. de la Casa-Lillo, F. Lamari-Dakrim, D. Cazorla-Amorós, A. Linares-Solano, *J. Phys. Chem. B* 106 (2002) 10930.
- [69] R. Gadiou, S.-E. Saadallah, T. Piquero, P. David, J. Parmentier, C. Vix-Guterl, *Microporous and Mesoporous Materials* 79 (2005) 121.
- [70] K. A. Williams, P. C. Eklund, *Chem. Phys. Lett.* 320 (2000) 352.
- [71] P. A. Georgiev, D. K. Ross, A. De Monte, U. Montaretto-Marullo, R. A. H. Edwards, A. J. Ramirez-Cuesta, M. A. Adams, D. Colognesi, *Carbon* 43 (2005) 895.
- [72] T. Wilson, A. Tyburski, M. R. DePies, O. E. Vilches, D. Becquet, M. Bienfait, *J. Low. Temp. Phys.* 126 (2002) 403.
- [73] M. S. Dresselhaus, P. C. Eklund, *Advances in Physics*, 49 (2000) 705.
- [74] E. C. Looi, J. C. Stryland, H. L. Welsh, *Can. J. Phys.* 56 (1978) 1102.

- [75] A. D. May, G. Varghese, J. C. Stryland, H. L. Welsh, *Can. J. Phys.* 42 (1965) 1058.
- [76] A. Centrone, L. Brambilla, G. Zerbi, *Phys. Rev. B*, 71 (2005) 245406.
- [77] A. D. May, J. D. Poll, *Can. J. Phys.* 43 (1964) 1863.
- [78] S. J. V. Frankland, D. W. Bernner, *Chem. Phys. Lett.* 334 (2001) 18.
- [79] K. A. Williams, B. K. Pradhan, P. C. Eklund, M. K. Kostov, M. W. Cole, *Phys. Rev. Lett.* 88 (2002) 165502.
- [80] H. G. Schimmel, G. J. Kearly, M. G. Nijkamp, C. T. Visser, K. P. De Jong, F. Mulder, *Chem. Eur. J.* 9 (2003) 4764.
- [81] S. S. Bhatnagar, E. J. Allin, H. L. Welsh, *Can. J. Phys.* 40 (1962) 9.
- [82] M. S. Dresselhaus G. Dresselhaus, R. Saito, A. Joris, *Physics Report* 409 (2005) 47.
- [83] A. M. Rao, P. C. Eklund, S. Bandow, A. Thess, R. E. Smalley, *Nature* 388 (1997) 257.
- [84] O. M. Yaghi, M. O’Keeffe, N. W. Ockwig, H. K. Chae, M. Eddaoudi, J. Kim, *Nature* 423 (2003) 705.
- [85] B. Panella, M. Hirscher, H. Pütter, U. Müller, *Adv. Funct. Mat.* 16 (2006) 520
- [86] B. Panella, M. Hirscher, *Adv. Mat.* 17 (2005) 538.
- [87] J. L. C. Rowsell, A. R. Millward, K. S. Park, O. M. Yaghi, *J. Am. Chem. Soc.* 126 (2004) 5666.

- [88] L. Huang, H. Wang, J. Chen, Z. Wang, J. Sun, D. Zhao, Y. Yan, *Microporous and Mesoporous Materials* 58 (2003) 105.
- [89] A. Le Bail, H. Duroy, J. L. Fourquet, *Mater. Res. Bull.* 23 (1988) 447.
- [90] A. Dailly, J. J. Vajo, C. C. Ahn, *J. Phys. Chem. B* 110 (2006) 1099.
- [91] S. S.-Y. Chui, S. M.-F. Lo, J. P. H. Charmant, A. Guy Orpen, I. D. Williams, *Science* 283 (1999) 1148
- [92] A. Vishnyakov, P. I. Ravikovitch, A. V. Neimark, M. Bülow, Q. M. Wang, *Nano Letters* 3 (2003) 713
- [93] K. Schlichte, T. Kratzke, S. Kaskel, *Microporous and Mesoporous materials* 73 (2004) 81.
- [97] Q. M. Wang, D. Shen, M. Bülow, M. L. Lau, S. Deng, F. R. Fitch, N. O. Lemcoff, J. Semanscin, *Microporous and mesoporous materials* 55 (2002) 217.
- [97] P. D. C. Dietzel, B. Panella, M. Hirscher, R. Blom, H. Fjellvåg, *Chem. Commun* (2006) 959.
- [96] P. Krawiec, M. Kramer, M. Sabo, R. Kunschke, H. Fröde, S. Kaskel, *Adv. Eng. Mater.* 8 (2006) 293.
- [97] B. Chen, N. W. Ockwig, A. R. Millward, D. S. Contreras, O. M. Yaghi, *Angew. Chem. Int. Ed.* 44 (2005) 4745.
- [98] H. Frost, T. Düren, R. Q. Snurr, *J. Phys. Chem.* 110 (2006) 9565.

- [99] C. Prestipino, L. Regli, J. G. Vitillo, F. Bonino, A. Damin, C. Lamberti, A. Zecchina, P. L. Solari, K. Kongdhau, S. Bordiga, *Chem. Mater.* 18 (2006) 1337.
- [100] J. L. C. Rowsell, O. M. Yaghi, *J. Am. Chem. Soc.* 128 (2006) 1304.
- [101] A. Centrone, D. Y. Siberio-Pérez, A. Millward, O. M. Yaghi, A. J. Matzger, G. Zerbi, *Chem. Phys. Lett.* 411 (2005) 516.
- [102] H. W. Langmi, D. Book, A. Walton, S. R. Johnson, M. M. Al-Mamouri, J. D. Speight, P. P. Edwards, I. R. Harris, P. A. Anderson, *J. Alloys and Compounds* 404-406 (2005) 637.
- [103] S. S. Kaye, J. R. Long, *J. Am. Chem. Soc.* 127 (2005) 6506.
- [104] G. Gao, T. Cagin, W. A. Goddard III, *Nanotechnology* 9 (1998) 184.

ACKNOWLEDGMENTS

I would like to thank the people who contributed in different ways to the realization of this work.

My thank goes to my supervisor, **Michael Hirscher**, for advising me and supporting me constantly during these three years.

I'm thankful to **Prof. Gisela Schütz** who gave me the possibility to work in her department, and who always supported the hydrogen storage project.

I would like to thank Prof. **Emil Roduner** for fruitful discussions and for making me feel as a part of his group.

I am grateful to **Bernd Ludescher, Werner Dietrich and Uwe Engelhard** for their constant technical support.

Thanks to Prof. **Karl Syassen** for giving me the possibility to work in his Raman laboratory and to **Ingo Loa** for introducing me to the world of Raman spectroscopy.

My thanks go also to **Annette Fuchs, Ewald Bischoff, Robert Dinnebier and Pascal Dietzel** for their contributions to this work.

Special thanks go to **Ulrich Müller** from BASF for kindly providing most of the MOF samples.

I am also grateful to **Richard Chahine, John Vajo, Channing Ahn, Mauricio Terrones, Humberto Terrones, Eduardo Terres, Jose Manuel Dominguez, Ursula Dettlaff-Wegliskowska** for providing the carbon samples.

Thank you to **Siegmar Roth** and to his group for scientific discussions on hydrogen storage.

I am grateful to the **Max-Planck-Research School** for financial support and to **Hans-Georg Libuda** for his help during these three years.

Finally my most sincere thanks go to the people who always supported me during these three years:

My thanks go to **Uta, Gerhard, Oma, Martina, Thomas, Lisa und Lena**. Danke für Freude, Trost, und Unterstützung in diesen drei Jahren.

Many thanks go to my friends of Stuttgart, especially the Italian community and to the friends of Rome for distraction out of work.

Grazie **Gambassi** per la tua stupenda amicizia!

Grazie **Roberto**, per questi anni meravigliosi passati insieme.

Grazie **Sandra** perché so che per me ci sei sempre.

Mein größter Dank geht an meine **Eltern, Monika und Mario**. Ihr habt mir immer Liebe und Vertrauen geschenkt, mich in Allem unterstützt, und auch in schwierigen Zeiten habt Ihr mir Sicherheit und Halt gegeben.

This thesis is dedicated to my Dad.

Papà sei il mio esempio per la vita.

Curriculum Vitae

Barbara Panella

Date of birth and birthplace: 3rd December 1978, Rome, Italy

Education:

- 1985-1998: Deutsche Schule Rom, Italy.
- 1998-2003: Studies in Chemistry, Università degli Studi di Roma "La Sapienza", Italy. Title of Laurea Thesis: "Pd/H₂ in hydrogen cold plasma: thermodynamic, kinetic and structural aspects".
- 2003-2006: Dissertation at the Max-Planck-Institut für Metallforschung, Stuttgart.
- 2003-2006: Member of the Max-Planck-Research School for Advanced Material

Publications related to the present work:

- B. Panella, M. Hirscher, S. Roth, *Hydrogen adsorption in different carbon nanostructures*, Carbon 43 (2005) 2209
- E. Terrés, B. Panella, T. Hayashi, Y. A. Kim, M. Endo, J. M. Dominguez, M. Hirscher, H. Terrones, M. Terrones, *Hydrogen storage in spherical nanoporous carbons*, Chem. Phys. Lett. 403 (2005) 363
- M. Hirscher, B. Panella, *Nanostructures with high surface area for hydrogen storage*, J. Alloys Comp. 404-406 (2005) 399
- B. Panella, M. Hirscher, *Hydrogen physisorption in metal-organic porous crystals*, Adv. Mat. 17 (2005) 538
- P. D. C. Dietzel, B. Panella, M. Hirscher, R. Blom, H. Fjellvåg, *Hydrogen adsorption in a nickel based coordination polymer with open metal sites in the cylindrical cavities of the desolvated framework*, Chemm. Commun (2006) 959
- B. Panella, M. Hirscher, H. Pütter, U. Müller, *Hydrogen adsorption in metal-organic frameworks: Cu-MOFs and Zn-MOFs compared*, Adv. Funct. Mat. 16 (2006) 520